Aalto University
School of Engineering

AALTO UNIVERSITY
School of Engineering
Department of Engineering Design and Production

Klaus Kivekäs

Estimation of Tire-Road Friction Potential Based on Inertial Sensor Measurements in Low-Friction Conditions

Thesis submitted in partial fulfilment of the requirements for the degree of Master of Science in Technology

Espoo 30.05.2016
Supervisor: Professor Kari Tammi
Thesis Instructor: D.Sc (Tech) Ari Tuononen

Author Klaus Kivekäs

Title of thesis Estimation of Tire-Road Friction Potential Based on Inertial Sensor Measurements in Low-Friction Conditions

Degree programme Engineering Design and Production

Major/minor Machine Design/Mechatronics **Code** K3001

Thesis supervisor Professor Kari Tammi

Thesis advisor(s) D.Sc (Tech) Ari Tuononen

Date 30.05.2016 **Number of pages** 101+1 **Language** English

Abstract

Electronic driver aids have become commonplace in passenger cars in the last two decades. These systems improve safety by attempting to prevent the vehicle from exceeding the limits of its handling and becoming unstable. Those limits are largely defined by the tire-road friction potential. Consequently, the friction potential is one of the variables used in the control logics of these systems. Thus, by estimating the potential, the effectiveness of electronic driver aids can be significantly improved.

The purpose of this thesis is to develop and test the accuracy of a novel friction estimation algorithm that uses the accelerations and yaw, pitch, and roll rates of the vehicle measured with an inertial sensor as its basis. The algorithm was designed to account for the effects of inclination and banking, as they influence the acceleration capabilities of the vehicle and the acceleration measurements. Three different versions of the algorithm were created so that the effects of compensating for inclination and bank angle could be assessed. Additionally, the algorithm was designed in such a way that it should be able to estimate the friction potential accurately in start maneuvers where the steering angle is high. The single-track model was incorporated into the algorithm for this purpose. The algorithm must also detect when the vehicle is on the limits of its handling, as it is only then that the measured friction coefficient is equal to the friction potential. The algorithm accomplishes this by monitoring the states of the driver aids.

The algorithm was tested with simulations and experimental tests. The research vehicle was modelled in simulation software, including the most significant electronic driver aids. A variety of acceleration, braking, and cornering maneuvers were performed in order to test the capabilities of the algorithm on roads with varying inclinations and bank angles. The tests focused on low-friction conditions, as friction estimation is at its most beneficial in such circumstances.

The results show that this novel algorithm is capable of estimating the friction potential accurately in most acceleration, braking, and cornering situations on inclined, banked, and level roads. However, the results also indicate that accounting for the inclination and the bank angle makes little difference in the friction estimation. The algorithm calculates the tire-road forces largely based on the longitudinal and lateral acceleration measurements of the inertial sensor, which contain a component of gravitational acceleration if the road is not level. Thus, the effects of inclination and bank angle get mostly compensated even in the versions that were not specifically designed to account for them. The results also show that the friction potential estimation produced by the single-track model in high steering angle start maneuvers contains significant error due to the two front tires producing forces in different directions in such situations.

Keywords friction potential, passenger car, TCS, ABS, ESP, low friction

Tekijä Klaus Kivekäs

Työn nimi Tien ja renkaan välisen kitkapotentiaalin arviointi inertia-anturin mittausten perusteella alhaisen kitkan olosuhteissa

Koulutusohjelma Konetekniikka

Pää-/sivuaine Koneensuunnittelu/Mekatroniikka **Koodi** K3001

Työn valvoja Prof. Kari Tammi

Työn ohjaaja(t) TkT Ari Tuononen

Päivämäärä 30.05.2016 **Sivumäärä** 101+1 **Kieli** Englanti

Tiivistelmä

Elektronisista ajoavuista on tullut yleisiä henkilöautoissa viimeisten kahden vuosikymmenen aikana. Nämä järjestelmät parantavat turvallisuutta yrittämällä estää autoa ylittämästä suorituskykyrajojaan, jolloin auto muuttuu epästabiiliksi. Kyseiset rajat perustuvat laajalti renkaan ja tien väliseen kitkapotentiaaliin. Kitkapotentiaali on siksi yksi niistä muuttujista, joita nämä järjestelmät käyttävät ohjauslogiikoissaan. Täten ajoapujen toimintaa voidaan tehostaa merkittävästi estimoimalla kitkapotentiaalia.

Tämän opinnäytetyön tarkoituksena on luoda uudenlainen kitkaestimointialgoritmi, jonka toiminta perustuu inertia-anturilla mitattaviin auton kiihtyvyyksiin ja kallistumis-, nyökkimis- ja pystykiertymänopeuksiin, ja tutkia sen tarkkuutta. Algoritmi suunniteltiin huomioimaan tien nousu- ja sivuttaiskulmien vaikutus, sillä ne vaikuttavat auton kiihtyvyysrajoihin ja mitattuihin kiihtyvyyslukemiin. Algoritmista luotiin kolme eri versiota, jotta tien kulmien kompensoinnin vaikutusta voitaisiin arvioida. Lisäksi algoritmi suunniteltiin siten, että sen pitäisi kyetä arvioimaan kitkapotentiaalia tarkasti myös sellaisissa liikkeellelähtötilanteissa, joissa ohjauskulma on suuri. Kaksipyörämalli sisällytettiin algoritmiin tätä tarkoitusta varten. Algoritmin on myös kyettävä havaitsemaan, milloin auto on lähellä suorituskykyrajojaan, koska arvioitu kitkakerroin on lähellä kitkapotentiaalia vain silloin. Algoritmi toteuttaa tämän tarkkailemalla ajoapujen tiloja.

Algoritmia testattiin simulaatioiden ja koeautolla tehtävien testien avulla. Koeauto ja sen merkittävimmät ajoavut mallinnettiin simulaatio-ohjelmistossa. Monenlaisia kiihdytys-, jarrutus- ja kaarreajoliikkeitä suoritettiin algoritmin kykyjen tutkimiseksi erilaisia kallistuksia sisältävillä teillä. Testit keskittyivät alhaisen kitkan olosuhteisiin, sillä kitkaestimoinnista on eniten hyötyä juuri sellaisissa oloissa.

Tulokset näyttävät, että luotu algoritmi kykenee arvioimaan kitkapotentiaalia tarkasti useimmissa kiihdytys-, jarrutus- ja kaarreajotilanteissa mäkisillä, kallistetuilla ja tasaisilla teillä. Tulokset kuitenkin myös osoittavat, että nousu- ja sivuttaiskulman huomiointi algoritmissa tuottaa vain pienen eron kitkaestimoinnissa. Algoritmi laskee rengasvoimat perustuen enimmäkseen inertia-anturin pitkittäis- ja sivuttaiskiihtyvyysmittauksiin, jotka sisältävät putoamiskiihtyvyys-komponentin, mikäli tie ei ole tasainen. Täten nousu- ja sivuttaiskulmien vaikutus kompensoituu enimmäkseen pois niissäkin algoritmiversioissa, joita ei erityisesti suunniteltu huomioimaan kyseisiä kulmia. Tulokset näyttävät myös, että kaksipyörämallin tuottama kitkapotentiaaliarvio suuren ohjauskulman liikkeellelähtötilanteissa sisältää merkittävästi virhettä johtuen siitä, että etupyörät tuottavat tällöin voimaa eri suuntiin.

Avainsanat kitkapotentiaali, henkilöauto, TCS, ABS, ESP, alhainen kitka

Acknowledgements

This master's thesis was done in the Laboratory of Automotive Engineering at Aalto University School of Engineering. First of all, I want to thank the Henry Ford Foundation for providing me with a scholarship to carry out this fascinating study.

Special thanks to my thesis advisor D.Sc. Ari Tuononen for giving me the opportunity and framework for this thesis, as well as valuable guidance throughout the research, and assistance in performing the road tests with the research vehicle. I would also like to extend my gratitude to doctoral students Arto Niskanen and Yi Xiong for assisting with assembling and calibrating the measurement equipment for the research vehicle. My thanks also go to Professor Kari Tammi for giving important feedback and comments in finishing the thesis.

Finally, thanks to the fellow master's thesis workers at the office for keeping the atmosphere pleasant and to my family for supporting me throughout my studies.

Espoo 30.05.2016

Klaus Kivekäs

Table of Contents

Symbols and Definitions

A	[m^2]	Frontal reference area
A_p	[m]	Peak-to-peak amplitude
A_s	[-]	State transition matrix
B_x	[-]	MF longitudinal force stiffness factor
$B_{x\alpha}$	[-]	MF longitudinal force combined slip stiffness factor
B_y	[-]	MF lateral force stiffness factor
$B_{y\kappa}$	[-]	MF lateral force combined slip stiffness factor
C_i	[N/rad]	Tire lateral stiffness
C_1	[N/rad]	Front axle lateral stiffness
C_2	[N/rad]	Rear axle lateral stiffness
C_x	[-]	MF longitudinal force shape factor
$C_{x\alpha}$	[-]	MF longitudinal force combined slip shape factor
C_y	[-]	MF lateral force shape factor
$C_{y\kappa}$	[-]	MF lateral force combined slip shape factor
$D_{Vy\kappa}$	[N]	MF longitudinal-slip-induced lateral force vertical shift factor
D_x	[N]	MF longitudinal force peak value
D_y	[N]	MF lateral force peak value
E_x	[-]	MF longitudinal force curvature factor
$E_{x\alpha}$	[-]	MF longitudinal force combined slip curvature factor
E_y	[-]	MF lateral force curvature factor
$E_{y\kappa}$	[-]	MF lateral force combined slip curvature factor
F_D	[N]	Aerodynamic drag force
F_x	[N]	Longitudinal force
F_{x0}	[N]	MF longitudinal force in pure longitudinal slip situations
F_{x1}	[N]	Total longitudinal force produced by front tires
F_{x2}	[N]	Total longitudinal force produced by rear tires
$F_{x,tot}$	[N]	Total longitudinal force produced by all tires
F_y	[N]	Lateral force
F_{y0}	[N]	MF lateral force in pure lateral slip situations
F_{y1}	[N]	Total lateral force produced by front tires
F_{y2}	[N]	Total lateral force produced by rear tires
$F_{y,tot}$	[N]	Total lateral force produced by all tires
F_z	[N]	Wheel load
F_{z0}	[N]	Nominal wheel load
F_{z1}	[N]	Front axle vertical load
F_{z2}	[N]	Rear axle vertical load
F_{z3}	[N]	Vertical load of left side wheels
F_{z4}	[N]	Vertical load of right side wheels
$F_{z,1,1}$	[N]	Front axle vertical load estimated by algorithm version 1
$F_{z,1,2}$	[N]	Front axle vertical load estimated by algorithm version 2
$F_{z,1,3}$	[N]	Front axle vertical load estimated by algorithm version 3
$F_{z,tot}$	[N]	Total vertical load
$F_{z,tot,1}$	[N]	Total vertical load estimated by algorithm version 1
$F_{z,tot,2}$	[N]	Total vertical load estimated by algorithm version 2

$F_{z,tot,3}$	[N]	Total vertical load estimated by algorithm version 3
G	[N]	Force of gravity
$G_{x\alpha}$	[-]	MF longitudinal force combined slip reduction factor
$G_{x\alpha 0}$	[-]	MF longitudinal force combined slip horizontal shift factor
$G_{y\kappa}$	[-]	MF lateral force combined slip reduction factor
$G_{y\kappa 0}$	[-]	MF lateral force combined slip horizontal shift factor
H	[-]	KF measurement matrix
I_{zz}	[kgm^2]	Moment of inertia around the vertical axis at the CoG
K_k	[-]	KF Kalman gain matrix
$K_{x\kappa}$	[-]	MF longitudinal slip stiffness
$K_{y\alpha}$	[-]	MF lateral force stiffness coefficient
N	[-]	Number of data points used by moving average filter
P_k^-	[-]	KF *a priori* estimate of error covariance at instant k
$\hat{P}_k$	[-]	KF *a posteriori* estimate of error covariance at instant k
Q	[-]	KF process noise covariance matrix
Q_u	[-]	KF velocity estimation process noise covariance matrix
Q_θ	[-]	KF inclination estimation process noise covariance matrix
Q_φ	[-]	KF bank angle estimation process noise covariance matrix
R	[-]	KF measurement noise covariance matrix
$R_{u,1}$	[-]	KF velocity estimation primary meas. noise covariance matrix
$R_{u,1}$	[-]	KF velocity estimation secondary meas. noise covariance matrix
$R_{\theta,1}$	[-]	KF inclination estimation primary meas. noise covariance matrix
$R_{\theta,2}$	[-]	KF incl. estimation secondary meas. noise covariance matrix
R_φ	[-]	KF bank angle estimation measurement noise covariance matrix
R_0	[m]	Unloaded wheel radius
S_{Hx}	[-]	MF longitudinal force horizontal shift
$S_{Hx\alpha}$	[-]	MF horizontal shift factor for combined slip F_x reduction
S_{Hy}	[rad]	MF lateral force horizontal shift
$S_{Hy\kappa}$	[rad]	MF horizontal shift factor for combined slip F_y reduction
S_{Vx}	[N]	MF longitudinal force vertical shift
S_{Vy}	[N]	MF lateral force vertical shift
$S_{Vy\kappa}$	[N]	MF longitudinal-slip-induced lateral force vertical shift
T_s	[s]	Sample time
a	[m]	Optical sensor lateral distance from the CoG
a_x	[m/s^2]	Longitudinal acceleration of the CoG of the vehicle
$a_{x,k}$	[m/s^2]	Longitudinal acceleration of the CoG of the vehicle at instant k
$a_{x,e}$	[m/s^2]	Estimated longitudinal acceleration
$a_{x,m}$	[m/s^2]	Longitudinal acceleration measured by IMU
$a_{x,m,c}$	[m/s^2]	Longit. acceleration measured by IMU corrected to the CoG
a_y	[m/s^2]	Lateral acceleration of the CoG of the vehicle
$a_{y,e}$	[m/s^2]	Estimated lateral acceleration
$a_{y,m}$	[m/s^2]	Lateral acceleration measured by IMU
b	[m]	Optical sensor longitudinal distance from the CoG
b_{is}	[m]	IMU longitudinal distance from the CoG
b_1	[m]	Front track width
b_2	[m]	Rear track width

c_D	[-]	Drag coefficient
d	[-]	Delay caused by moving average filter
df_z	[-]	MF relative change of vertical load
g	[m/s^2]	Standard acceleration due to gravity
g_e	[m/s^2]	Longit. acc. measurement error caused by IMU error offset angle
l	[m]	Wheelbase
l_1	[m]	Front axle longitudinal distance from the CoG
l_2	[m]	Rear axle longitudinal distance from the CoG
p_{Cx1}	[-]	MF shape factor for longitudinal forces
p_{Cy1}	[-]	MF shape factor for lateral forces
p_{Dx1}	[-]	MF longitudinal friction coefficient μ_x
p_{Dx2}	[-]	MF variation of friction coefficient μ_x with load
p_{Dx3}	[-]	MF variation of friction coefficient μ_x with squared camber
p_{Dy1}	[-]	MF lateral friction coefficient μ_y
p_{Dy2}	[-]	MF variation of friction coefficient μ_y with load
p_{Dy3}	[-]	MF variation of friction coefficient μ_y with squared camber
p_{Ex1}	[-]	MF longitudinal force curvature factor E_x at F_{z0}
p_{Ex2}	[-]	MF variation of E_x with load
p_{Ex3}	[-]	MF variation of E_x with load squared
p_{Ex4}	[-]	MF variation of E_x with κ_x sign
p_{Ey1}	[-]	MF lateral force curvature factor E_y at F_{z0}
p_{Ey2}	[-]	MF variation of E_y with load
p_{Ey3}	[-]	MF zero order camber dependency of E_y
p_{Ey4}	[-]	MF variation of E_y with camber
p_{Hx1}	[-]	MF horizontal shift S_{Hx} at F_{z0}
p_{Hx2}	[-]	MF variation of shift S_{Hx} with load
p_{Hy1}	[-]	MF horizontal shift S_{Hy} at F_{z0}
p_{Hy2}	[-]	MF variation of shift S_{Hy} with load
p_{Hy3}	[-]	MF variation of shift S_{Hy} with camber
p_{Kx1}	[-]	MF longitudinal slip stiffness $K_{x\kappa}$ at F_{z0}
p_{Kx2}	[-]	MF variation of $K_{x\kappa}$ with load
p_{Kx3}	[-]	MF variation of slip stiffness $K_{x\kappa}$ exponent with load
p_{Ky1}	[-]	MF maximum value of stiffness coefficient $K_{y\alpha}$ at F_{z0}
p_{Ky2}	[-]	MF load at which $K_{y\alpha}$ reaches maximum value
p_{Ky3}	[-]	MF variation of $K_{y\alpha}/F_{z0}$ with camber
p_{Tx1}	[-]	MF relaxation length σ_κ at F_{z0}
p_{Tx2}	[-]	MF variation of σ_κ with load
p_{Tx3}	[-]	MF variation of σ_κ with exponent of load
p_{Ty1}	[-]	MF peak value of relaxation length σ_α
p_{Ty2}	[-]	MF shape factor of relaxation length σ_α
p_{Vx1}	[-]	MF vertical shift S_{Vx}/F_z at F_{z0}
p_{Vx2}	[-]	MF variation of shift S_{Vx}/F_z with load
p_{Vy1}	[-]	MF vertical shift S_{Vy}/F_z at F_{z0}
p_{Vy2}	[-]	MF variation of shift S_{Vy}/F_z with load
p_{Vy3}	[-]	MF variation of shift S_{Vy}/F_z with camber
p_{Vy4}	[-]	MF variation of shift S_{Vy}/F_z with camber and load

r_{Bx1}	[-]	MF slope factor $B_{x\alpha}$ for combined slip F_x reduction
r_{Bx2}	[-]	MF variation of $B_{x\alpha}$ with slip ratio
r_{By1}	[-]	MF slope factor $B_{y\kappa}$ for combined slip F_y reduction
r_{By2}	[-]	MF variation of $B_{y\kappa}$ with slip angle
r_{By3}	[-]	MF shift term for slip angle in slope factor $B_{y\kappa}$
r_{Cx1}	[-]	MF shape factor $B_{x\alpha}$ for combined slip F_y reduction
r_{Cy1}	[-]	MF shape factor $C_{y\kappa}$ for combined slip F_y reduction
r_{Ex1}	[-]	MF curvature factor $E_{x\alpha}$ at F_{z0}
r_{Ex2}	[-]	MF variation of $E_{x\alpha}$ with load
r_{Ey1}	[-]	MF curvature factor $E_{y\kappa}$ at F_{z0}
r_{Ey2}	[-]	MF variation of $E_{y\kappa}$ with load
r_{Hx1}	[-]	MF shift factor $S_{Hx\alpha}$ at F_{z0}
r_{Hy1}	[-]	MF shift factor $S_{Hy\kappa}$ at F_{z0}
r_{Hy2}	[-]	MF variation of $S_{Hy\kappa}$ with load
r_{Vy1}	[-]	MF κ-induced lateral force at F_{z0}
r_{Vy2}	[-]	MF variation of κ-induced lateral force with load
r_{Vy3}	[-]	MF variation of κ-induced lateral force with camber
r_{Vy4}	[-]	MF variation of κ-induced lateral force with slip angle
r_{Vy5}	[-]	MF variation of κ-induced lateral force with κ
r_{Vy6}	[-]	MF variation of κ-induced lateral force with $\tan^{-1}(\kappa)$
r_d	[m]	Tire dynamic rolling radius
$r_{d,e}$	[m]	Estimated dynamic rolling radius
r_z	[rad/m]	Ratio between wheel angle and steering rack displacement
t	[s]	Time
u	[m/s]	Longitudinal velocity of the CoG of the vehicle
u_{char}	[m/s]	Characteristic speed
u_{def}	[m]	Longitudinal tire deformation
u_e	[m/s]	Estimated longitudinal velocity of the CoG of the vehicle
u_k	[m/s]	Longitudinal velocity of the CoG of the vehicle at instant k
v	[m/s]	Lateral velocity of the CoG of the vehicle
$\dot{v}$	[m/s^2]	Time derivative of lateral velocity
v_{def}	[m]	Lateral tire deformation
v_k	[-]	Variance of measurement noise at instant k
v_{sensor}	[m/s]	Optical sensor total velocity
$v_{x,sensor}$	[m/s]	Optical sensor longitudinal velocity
$v_{y,is}$	[m/s]	Lateral velocity at the location of the IMU
$\dot{v}_{y,is}$	[m/s]	Time derivative of lateral velocity at the location of the IMU
$v_{y,sensor}$	[m/s]	Optical sensor lateral velocity
v_{tot}	[m/s]	Tire total velocity
$v_{tot,CoG}$	[m/s]	Total velocity of the CoG of the vehicle
$v_{tot,f}$	[m/s]	Front axle total velocity
$v_{tot,r}$	[m/s]	Rear axle total velocity
v_x	[m/s]	Tire longitudinal velocity
$v_{x,FL,c}$	[m/s]	CoG longitudinal velocity calculated based on FL wheel speed
$v_{x,FR,c}$	[m/s]	CoG longitudinal velocity calculated based on FR wheel speed
$v_{x,RL,c}$	[m/s]	CoG longitudinal velocity calculated based on RL wheel speed

$v_{x,RR,c}$	[m/s]	CoG longitudinal velocity calculated based on RR wheel speed
v_y	[m/s]	Tire lateral velocity
w_k	[-]	Variance of process noise at instant k
$w_{u,1,k}$	[-]	Variance of acceleration measurement noise at instant k
$w_{u,2,k}$	[-]	Variance of wheel-speed-based velocity meas. noise at instant k
$w_{\theta,1,k}$	[-]	Variance of pitch rate measurement noise at instant k
$w_{\theta,2,k}$	[-]	Variance of inclination estimation noise at instant k
$w_{\varphi,1,k}$	[-]	Variance of roll rate measurement noise at instant k
$w_{\varphi,2,k}$	[-]	Variance of bank angle estimation noise at instant k
x	[-]	Moving average filter input signal
x_k	[-]	State of the system at instant k
x_k^-	[-]	KF *a priori* estimate of the state of the system at instant k
$\hat{x}_k$	[-]	KF *a posteriori* estimate of the state of the system at instant k
y	[-]	Moving average filter output signal k
z_k	[-]	KF measurement at instant k
Ω	[rad/s]	Tire rotational speed
Ω_{FL}	[rad/s]	Left front wheel rotational speed
Ω_{FR}	[rad/s]	Right front wheel rotational speed
Ω_{RL}	[rad/s]	Left rear wheel rotational speed
Ω_{RR}	[rad/s]	Right rear wheel rotational speed
α	[rad]	Tire slip angle
α'	[rad]	Relaxation-length-compensated tire slip angle
α_s	[rad]	MF slip angle definition in combined slip situations
α_y	[rad]	MF slip angle definition in pure lateral slip situations
β	[rad]	Vehicle side slip angle
γ	[rad]	Camber angle
γ_y	[rad]	MF camber angle with $\lambda_{\gamma y}$ scale factor
γ_z	[rad]	MF camber angle with $\lambda_{\gamma z}$ scale factor
δ	[rad]	Steering angle
δ_w	[rad]	Steering wheel angle
ε	[rad]	Yaw rate dead zone
ε_{is}	[rad]	IMU error offset angle
θ	[rad]	Pitch angle / Inclination angle
θ_e	[rad]	Estimated inclination angle
$\theta_{e2,k}$	[rad]	Wheel-speed-and-IMU-based inclination estimation at instant k
θ_k	[rad]	Inclination angle at instant k
$\dot{\theta}_k$	[rad/s]	Pitch rate at instant k
κ	[-]	Slip ratio
κ'	[-]	Relaxation-length-compensated slip ratio
κ_s	[-]	MF slip ratio definition in combined slip situations
κ_x	[-]	MF slip ratio definition in pure longitudinal slip situations
λ	[m]	Wavelength
λ_{Cx}	[-]	MF Scale factor of F_x shape factor C_x
λ_{Cy}	[-]	MF Scale factor of F_y shape factor C_y
λ_{Ex}	[-]	MF Scale factor of F_x curvature factor E_x
λ_{Ey}	[-]	MF Scale factor of F_y curvature factor E_y
λ_{Hx}	[-]	MF Scale factor of F_x horizontal shift S_{Hx}

λ_{Hy}	[-]	MF Scale factor of F_y horizontal shift S_{Hy}
$\lambda_{K x \kappa}$	[-]	MF Scale factor of F_x slip stiffness coefficient $K_{x\kappa}$
$\lambda_{K y \alpha}$	[-]	MF Scale factor of F_y stiffness coefficient $K_{y\alpha}$
λ_{Vx}	[-]	MF Scale factor of F_x vertical shift S_{Vx}
λ_{Vy}	[-]	MF Scale factor of F_y vertical shift S_{Vy}
$\lambda_{V y \kappa}$	[-]	MF Scale factor of κ-induced F_y
$\lambda_{x\alpha}$	[-]	MF Scale factor of α influence on F_x
$\lambda_{y\kappa}$	[-]	MF Scale factor of κ influence on F_y
$\lambda_{\gamma x}$	[-]	MF Scale factor of camber for F_x
$\lambda_{\gamma y}$	[-]	MF Scale factor of camber for F_y
$\lambda_{\gamma z}$	[-]	MF Scale factor of camber for combined slip F_y
$\lambda_{\mu x}$	[-]	MF Scale factor of peak longitudinal friction coefficient μ_x
$\lambda_{\mu y}$	[-]	MF Scale factor of peak lateral friction coefficient μ_y
μ	[-]	Friction coefficient
μ_e	[-]	Estimated friction coefficient
μ_{eff}	[-]	CarMaker effective friction coefficient
μ_t	[-]	Overall tire-road friction coefficient
μ_{pot}	[-]	Friction potential
μ_{road}	[-]	CarMaker user-defined friction coefficient
μ_x	[-]	Longitudinal tire-road friction coefficient
μ_y	[-]	Lateral tire-road friction coefficient
ρ	[kg/m^3]	Density of air
σ_α	[m]	Slip-angle-related relaxation length
σ_κ	[m]	Slip-ratio-related relaxation length
τ	[-]	Steering ratio
τ_{swtr}	[rad/m]	Ratio of steering wheel angle and steering rack displacement
φ	[rad]	Roll angle / Bank angle
$\dot{\varphi}$	[rad/s]	Roll rate
φ_e	[rad]	Estimated bank angle
$\varphi_{e,k}$	[rad]	Estimated bank angle at instant k
φ_k	[rad]	Bank angle at instant k
$\dot{\varphi}_k$	[rad/s]	Roll rate at instant k
$\dot{\varphi}_{m,k}$	[rad/s]	Roll rate measured by IMU at instant k
ψ	[rad]	Yaw angle
$\dot{\psi}$	[rad/s]	Yaw rate
$\ddot{\psi}$	[rad/s^2]	Time derivative of yaw rate
$\dot{\psi}_{No}$	[rad/s]	Nominal yaw rate

Abbreviations

ABS	Anti-lock Braking System
ACC	Adaptive Cruise Control
ARB	Anti-roll Bar
CIT	CarMaker Interface Toolbox
CoG	Center of Gravity
ESP	Electronic Stability Program
FL	Left Front Wheel
FR	Right Front Wheel
GUI	Graphical User Interface
HIL	Hardware-in-the-Loop
KF	Kalman Filter
LED	Light-Emitting Diode
MF	Magic Formula
PIARC	Permanent International Association of Road Congresses
PSD	Position Sensitive Detector
RL	Left Rear Wheel
RPM	Revolutions per Minute
RR	Right Rear Wheel
SAW	Surface Acoustic Wave
TCS	Traction Control System
VVE	Virtual Vehicle Environment

1 Introduction

1.1 Motivation and Background

Most car accidents are caused by human error [1]. The widespread introduction of electronic driver aids, such as traction control systems (TCS), anti-lock braking systems (ABS), adaptive cruise control (ACC), and electronic stability programs (ESP), has significantly reduced road fatalities. For instance, the number of road fatalities reduced by 60 % in Germany between 1999 and 2013 while installation rates for ABS and ESP systems increased substantially. [2]

The primary purpose of active safety systems is to allow the driver to maintain control of the vehicle. ABS assists the driver under heavy braking by preventing the wheels from locking up. This allows for a decent level of handling performance even under full braking. The system detects if one or more wheels are on the verge of locking up and limits brake pressure accordingly. [3; 4] The purpose of the TCS is to prevent the driven wheels from spinning under acceleration by limiting the drive torque at each driven wheel. This ensures that the vehicle remains stable and steerable while also improving traction. [3] The main task of the ESP is to prevent the vehicle from spinning. It enhances the directional stability of the vehicle in various situations by using the braking and engine management systems as tools for steering the vehicle. [3; 4] ACC differs from the previously discussed three systems in that it partially removes control from the driver rather than enhancing it. Its purpose is to control the velocity of the vehicle and maintain a safe distance to the car in front. While it is not considered an active safety system, ACC still has a significant impact on safety due to maintaining larger distances between vehicles. [3]

Real-time information about the current friction coefficient between the tires and the road is beneficial to all of the aforementioned electronic driver aids, particularly in slippery conditions. The coefficient can vary greatly between different conditions, ranging from as low as 0.05 on ice-covered roads up to 1.3 on dry tarmac [5]. Tire-road forces, which are limited by the friction coefficient, largely dictate the maximum lateral and longitudinal accelerations of the vehicle. ABS can function more effectively if the maximum possible longitudinal deceleration is known. TCS uses the current tire-road friction coefficient as one of the factors in determining a reference value for the amount of slip that it tries to maintain the driven wheels at. [3] The performance of an ESP system is reliant on information about the friction coefficient due to its influence on the lateral acceleration and yaw rate limits of the vehicle [4]. ACC can also function more safely if the current friction coefficient is known, as the system can then adapt the gap to the car in front accordingly. The lower the coefficient is, the longer the braking distances are, and thus the longer the gap should be. [3]

Real-time tire-road friction coefficient estimation will become increasingly relevant in the coming decades due to autonomous passenger cars becoming more commonplace. Autonomous vehicles lack the intelligence to reliably overcome hazardous situations. Thus, having accurate information about the friction coefficient, in order to avoid exceeding the handling limits and putting the vehicle in a dangerous position, is even more important than it is in human-operated vehicles. [6]

1.2 Problem Statement

Numerous different tire-road friction coefficient estimation methods have been developed. They can be categorized into direct and vehicle dynamics based versions. The direct methods attempt to measure the friction coefficient with special sensors, e.g. acoustic, optical, or strain sensors. These sensors are typically either exceedingly expensive or lacking in robustness and reliability, which makes direct estimation impractical for commercial use. [7; 8; 9; 10] Instead, vehicle dynamics based methods are preferable. They are based on measuring the motions of the vehicle and estimating the friction coefficient using vehicle dynamics models. [10]

The objective of this master's thesis is to develop a friction estimation algorithm that could be feasibly implemented into production cars in the near future and to examine the accuracy of the algorithm. The approach chosen for the development of the algorithm is to deploy an inertial measurement unit (IMU) that includes a triaxial acceleration sensor and a triaxial gyroscope to work in conjunction with the sensors commonly found in commercial automobiles, such as wheel speed sensors, brake pressure sensors, and a gas pedal position sensor, in order to measure the motions of the vehicle. By measuring the longitudinal and lateral accelerations and yaw, pitch, and roll rates of the car, a decent approximation for the tire-road friction coefficient can be calculated when the car is on the limits of its handling.

One issue with this approach is that the acceleration sensor measures components of gravitational acceleration on axes other than the vertical z-axis if the sensor is not perfectly level. This causes error in longitudinal and lateral acceleration measurements if the road has inclination or bank angle unless they are compensated for. On the other hand, road inclination and bank angle also affect the car's acceleration and the vertical loads on the tires. For these reasons, the algorithm is also designed to be able to measure road inclination and bank angle and to account for them in estimating the friction coefficient.

The ability of the algorithm to estimate the tire-road friction coefficient is tested in both simulations and road tests. The simulations are conducted with CarMaker for Simulink, which is a complete integration of the CarMaker vehicle dynamics simulation software into the MATLAB and Simulink modeling and simulation environment [11]. This way, the friction estimation algorithm, created in Simulink, can be used for analyzing both the simulation model and the data from the real test vehicle. The tests focus on slippery winter conditions, as friction estimation is at its most advantageous in such circumstances. The effect of road inclination and bank angle estimation on the accuracy of the friction estimation algorithm is also tested. Traction control and anti-lock braking system algorithms are already supplied with the simulation software, requiring only minor modifications to work appropriately, but an ESP system needs to be developed. In the road tests, the research vehicle is equipped with a wheel-integrated force transducer system in order to obtain the actual friction coefficient for comparison with the algorithm.

Another concern is that the mass and the center of gravity (CoG) of the car can vary depending on the amount of passengers and luggage in the car. This causes some inaccuracy in the friction estimation. The effects of inaccurate information about the location of the center of gravity and the mass of the vehicle on the estimation are tested in this thesis.

1.3 Outline

The tire-road interface is examined in Chapter 2. The characteristics of rubber are discussed first, and then the basic tire-road friction mechanisms are explained. The effect of road conditions and tire tread patterns on friction are also discussed in this chapter. In Chapter 3, the basics and terminology of vehicle and tire dynamics are discussed. Chapter 4 presents an overview of the various different friction estimation methods that have been developed and also addresses the most common electronic driver aids and how they can take advantage of friction estimation.

Chapter 5 presents an overview of the research vehicle and sensor equipment used in the road test measurements. In Chapter 6, the simulation model built with CarMaker for Simulink is discussed. After giving an overview of the simulation software, the simulated vehicle is explained in detail. Chapter 7 is dedicated to the created friction estimation algorithm. The Kalman filter, which is central to the algorithm, is also discussed in the same chapter. The test maneuvers conducted with the research vehicle and in the simulation software are explained in Chapter 8. In Chapter 9, both the simulation and road test results are presented and discussed. Differences and similarities in the results between the simulations and the road test measurements are examined, and potential sources of error are discussed, including shortcomings of the friction estimation algorithm. Comparisons to previous studies are also made. Finally, Chapter 10 concludes the thesis with suggestions for improvements and potential future work.

2 Tire-Road Interface

Tire tread rubber is the only portion of the car that is in direct contact with the road. The properties of both the tires and the road surface significantly affect the tire-road friction forces. The viscoelastic nature of tire rubber allows the rubber to grip firmly onto the road with the aid of hysteresis and adhesion. Road surface texture and conditions have a substantial impact on the effectiveness of these mechanisms. Tire construction and tread pattern design also influence the characteristics of the tire.

2.1 Rubber Characteristics

2.1.1 Viscoelasticity

Rubber is a viscoelastic material, which means that its behavior lies somewhere between that of a viscous liquid and an elastic solid. Like elastic materials, viscoelastic materials revert back to their initial shape after deforming once the stress causing the deformation is removed. However, similar to viscous fluids, they also feature hysteresis, which causes energy loss. A deformed viscoelastic body reverts back to its initial shape only a certain amount of time after the stress causing the deformation has been removed. When cyclically stressed, deformation lags behind the applied force, although the phase angle δ is smaller than for a purely viscous material. In purely viscous materials, deformation lags behind stress with a 90-degree phase angle. The phase angle is linked to the energy loss; the coefficient of energy loss, which translates the material's ability to dissipate energy, is $\tan(\delta)$. [12] The hysteresis of a viscoelastic material is demonstrated in figure 1. The figure depicts a force exerted on the material and the deformation of the material.

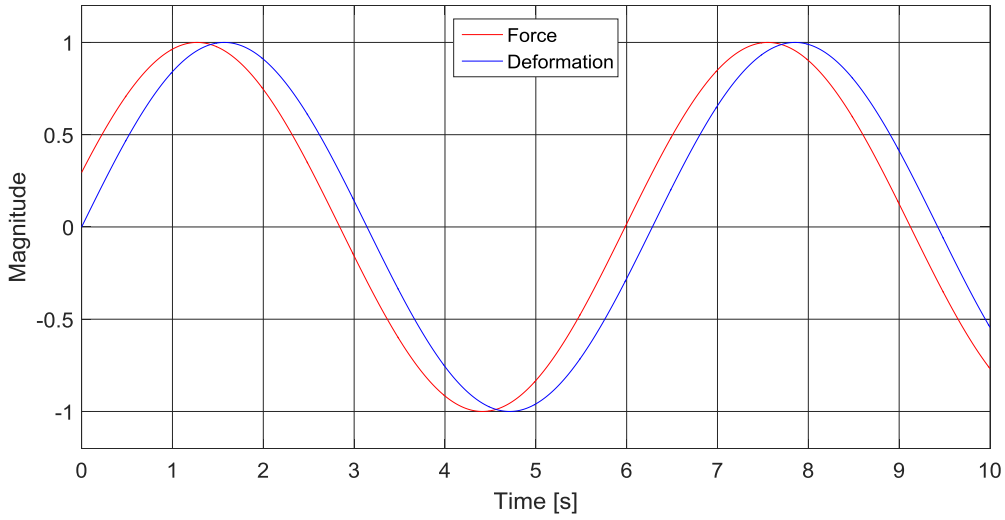

Figure 1 Viscoelastic behavior of rubber (figure is based on [5; 12])

The viscoelastic behavior of tire rubber is caused by vulcanized elastomers. They are made up of polymers, long molecular chains, which spontaneously become entangled with each other. [12] Vulcanization is a process in which a rubber or elastomer is obtained by transforming polymers into a viscoelastic solid that contains chemical crosslinked molecular networks [13]. When the polymers are vulcanized during the manufacturing process of tire rubber, sulphur bridges are created between them. An isolated polymer behaves elastically when deformed. However, the sulphur bridges in the network of polymers in tire rubber

cause the polymers to rub against each other when deformed. This gives the material its viscous component. The formulation of elastomeric compounds affects their viscosity. [12]

2.1.2 Influence of Temperature and Stress Frequency

In addition to the energy loss and hysteresis, the behavior of rubber is dependent on its rigidity which is characterized by the modulus of the rubber. Modulus describes the stress-to-strain ratio of a material. In order to achieve maximum tire-road friction, the tire rubber compound should have a moderate modulus and highest possible hysteresis. [12]

The modulus, energy loss, and hysteresis of a tire rubber compound are dependent on the stress frequency and the temperature of the rubber. Stress frequency refers to the frequency with which the stress is applied to the rubber. The viscoelastic nature of rubber disappears in high and low temperatures as well as with high or low stress frequencies. [5]

When the stress frequency is low, tire rubber deforms slowly. Thus, there is little damping, and the rubber functions elastically. This also means that energy losses and hysteresis are low. Furthermore, the modulus is also low. On the other hand, when the stress frequency is high, the polymer chains in the compound do not have enough time to revert back to their equilibrium, resulting in the compound behaving in a glass-like manner and having a high modulus. This also causes energy losses and hysteresis to be low. At moderate stress frequencies, the rubber has a moderate modulus and it behaves viscoelastically. Thus, hysteresis and energy losses are high. As a consequence, moderate frequencies are most favorable for grip. [12] The effect of stress frequency on the modulus and the energy loss of rubber is demonstrated in figure 2.

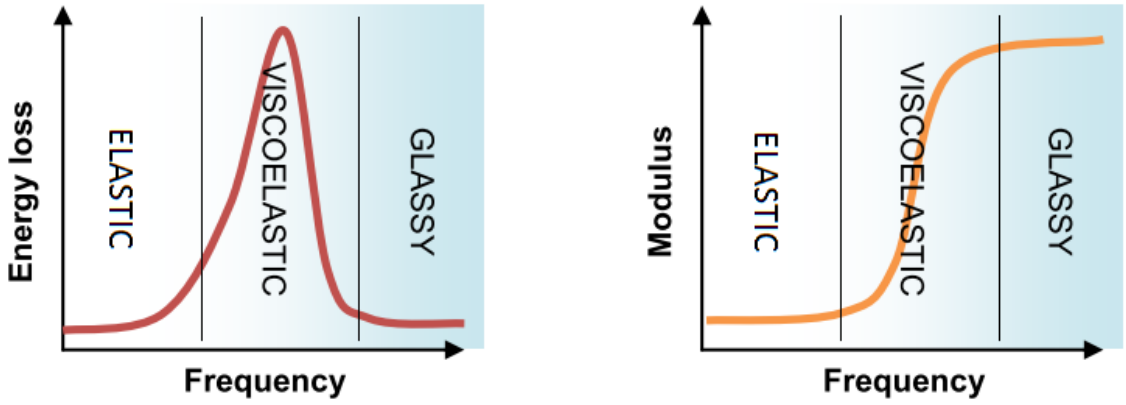

Figure 2 Influence of stress frequency on rubber (figure is based on [14])

Temperature and stress frequency affect the properties of rubber in opposite ways. A low temperature has the same effect as a high stress frequency, and vice versa. The effect of temperature is caused by changes in molecular mobility. The higher the temperature is, the quicker the molecular chains can return to their state of equilibrium. [12] The effect of temperature is displayed in figure 3.

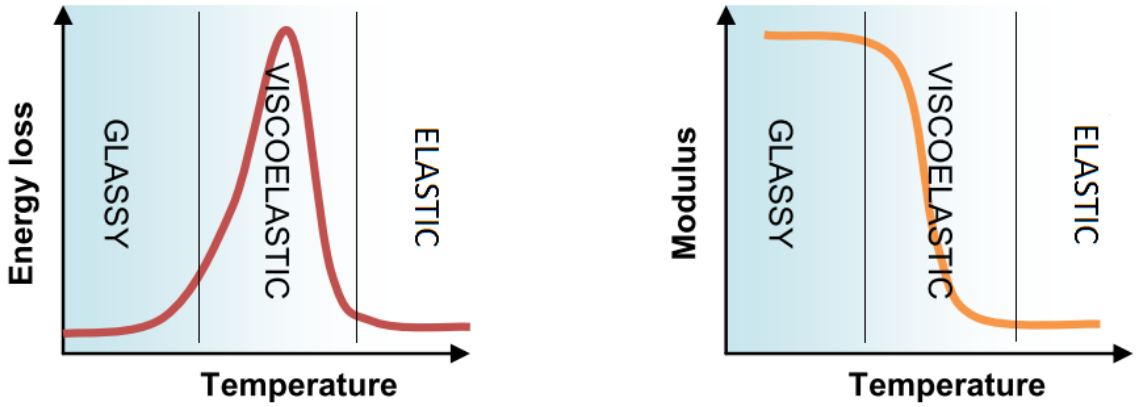

Figure 3 Influence of temperature on rubber (figure is based on [14])

The temperature at which energy loss and hysteresis are highest is called glass transition temperature. When the temperature falls below this value, the rubber compound starts to become glass-like. The higher the stress frequency is, the higher the glass transition temperature is. This relationship between them is due to a balance between molecular velocity and speed of deformation. The material will behave in a glass-like manner if the speed of deformation is higher than the speed at which the molecules can move in their environment. If the molecules can move at a speed that is faster than the speed of deformation, the material will then appear flexible. [12]

2.2 Tire Design

2.2.1 Tire Construction

The most significant functions of tires include: transmitting driving and braking torque and providing cornering force, load-carrying capacity, cushioning, and dampening. Additionally, tires should, among other requirements, have low rolling resistance, resist abrasion, provide good traction and minimum noise, and be durable throughout their expected life span. [5; 15]

A passenger car tire consists of various parts and subassemblies, all of which serve to ensure that the product meets its intended design and performance requirements. Tubeless pneumatic radial ply tires are the most widely used type of tire in passenger cars [13; 16]. The structure of such a tire is presented in figure 4. The carcass of the tire consists primarily of textile or steel cords (plies) laid radially between the bead wires. The ends of the plies are wrapped around the bead wires and turn up the sidewall, which anchors the body ply to the bead bundle and allows the ply turn up to provide added reinforcement for the lower sidewall region. The sidewall protects the carcass from side scuffing, controls ride characteristics, and assists in tread support. [13; 15] The bead wires secure the radius of the chafer area, making sure that the tire stays on the rim [5].

The inner liner lies underneath the plies. It makes the tire airtight. [5] The inner liner is made of butyl rubber or halogenated derivatives of such polymers. Belts, made of steel or textile, lie in between the plies and the tread. They serve to longitudinally stiffen the carcass and to improve wear performance, handling response, damage resistance, and protection of the ply cords. The tread is the part of the tire that is in contact with the road. In addition to wear resistance, it must provide traction, wet skid, and good cornering characteristics while

maintaining low noise generation and heat buildup. The tread can feature various different shapes, grooves, and sipes that significantly affect the performance characteristics of the tire. [5; 15]

Nylon overlays, the belt wedges, and the tread base lie between the belts and the tread. The nylon shrinks as it heats up, which prevents the tire from expanding at high velocities. [5] The belt wedge is made of a high-adhesive rubber compound. Its purpose is to improve tread wear and durability. The tread base is a rubber compound that is used to reduce rolling resistance and to enhance adhesion between the belts and the tread. It can also improve heat dissipation. [15]

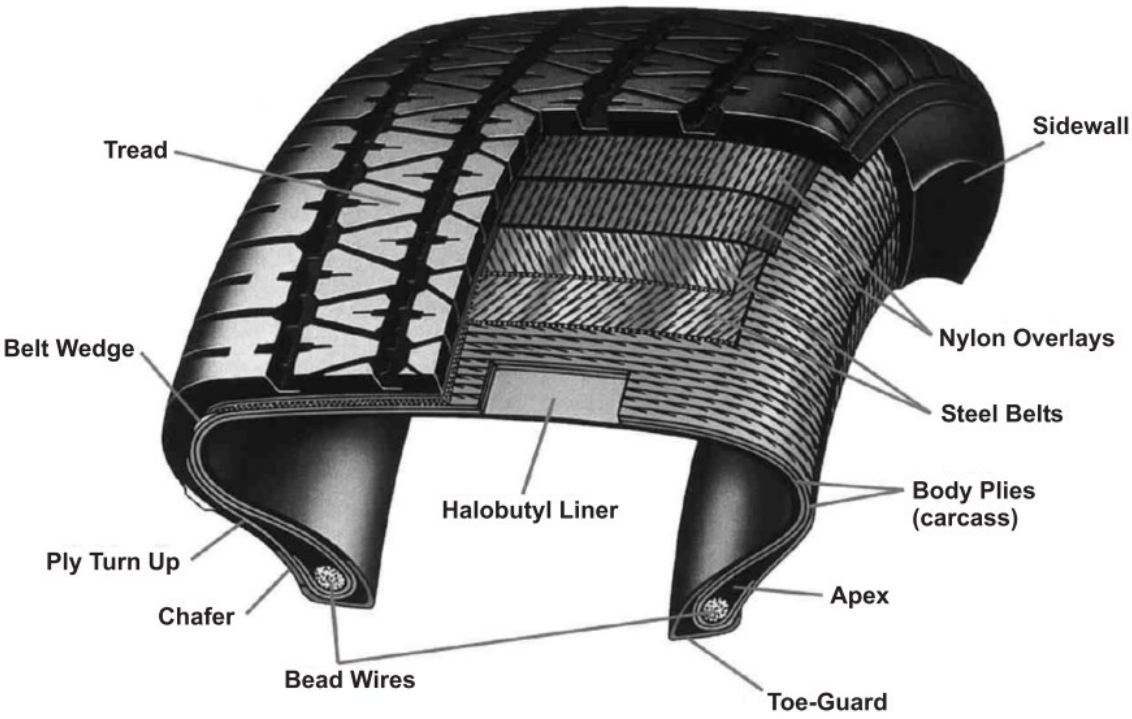

Figure 4 Cross section of a passenger car radial ply tire [15]

2.2.2 Tire Tread Patterns

The tread pattern drastically affects the performance characteristics of the tire. The tire's rolling resistance, stability, wear, and ability to produce longitudinal and lateral forces all depend on the pattern. [17] Some of the more common types of tread patterns are displayed in figure 5.

The tread patterns are defined by two types of cuts: grooves and sipes. Grooves are the large and deep cuts in the tread. They are fundamental in defining the tire's characteristics. Sipes are shallower grooves that enhance the performance of the tire. They are particularly significant in improving winter tire grip in icy conditions and braking control on wet roads. [17]

The longitudinal groove pattern along the circumference of the tire is called the rib shape. It serves to reduce rolling resistance and enhance directional stability while adversely affecting braking and acceleration capabilities on wet roads. The lug shape is a groove pattern

perpendicular to the circumference of the tire. It improves traction and braking performance. However, the lug shape does also increase noise and rolling resistance. The rib-lug shape takes the best of both worlds by providing directional stability with the rib shape and enhanced traction and braking capabilities due to the lug shape on the shoulders of the tire. [17; 18]

The block shape, which features a pattern of independent blocks, increases tire wear but improves stability on snow covered or wet roads. It is capable of dispersing water effectively. The block shape is suited for winter or all-season tires. An asymmetric pattern is intended for high performance tires. It allows for improved high speed cornering due to greater contact area. [17] The purpose of a directional pattern is to improve friction in wet conditions, though grip on wet roads and resistance to aquaplaning are largely dependent on the depth of the grooves rather than the shape of the pattern [17; 18; 19].

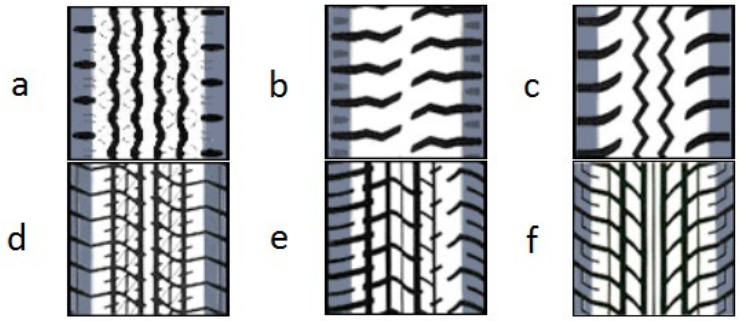

Figure 5 Tread patterns: a) rib shape, b) lug shape, c) rib-lug shape, d) block shape, e) asymmetric pattern, and f) directional pattern [17]

While summer tires offer excellent performance on both dry and wet roads in warm temperatures, they do not function effectively in sub-zero, snowy, icy, and muddy conditions. Consequently, specialized tires have been developed for different road and weather conditions. [20] As discussed earlier, temperature significantly influences the behavior of rubber. Thus, different compounds are needed for cold conditions. There are two main types of winter tires: studded and non-studded. Studded winter tires feature small pieces of strong metal called studs that dig into ice, providing increased traction. They can, however, damage the road if it is not covered in ice, which is why their use is regulated. [5; 21] Studded tires are even banned in some countries, such as Germany [5]. Non-studded snow tires have increased in popularity in recent years due to improvements in rubber compounds and tire tread designs. Their treads are made of rubber compounds that maintain flexibility in cold temperatures, which helps with traction on snowy, icy, wet, and dry surfaces. The tread patterns feature block shapes and thousands of little sipes that act as biting edges on ice. [20; 21]

All-season tires are designed to be used all year round. They do not perform as well as winter tires in severe conditions due to their tread being made of a harder rubber compound, but their tread patterns are designed to give better traction than summer tires in snowy and icy conditions. All-season tire tread patterns feature block shapes and sipes. [20; 22] All-weather tires are similar to all-season tires, but they use slightly softer compounds, making them perform better in cold conditions [22].

2.3 Tire Friction Mechanisms

As discussed previously, hysteresis occurs in rubber due to rubber's viscoelastic nature. Though hysteresis is often considered an adverse phenomenon in many applications, in tire dynamics it is fundamental to grip [5]. Hysteresis functions as a friction mechanism in car tires largely due to the stress frequency excitation caused by the roughness of the road. When the rubber slides over a spot of surface roughness, it deforms. However, once it has passed over that spot, it does not immediately return to its initial form due to hysteresis, meaning that some energy is lost. This causes an asymmetrical stress field in the rubber, as demonstrated in figure 6. The resultant force has a component that opposes the motion of the rubber. [12] Even if the road surface was absolutely smooth with no roughness, the hysteresis of the rubber would cause an asymmetrical overall stress field in the contact patch of the rubber, resulting in a force component opposing the motion [5].

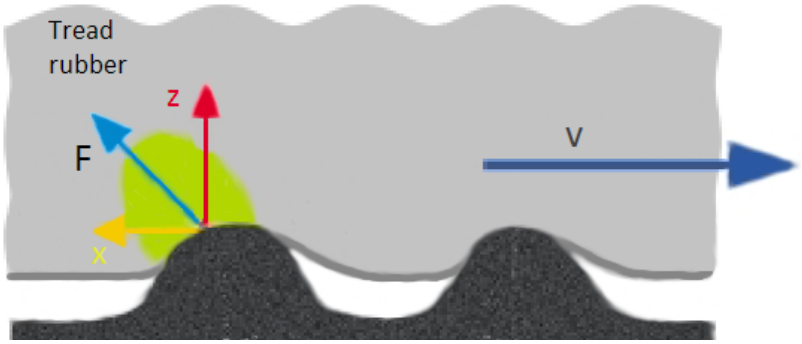

Figure 6 Force caused by hysteresis of tire rubber [12]

The other major mechanism in tire-road friction is molecular adhesion. It is caused by Van der Waals bonds between the rubber and the road. These bonds form, stretch, and then break cyclically, which results in forces opposing the motion of the rubber. [12] Adhesion mostly depends on the materials and the area of the contact. It also requires the rubber to be in direct contact with the ground, with the distance between their molecules being less than 10^{-6} mm. This means that the road must be clean and dry in order for adhesion to take effect. [5; 12]

One important property of tire rubber is that the friction coefficient between the rubber and the road decreases as the vertical load on the tire increases. This is called load sensitivity. [23] It is caused by the area of contact between the two materials not following the load linearly. As the load increases, the rubber increasingly fills the indentations of the road, increasing the contact area. However, the more the rubber fills the indentations, the less it can fill them further. Consequently, the relationship between the load and the size of the contact area is not linear. This limits the friction coefficient because one of the main components of the tire-road forces, adhesion, is dependent on the contact area. [5]

2.4 Influence of Road Conditions

2.4.1 Influence of Surface Texture

The Permanent International Association of Road Congresses (PIARC) established in 1987 that the texture of the road can be divided into three categories based on the wavelength and peak-to-peak amplitude of the deviations of the pavement surface from a true planar surface. These categories are presented in table 1. The mega-texture, which does not affect the tire-

road friction in any significant way, describes the waviness of the pavement surface. Its wavelengths are in the same order of size as the length of the tire-road contact patch. The macro-texture is defined by the shape, size, and gradation of the mineral aggregate particles used in the pavement material. The micro-texture describes the roughness of the road at microscopic level. [19]

Table 1 Road texture categories (table is based on [19])

	Micro-texture	Macro-texture	Mega-texture
Wavelength (λ)	$\lambda < 0.5$ mm	$0.5 \leq \lambda < 50$ mm	$50 \leq \lambda \leq 500$ mm
Peak-to-peak amplitude (A_p)	$0.001 \leq A_p \leq 0.5$ mm	$0.1 \leq A_p \leq 20$ mm	$0.1 \leq A_p \leq 50$ mm

It has been observed that variations in the tire-road friction coefficient on dry surfaces are reasonably small. The coefficient can vary between 1 and 1.3. [12] The roughness of the road influences the amount of tire-road friction generated by both the hysteresis of the rubber and the molecular adhesion between the rubber and the road. A higher degree of roughness increases the amount of deformation occurring in the rubber, thus increasing hysteresis, which in turn increases friction. However, a rougher surface reduces the area of contact, decreasing the molecular adhesion. [5]

2.4.2 Influence of Water, Snow, and Ice

The roughness of the surface has a much more significant effect on the friction in damp and wet conditions. The friction coefficient can vary between 0.1 and 0.9 in such conditions, depending on the texture of the surface. When the surface is damp, a film of water between the rubber and the road prevents molecular adhesion from occurring unless the film is broken. [12] If the surface has significant microroughness, spots of high pressure will develop between the rubber and the road, which will break the film of water, allowing molecular adhesion to contribute to the friction. Hysteresis continues to provide friction with the aid of the macroroughness of the road, although the water on the road can decrease the effect by effectively reducing the roughness. [5] The micro-texture affects the level of friction on a damp road more than the macro-texture. A surface that is smooth on both macro and micro-level provides the lowest amount of friction in damp conditions. [12] Additionally, aquaplaning can occur at high speeds on wet surfaces. It has been experimentally shown to occur when the hydrodynamic pressure exceeds the tire pressure. [5] As water between the rubber and the road clearly has an adverse influence on the level of friction, passenger car tires must be designed in such a way that they disperse water as effectively as possible. This can be achieved by adjusting the shape of the contact patch and the tread pattern. [12]

On an icy surface, the tire-road friction depends largely on the amount of water on top of the ice cover. The lack of friction is caused by the friction between the rubber and the road melting the ice. The lower the temperature is, the drier the ice is and the less the ice melts as a result of the friction, thus providing better grip. [5]

There are various different types of snow. Compact and cold snow behaves similarly to dry ice. Melting snow, on the other hand, is comparable to a highly viscous fluid. When a tire

bites deep into snow, the amount of friction depends on the shear strength of the snow. [5] Snowy and icy conditions place special demands on the tires, requiring soft rubber compounds that maintain a moderate modulus and hysteresis in low temperatures and tread patterns that feature block shapes and sipes in order for the tire to bite onto the road as effectively as possible [12; 20].

3 Vehicle Dynamics

Vehicle dynamics can be divided into three subcategories: longitudinal, lateral, and vertical dynamics. This thesis mainly focuses on longitudinal and lateral dynamics. This chapter introduces the basic terminology of vehicle dynamics relevant to the topic at hand while presenting the linear single-track model, which is used to analyze the lateral behavior of vehicles. A modified version of the model is later used in creating the friction estimation algorithm in Chapter 7.

The coordinate system of a vehicle is presented in figure 7. The origin of the system is situated at the center of gravity of the vehicle. Longitudinal motion is the motion in the direction of the x-axis. Lateral motion is the motion in the direction of the y-axis, which is perpendicular to the vehicle center plane. The z-axis is parallel to the direction of the vertical motion. The corresponding velocities are u, v, and w. The rotations around these axes are called roll, pitch, and yaw respectively. [5; 16]

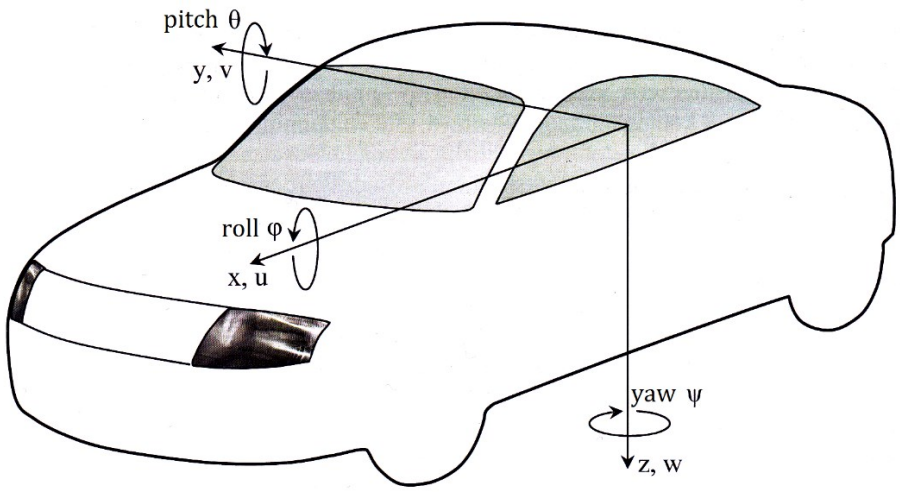

Figure 7 Vehicle coordinate system [5]

Longitudinal dynamics is usually associated with the performance capabilities of the car. Typical points of interest in longitudinal dynamics are the top speed, acceleration, factors limiting the acceleration, the effect of road inclination, and longitudinal load transfers. [5] The longitudinal acceleration capabilities of a vehicle are affected not only by the power curve of the engine but also by the mass of the vehicle and its distribution, the number of driven wheels, the suspension, the aerodynamic drag, the rolling resistance of the tires, the inclination of the road, and the road conditions. While the rolling resistance and the aerodynamic drag waste energy by turning it into heat, driving uphill causes work to be turned into potential energy as the car combats the gravity of Earth. [16] The suspension influences the longitudinal weight transfers and the ability of the vehicle to keep the tires in contact with the road on rougher terrain. Additionally, as a consequence of lateral slip, the lateral forces produced by the tires feature a component that opposes the longitudinal motion of the vehicle. [5]

Lateral dynamics, on the other hand, is typically associated with the concept of handling. It involves the lateral and yaw motions of the vehicle. The main points of interest in lateral dynamics are the lateral and yaw responses of the vehicle to the driver's steering and pedal

inputs. The vehicle should respond quickly enough to the inputs such that the driver can adjust the trajectory of the vehicle with relative ease. On the other hand, the response should not be too rapid in order for the vehicle to be easily controllable and to maintain stability. [5]

Vertical dynamics is commonly linked to the concept of ride comfort. However, the suspension of the vehicle also dictates the roll and pitch behavior of the vehicle, meaning that the suspension significantly influences the lateral and longitudinal weight transfers, thus affecting the lateral and longitudinal dynamics of the vehicle. [5]

This chapter also discusses the topic of nonlinear tire dynamics and the limitations it puts on vehicle performance and handling. Longitudinal and lateral tire dynamics also drastically affect one another, which further limits the capabilities of the vehicle. Other factors, such as tire pressure and temperature, load sensitivity, suspension geometry, and road conditions, further complicate the force production characteristics of tires. [24] Many different tire models have been developed to describe these characteristics [5].

3.1 Linear Single-Track Model

The single-track model, also known as the bicycle model, combines the lateral dynamic properties of the wheels on one axle to form one effective wheel. It is used to analyze the lateral behavior of vehicles. [16] The free body diagram of the basic form of the single-track model is presented in figure 8. The purpose of the linear version of the model is to examine the lateral behavior of the vehicle in the linear range of the tires. The model is based on various limitations and assumptions [23; 25]:

- The road surface is flat and level
- The steering system is either ignored or assumed to be rigid
- No lateral or longitudinal load transfer
- No rolling or pitching motions of the body
- The vehicle structure is rigid, including the suspension system
- Linear range tires
- Steering and slip angles are small
- Constant forward velocity
- The effect of longitudinal tire forces on lateral tire forces is ignored
- No aerodynamic effects

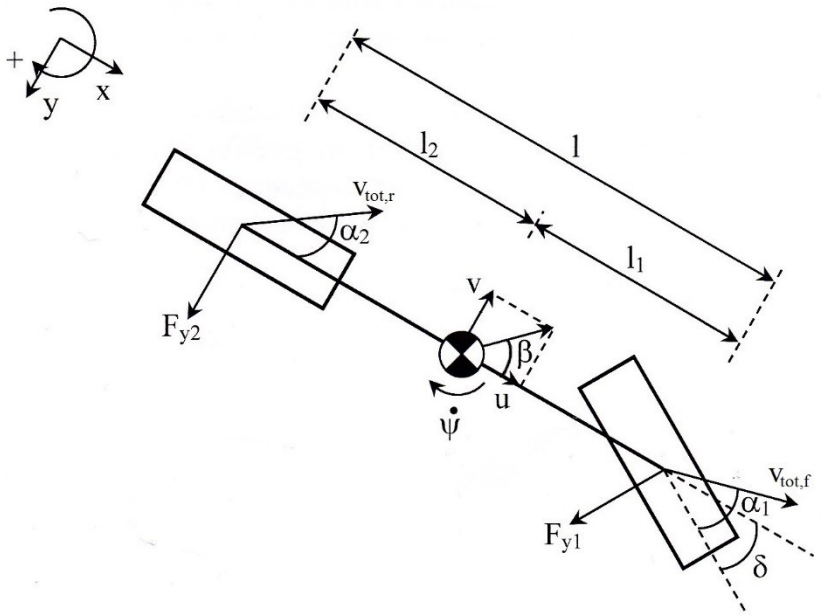

Figure 8 Single-track model of a vehicle sliding towards the outside of a corner [5]

Longitudinal velocity u is constant for every point of the vehicle in the model. The total lateral velocity of any given point consists of two components: the lateral velocity at the center of gravity v and the yaw rate $\dot{\psi}$ multiplied with the corresponding distance from the CoG. [5]

The Newton's equations of motion for the single-track model read [5]:

$$\sum F_x = 0, \tag{3.1}$$

$$\sum F_y = ma_y = F_{y1} + F_{y2}, \tag{3.2}$$

$$\sum M_z = I_{zz}\ddot{\psi} = l_1 F_{y1} - l_2 F_{y2}. \tag{3.3}$$

In these equations, a_y is the lateral acceleration of the vehicle, F_{y1} and F_{y2} are the lateral forces produced by the tires on the front and the rear axle respectively, $\ddot{\psi}$ is the time derivative of the yaw rate, also known as yaw acceleration, I_{zz} is the moment of inertia around the vertical axis at the center of gravity, and l_1 and l_2 are the distances of the front and the rear axle from the center of gravity. [5]

The lateral acceleration at the center of gravity can be defined as:

$$a_y = \dot{v} + u\dot{\psi} \tag{3.4}$$

where $\dot{v}$ is the time derivative of the lateral velocity at the center of gravity. The multiplication of u and $\dot{\psi}$ is equal to the centripetal acceleration of the vehicle when the CoG has no lateral velocity. [5] Consequently, equation (3.2) can then be written as:

$$\sum F_y = m(\dot{v} + u\dot{\psi}) = F_{y1} + F_{y2}. \tag{3.5}$$

The tire slip angle α is the angle between the centerline and the total velocity of the tire. In figure 8, the total velocities of the front and rear axle are denoted by $v_{tot,f}$ and $v_{tot,r}$ respectively. A tire is considered to be in its linear range when the relationship between the lateral force and the slip angle is linear. The linear range only covers small slip angles. The relationship between the lateral force and the slip angle in the linear range is described by the lateral stiffness C_i of the tire, as shown in equation (3.6). In the case of the single-track model, C_i describes the combined lateral stiffness of both of the tires on an axle. [5]

$$F_{yi} = C_i \alpha_i \tag{3.6}$$

The vehicle side slip angle β is the angle between the centerline of the vehicle and the total velocity of the center of gravity. It is calculated as follows [5]:

$$\beta = \tan^{-1}\left(\frac{v}{u}\right). \tag{3.7}$$

The yaw rate gain, which describes the relationship between the yaw rate and the steering angle, can be derived from the linear single-track model. It can be written as:

$$\frac{\dot{\psi}}{\delta} = \frac{ulC_1C_2}{l^2C_1C_2 - mu^2(l_1C_1 - l_2C_2)} \tag{3.8}$$

where l is the wheelbase of the vehicle, C_1 is the lateral stiffness of the front axle, and C_2 is the lateral stiffness of the rear axle. A maximum value exists for the yaw rate gain of an understeering car. The speed at which the maximum yaw rate gain occurs, which is also known as the characteristic speed u_{char}, can be found by differentiating equation (3.8) with respect to u and finding the value of u at which the derivative is zero [5]:

$$u_{char} = \sqrt{\frac{l^2C_1C_2}{m(l_2C_2 - l_1C_1)}}. \tag{3.9}$$

The characteristic speed is used in the control logic of ESP systems, which will be discussed in Chapter 4 [4].

3.2 Nonlinear Tire Dynamics

A tire generates forces and moments in every direction. They are presented, along with the general tire coordinate system, in figure 9. The total velocity of the tire is denoted by v_{tot} and the rotational speed by Ω in the figure. The vertical force F_z is the vertical load exerted on the wheel. The longitudinal force F_x is the force that generally accelerates and brakes the vehicle. The lateral force F_y is largely responsible for the lateral and yaw motions of the vehicle. The self-aligning moment M_z is caused by the resultant force at the contact patch not being located at the center of the patch. The overturning couple M_x is caused by the load on the wheel not being distributed evenly horizontally. [5] The rolling resistance moment M_y is caused by the hysteresis in the tire [24]. In this thesis, the tire forces are the most important outputs of the tire.

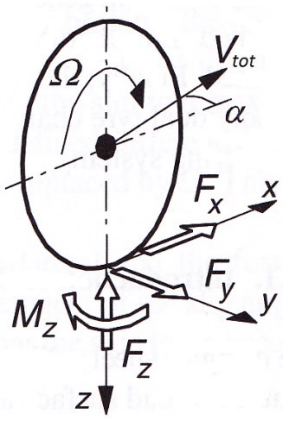

Figure 9 Tire forces and moments [24]

3.2.1 Lateral Dynamics

The lateral coefficient of friction is defined as:

$$\mu_y = \frac{F_y}{F_z}. \tag{3.10}$$

As mentioned previously, the linear range only covers small slip angles. As the slip angle increases, the portion of the tread rubber in the contact patch that is sliding, rather than merely stretching, increases. With low slip angles, only a small portion of the tread is sliding at the trailing edge of the contact patch. When the slip angle increases, the point at which the tread rubber starts sliding moves towards the leading edge of the contact patch. At a certain slip angle, the lateral force reaches its maximum, and increasing the angle further will only reduce the force. Thus, the area past the peak is considered the unstable region of the tire. [12]

Load sensitivity, which was discussed in Chapter 2, also affects the lateral force, as it causes the friction coefficient to reduce as the vertical load increases. The overall shape of the friction coefficient versus slip angle curve changes with the load as well, including the location of the peak. [23] Figure 10 demonstrates the relationship between the lateral friction coefficient and the slip angle, and the effect of load sensitivity.

The lateral force is also influenced by the camber angle (γ) of the tire. Camber is defined as the angle between a tilted wheel plane and the vertical, as shown in figure 11. The camber angle is positive if the wheel leans outward at the top relative to the vehicle, or negative if it leans inward. [23] The angle changes during body roll, the extent of the change depending on the suspension [25]. Camber angle can increase the peak lateral force the tire yields due to the effect it has on the shape of the contact patch. Typically, negative camber angles are used as they tend to increase the lateral force produced by the tires on the outside of the corner. A tire that has camber also produces some lateral force even when there is no slip angle. [23]

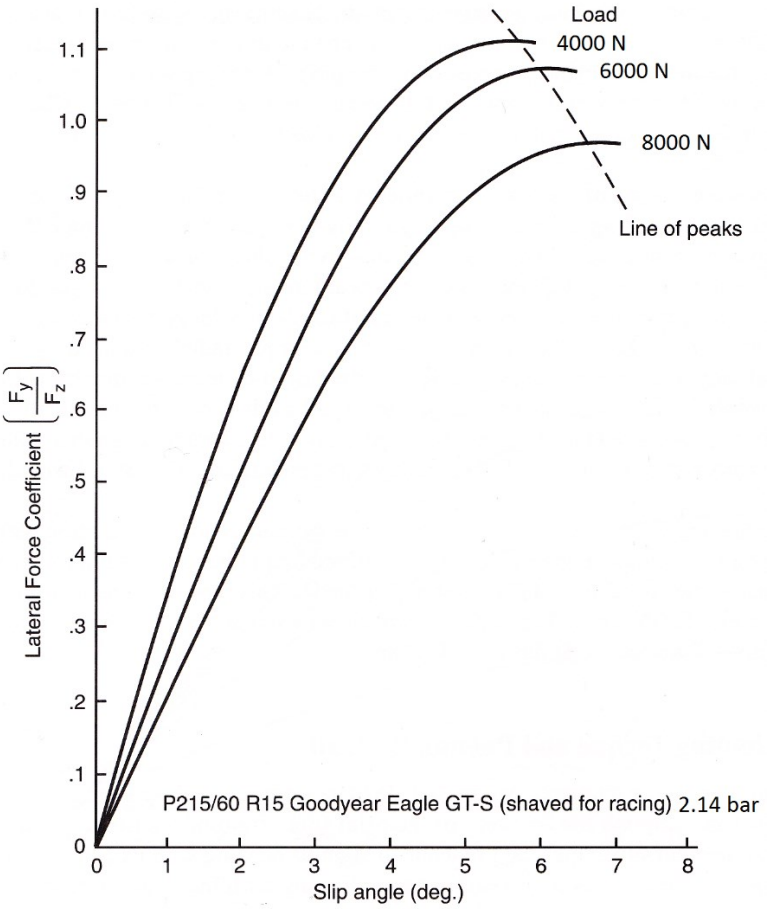

Figure 10 Lateral friction coefficient vs slip angle [23]

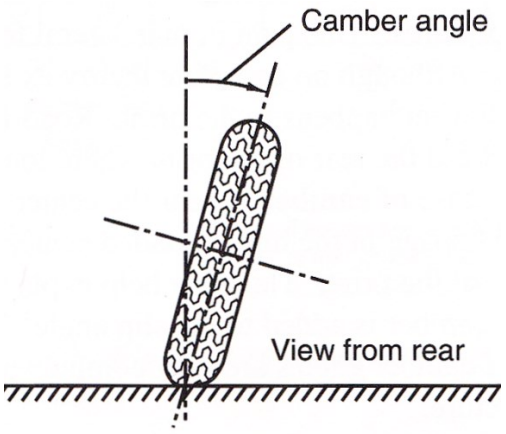

Figure 11 Camber angle [23]

The lateral force produced by the tire also depends on other factors, including tire non-symmetries. Conicity is a lateral force component produced by the tire due to its shape being slightly conical, meaning that the radius of the tire reduces towards the other edge. This is generally caused by an off-center belt in a radial tire. The direction of the conicity force is always the same regardless of the direction the tire is rotated. [23] Ply steer is a lateral force component that is caused by the alignment of the plies during tire deformation [5]. The direction of this force component depends on the direction the tire is rotated in [23].

3.2.2 Longitudinal Dynamics

The longitudinal friction coefficient is defined as [12]:

$$\mu_x = \frac{F_x}{F_z}. \tag{3.11}$$

The longitudinal force produced by the tire depends on the amount of longitudinal slip. Slip ratio κ describes the longitudinal slip:

$$\kappa = -\frac{v_x - \Omega r_d}{v_x} \tag{3.12}$$

where v_x is the longitudinal velocity of the tire (i.e., the velocity along the direction of the x-axis in figure 9). The dynamic rolling radius r_d is defined as the ratio between the longitudinal velocity and the rotational speed of the tire when the tire is rolling freely with no longitudinal slip. [5] As can be deduced from equation (3.12), the value of the ratio is positive when the wheel slips during acceleration. The positive slip ratio during acceleration is also known as drive slip. During heavy braking, the wheels experience a negative slip ratio. A fully locked up wheel has a slip ratio of -1. The absolute value of the slip ratio during braking is called brake slip. [3]

The relationship between the longitudinal friction coefficient and the slip ratio functions similarly to that between the lateral coefficient and the slip angle. Sliding begins at the trailing edge of the contact patch, and as the absolute value of slip ratio increases, the point at which the tread begins to slide moves towards the leading edge of the contact. At a certain slip ratio, the friction coefficient reaches its maximum and declines beyond that. [12] Load sensitivity influences the longitudinal dynamics of a tire in much the same way it affects the lateral dynamics [23].

3.2.3 Combined Dynamics

A tire cannot produce maximum lateral and longitudinal forces simultaneously because the friction between the tire and the road is shared between the two force components. The overall tire-road friction coefficient can be defined as:

$$\mu_t = \sqrt{{\mu_x}^2 + {\mu_y}^2} = \frac{\sqrt{F_x^2 + F_y^2}}{F_z}. \tag{3.13}$$

The terminology relating to the use of tire-road friction is explained with a simple version of the friction ellipse in figure 12. The maximum overall friction capabilities are called friction potential. The amount of available friction is the difference between the currently used tire-road friction and the friction potential. [26]

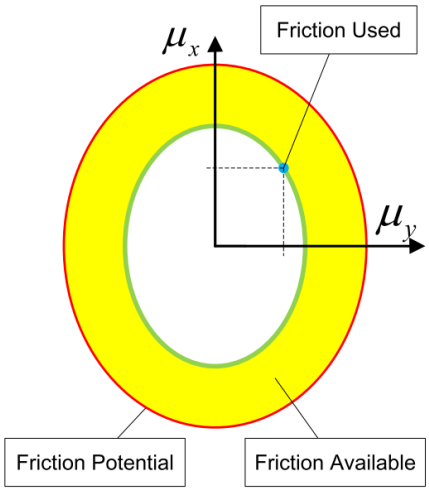

Figure 12 Friction ellipse and terminology [14]

The friction potential is slightly elliptical rather than perfectly round because the maximum longitudinal friction coefficient is usually slightly higher than the maximum lateral coefficient. The production of longitudinal force is also more resistant to effects of the slip angle than the production of lateral force is to effects of the slip ratio, as shown in figure 13. [12] The friction ellipse can also be plotted with different amounts of slip visible, an example of which is given in figure 14. In the ellipse, lateral force is plotted as a function of longitudinal force with constant slip ratios and slip angles. The vertical load is constant as well. [5]

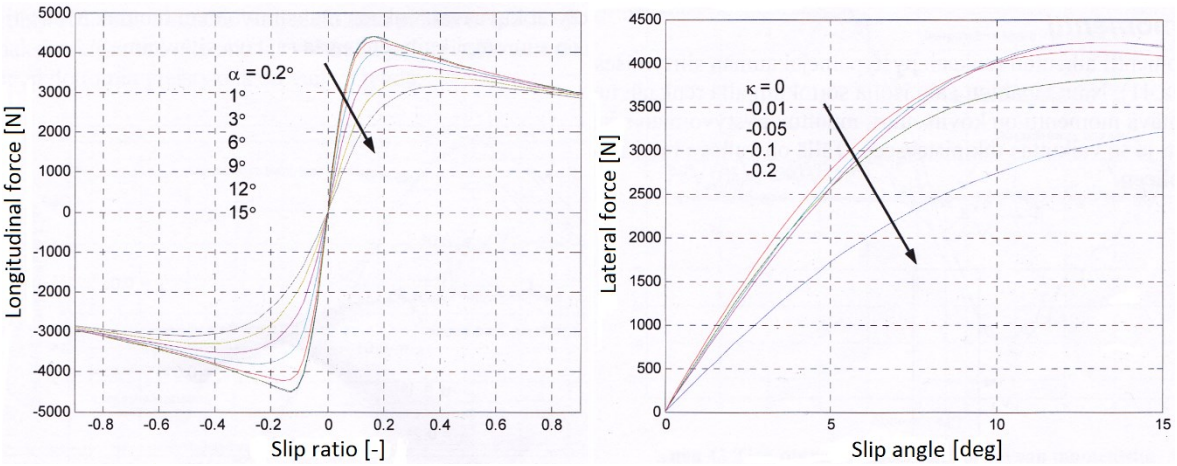

Figure 13 The effects of slip angle on longitudinal force and slip ratio on lateral force (5 kN load) [5]

Factors such as camber, conicity, and ply steer cause the tire to generate lateral force even with zero slip angle. Consequently, they also adversely affect traction and braking capabilities, as they use up some of the available friction, thus reducing the maximum longitudinal force the tire can produce.

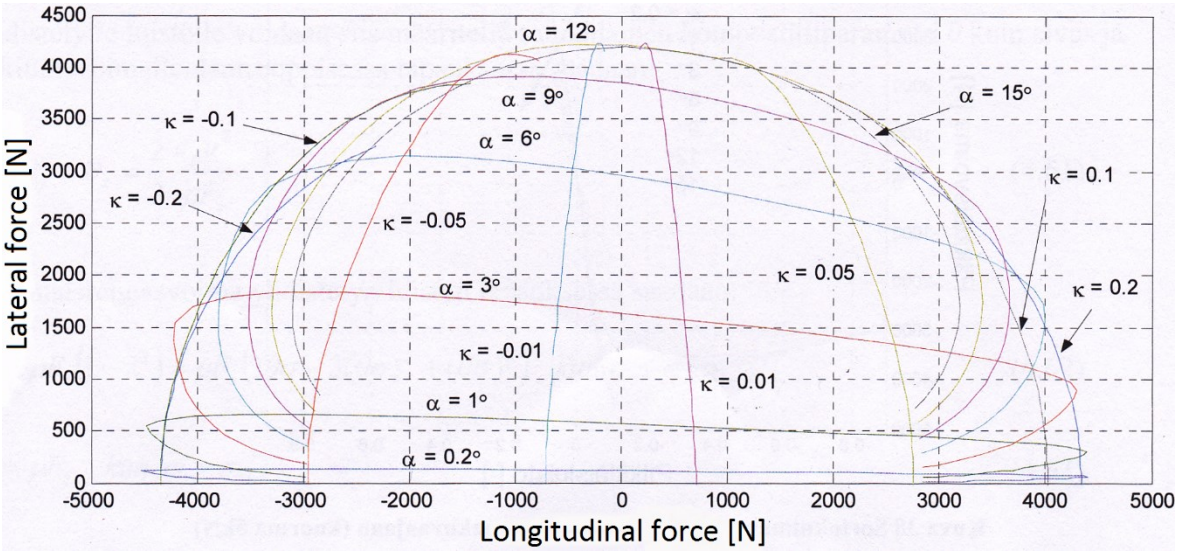

Figure 14 Friction ellipse (5 kN load) [5]

3.2.4 Influence of Winter Conditions

The maximum overall tire-road friction coefficient can vary between 0.05 and 0.6 in snowy and icy conditions. The conditions affect not only the maximum coefficient but also the shape of the force versus slip curves. [5] The maximum coefficient depends on the depth of the fresh snow cover. The deeper the cover is, the lower the friction coefficient is. Tire-road forces tend to have less drop-off after the peak in the force-slip curves in snowy conditions. [27] On icy roads, the drop-off after the peak can be sharp, and the peak is reached with less slip than on snowy roads. The shape of the curves and the value of the maximum coefficient are also heavily dependent on the tires the vehicle is equipped with. Load sensitivity properties also vary significantly between different tires and conditions. [28] Saalimo tested three different winter tires in snowy and icy conditions in order to plot their lateral friction coefficient versus slip angle curves in reference [28]. Curves obtained for a certain tire in both icy and snowy conditions are presented in figure 15.

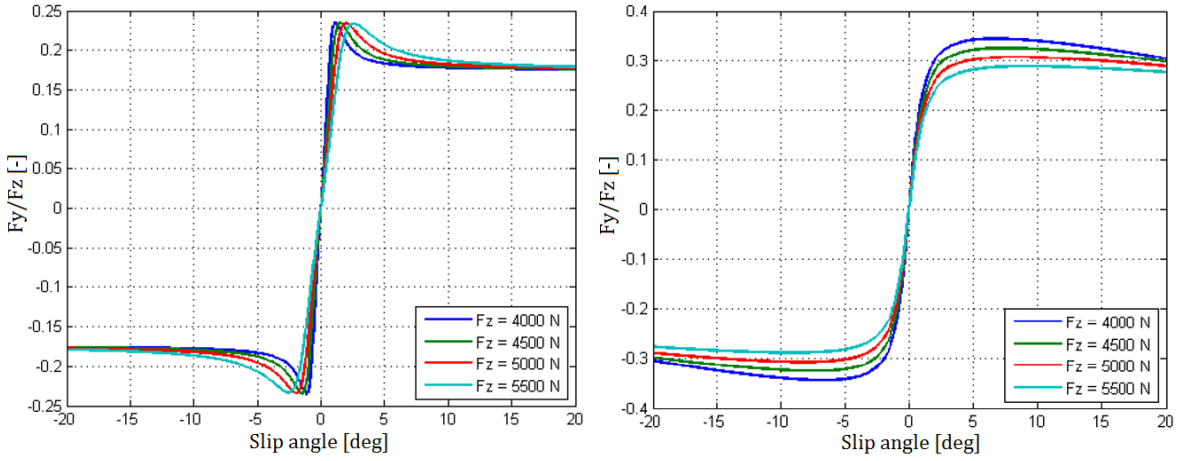

Figure 15 Lateral friction coefficient vs slip angle on ice (left) and snow (right) [28]

4 Background of Friction Estimation

The purpose of friction estimation is to obtain the current maximum overall tire-road friction coefficient, also known as friction potential, so that the control and safety systems of the vehicle can operate more effectively. Acquiring a relatively accurate estimation of the friction coefficient currently used by the tires is entirely feasible and can be executed in many ways. However, for most of the time during regular operation, passenger cars are not on the limits of friction, meaning that the measured current friction coefficient is not the same as the friction potential. Various diverse friction estimation methods have been developed. Some of them focus on trying to estimate when the car is on the limits of friction and then obtaining the current friction coefficient, while others try to estimate the friction potential with predictive techniques. The estimation methods can be categorized based on whether they try to obtain the friction coefficient with special sensors or estimate it from the motions of the vehicle using different tire and vehicle dynamics models. Additionally, the vehicle dynamics based estimation algorithms can either try to measure an average friction coefficient for all four tires of the car, or they can attempt to measure the tire-road friction for each tire individually. [10]

4.1 Direct Friction Sensors

Direct friction estimation methods employ special sensors to try to acquire information about the tire-road friction such that the friction potential could be determined from the sensor outputs without needing elaborate vehicle dynamics based estimation algorithms [10]. Many different approaches to friction estimation have been taken that can be classified as direct methods. Most of these methods rely on placing sensors inside the tire to measure different quantities. The term “intelligent tire” describes tires equipped with sensor systems that measure thermal and mechanical parameters while driving [29]. Measuring tire deformations is common, as they are closely related to the tire-road forces. Some of the early intelligent tire prototypes in the 1990s featured Hall sensors installed inside the tire to measure the deformations [7; 30]. Another early concept utilized a passive surface acoustic wave (SAW) sensor [29]. Magnetizing the sidewall of the tire to measure its deformations was also proposed [31] as well as measuring the wheel load and the vertical deflection of the tire with an ultrasonic sensor mounted on the wheel rim [32].

A more recent approach to direct estimation is using optical sensors to measure the deformations of the tire. The tire-road forces can then be calculated based on the deformations. A special optical sensor for measuring tire deformations, which was developed in the EU-funded Apollo project, is presented in [33]. The sensor, which consists of two parts, is installed inside the tire. A light-emitting diode (LED) is installed on the inner liner of the tire, and a two-dimensional position sensitive detector (PSD) is attached to the rim. When the tire deforms, the LED moves relative to the PSD, and the PSD measures the movement. The sensor is able to measure the deformation of the tire in all three directions. Lateral and vertical forces were calculated once per rotation from the deformations in laboratory test runs, and the results showed good correlation with reference measurements. [33] The sensor was also shown to function for detecting aquaplaning in reference [34]. However, according to Tuononen [33], a major issue with this sensor solution is that the tire can normally move on the rim, which would move the LED relative to the PSD. Fixing the tire to the rim would be challenging for mass production. Nonetheless, laser-based rim-mounted optical sensors for measuring tire deformations in laboratory and proving ground tests are commercially available [35]. Optical sensors can also be used to measure the road

directly and thus identify the road conditions [36]. Rim-mounted cameras can also be employed to measure tire deformations by using digital image processing techniques [37; 38]

Methods utilizing strain sensors inside the tire to measure deformations and forces have been proposed. The idea behind these methods is that the strain sensor deforms together with the tire, allowing for accurate measurements of the deformations of the tire. [39; 40] Moreover, Sergio et al. have developed a method that measures the capacitances and resistances of the steel belt arrays in a tire. As the tire and the belts deform, the capacitances and resistances change accordingly. [41] Using strain sensors to measure sidewall deformations has been proposed as well [42]. Additionally, rim-integrated force transducer systems that measure tire forces and moments with strain gauges are commercially available. These systems are only intended for proving ground tests, however. [43]

Embedding accelerometers into tires for obtaining information about the tire-road friction has also been researched [44; 45; 46; 47]. Niskanen and Tuononen proposed using three three-axis accelerometers attached to the inner liner of the tire in [44]. The accelerometers were attached side-by-side to cover half of the contact area in the lateral direction. The acceleration data was discovered to contain useful friction-related information, as the vibration level on an ice surface was higher than on dry concrete during the moments before the sensors would hit the contact patch. The friction between the rubber and the surface was thought to stabilize the vibration in the tire carcass. [44] Accelerometer signals can also be used to determine the length of the contact patch, which in turn contains information about the vertical load [44; 45]. Additionally, Savaresi et al. proposed that the phase shift between a wheel encoder and the pulse-like radial acceleration peaks experienced by the in-tire accelerometer could be used to determine the longitudinal tire-road force [45].

4.2 Vehicle Dynamics Based Friction Estimation

Direct friction sensors have limitations regarding cost, reliability, and robustness [10]. Additionally, supplying energy to the sensors in intelligent tires is challenging, as the use of batteries embedded inside tires is not practical [48]. Therefore, vehicle dynamics based friction estimation methods have been the topic of numerous pieces of research, and various types of such methods have been proposed. One such approach is the slip-slope method, which utilizes the relationship between the longitudinal friction coefficient and slip ratio to determine the friction potential. The longitudinal friction coefficient is proportional to the slip ratio for small slip ratios (i.e., in the linear range of the tire). The term “slip-slope” refers to the slope of the friction coefficient versus slip ratio curve in the linear range. The slip-slope varies with the maximum overall friction coefficient. Thus, the premise of the method is that by finding the value of the slope, the friction potential can be determined. The method requires estimating the longitudinal forces and vertical loads of the tires based on the acceleration of the car. Estimating the slip ratios is needed as well. [10] The slope also depends on inflation pressure, tire type, and temperature, among other factors. Uncertainties in these parameters can make it difficult to reliably estimate the friction potential based on small changes in the slope. [49]

Another approach to vehicle dynamics based estimation is to utilize the self-aligning torque of the steering system to estimate the friction potential [14; 50; 51; 52; 53]. The self-aligning torque is caused by the lateral tire-road force due to the caster trail. The caster trail is a consequence of the angle of the kingpin axis and of the acting point of the lateral force not

being located at the center of the contact patch, which is demonstrated in figure 16. [50] The position of the kingpin axis is determined by the kinematics of the axle [16]. The self-aligning torque reaches its peak value at much lower slip angles than the lateral force, thus allowing for estimating the friction potential even when the tire is not on the limits of its lateral force production capabilities [50]. In order to calculate the friction potential in this way, a tire model that describes the nonlinear characteristics of tires needs to be used. The Fiala tire model and the Brush model have been suggested to be utilized for this purpose. The suspension kinematics of the car must also be known. [14; 50; 51; 52; 53]

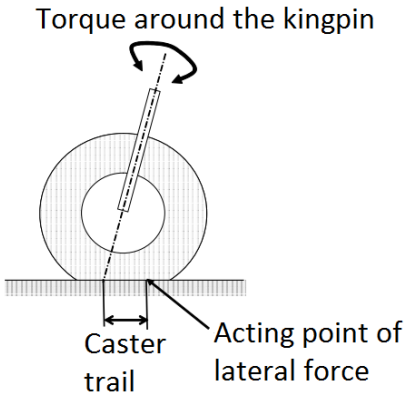

Figure 16 Caster trail and self-aligning torque [50]

Many more tire model based estimation methods have been devised. These methods are based on finding an optimal fit for the tire model to the tire force data that is estimated from the motions of the vehicle. Different tire models have been proposed to be used in these methods, such as the Dugoff tire model [54] and the Brush tire model [55; 56].

Methods that do not use elaborate tire models but rather only utilize vehicle models to estimate the friction potential have been created as well. Kiencke and Daiß proposed measuring longitudinal acceleration to calculate the longitudinal tire-road forces and vertical wheel loads. That way the friction potential can be found during heavy acceleration and braking maneuvers. [57] Kim et al. proposed using 6-DoF acceleration measurement in [58]. The premise of their method is that the longitudinal, lateral, and normal accelerations at each tire could be derived from the outputs of a 6-DoF accelerometer. The accelerations could be used to calculate the current longitudinal and lateral forces as well as the vertical loads for each tire, meaning that the current friction coefficients for each tire could then be computed as well. In order to calculate all the accelerations, a four-wheel vehicle and suspension model comprising of four quarter-car models was used. [58]

Additionally, several methods that employ different versions of the Kalman filter have been developed. The filter, the basic linear version of which will be taken a closer look at in Chapter 7, is an effective and recursive solution for filtering noisy discrete measurement data [59]. Expanded nonlinear versions of the filter have been used as a core component of algorithms that estimate friction and the lateral state of the vehicle with vehicle and tire models using velocity, acceleration, and yaw, pitch, and roll measurements. The versions used include the dual extended Kalman filter [60], the extended Kalman-Bucy filter [10], and the unscented Kalman filter [61; 62]. The Kalman filter and its nonlinear versions have also been used in friction and lateral state estimation algorithms that employ tire force sensors in addition to sensors that measure the motions of the vehicle [63; 64; 65].

4.3 Electronic Driver Aids and Friction Estimation

Electronic driver aids are mainly designed to improve the safety of passenger cars. The four most significant and common driver aids are discussed in this section. The significance of friction estimation for each of the systems is explained as well. Of the four systems, the anti-lock braking system, the traction control system, and the electronic stability program are considered active safety systems, as they stabilize the vehicle's handling response in critical situations. The adaptive cruise control is considered more of a convenience system. However, it does have an effect on safety as well due to maintaining safe gaps in traffic. [3]

4.3.1 Anti-lock Braking System

4.3.1.1 Components of Braking System with ABS

The components of a braking system fitted with ABS are presented in figure 17. The components in the figure are [3]:

1. Brake pedal
2. Brake booster
3. Master cylinder
4. Reservoir
5. Brake line
6. Brake hose
7. Wheel brake
8. Wheel speed sensor
9. Hydraulic modulator
10. ABS control unit
11. ABS warning lamp

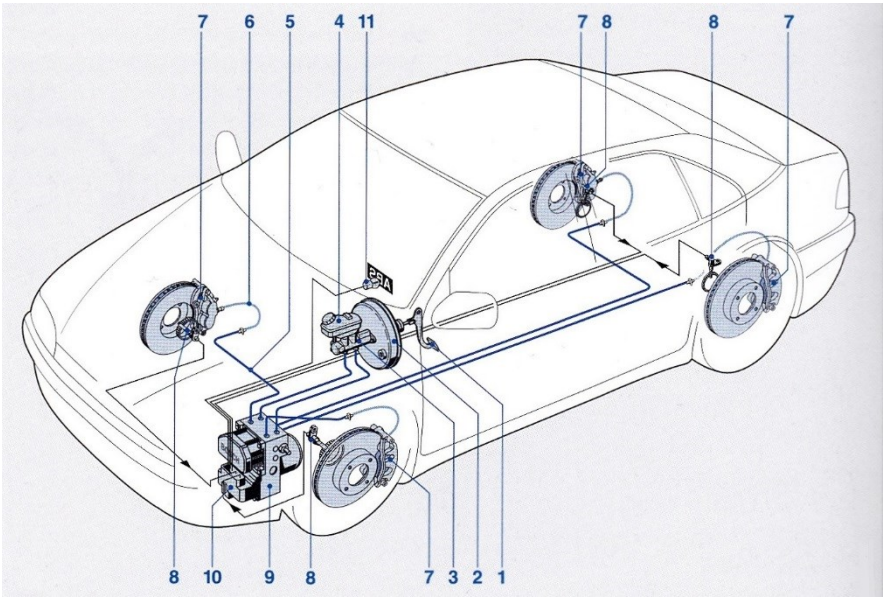

Figure 17 Braking system with ABS [3]

The wheel speed sensors, the hydraulic modulator, and the ABS control unit are specific to ABS, the rest of the components are conventional components of a braking system. The

brake booster amplifies the force applied by the driver's foot, reducing the effort required to brake the car. The master cylinder converts the mechanical force into hydraulic pressure in the brake circuits. The brake-fluid reservoir contains additional fluid for the brake circuits and also acts as an expansion that can accommodate volume fluctuations in the circuits. The lines and hoses bring the hydraulic pressure to the wheel brakes where the pressure is converted into friction. The brakes can be either drum or disk brakes. Disk brakes have been the standard at the front of the car for many years, but drum brakes can be used at the rear. [3]

4.3.1.2 Operating Principle of ABS

The purpose of an anti-lock braking system is to minimize braking distances while retaining steerability during heavy braking. The shortest braking distance possible can be achieved by maintaining the brake slips of the wheels as close as possible to the value that provides the highest longitudinal friction coefficient. When the slip of a wheel exceeds this value, the wheel quickly becomes unstable and locks up. [66] A locked up wheel produces less longitudinal force and provides next to no lateral force [5]. During heavy braking, all four wheels are slipping, which means that the velocity of the vehicle cannot be accurately obtained from any of them. As shown in equation (3.12), the velocity of the vehicle is needed in order to calculate the slip ratio of a wheel. The control unit does calculate a reference velocity during an ABS control sequence, but its accuracy is limited. [3]

The control unit uses the signals from the wheel speed sensors in calculating the control signals that it will send to the hydraulic modulator. The modulator contains solenoids and valves for controlling the pressures in the brake lines. [3] An ABS control cycle developed by Bosch is presented in figure 18.

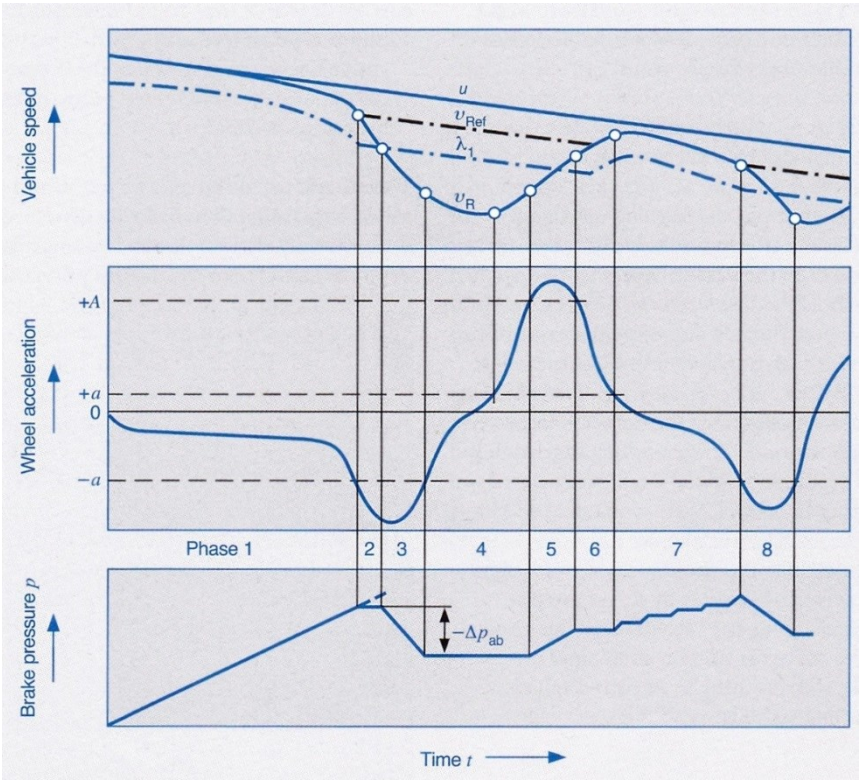

Figure 18 Bosch ABS cycle [3]

When the driver begins to brake, the velocity v_R, which is calculated by multiplying the rotational speed of the wheel with the dynamic rolling radius, starts to decrease more rapidly than the actual velocity of the vehicle, indicating that the brake slip of the wheel is increasing. Once the deceleration, which is the derivative of v_R, exceeds the threshold $-a$ at the end of phase 1, the hydraulic modulator cuts the connection between the brake line and the master cylinder in order to maintain the brake pressure at a constant level. Brake pressure must not yet be reduced at this point, as the threshold might be reached within the stable zone of the friction coefficient versus brake slip curve. Simultaneously, the reference velocity v_{Ref}, which the control unit calculates, is reduced. As v_R continues to fall more rapidly than the reference velocity during phase 2, it eventually drops below the slip switching threshold λ_1, which is based on the reference velocity. At that point, the hydraulic modulator begins reducing the pressure in the brake line of the wheel by connecting the line to the return pump integrated in the modulator. [3]

The pressure reduction continues until the wheel acceleration is above $-a$ again. The modulator keeps the pressure at the same level throughout phase 4 until the wheel acceleration has reached the threshold value $+A$. After that, it starts to increase the pressure in phase 5 until the acceleration falls below $+A$ again. Once the acceleration has dropped beneath the threshold $+a$ at the end of phase 6, the modulator begins to gradually increase the pressure again, and eventually the cycle begins anew. However, in the following cycle, the pressure is reduced immediately after the deceleration exceeds the threshold $-a$. This is because in the previous cycle the deceleration of the wheel kept increasing even after the pressure increase was halted at the same deceleration threshold, and thus the control unit knows that the threshold is exceeded in the unstable zone of the friction coefficient curve. [3]

The value of the fixed wheel acceleration threshold $-a$ impacts the effectiveness of an anti-lock braking system. Its absolute value should be only fractionally higher than the maximum possible deceleration of the car. [3] However, the maximum deceleration depends significantly on the road conditions. The lower the friction coefficient between the tires and the road is, the lower the maximum deceleration is. Additionally, the inclination angle of the road impacts the deceleration capabilities due to the effect of gravity. Thus, having accurate information about the current tire-road friction coefficient and the inclination angle would allow the control unit to better estimate the maximum possible deceleration of the car, improving the accuracy of the wheel acceleration threshold. Furthermore, the reference velocity v_{Ref} could also be enhanced by limiting its gradient according to the maximum deceleration. This would impact the point at which the slip switching threshold λ_1 is crossed.

4.3.2 Traction Control System

The traction control system aims to prevent the driven wheels from spinning under acceleration and to keep their drive slip close to the slip that yields the highest longitudinal force. Excessive drive slip also significantly reduces the lateral force produced by a tire. Thus, TCS keeps the vehicle stable and steerable under acceleration in addition to increasing traction. [3]

The system can control the drive slip with the brake system of the car and by doing engine interventions to control the drive torque. TCS is most effective when it is designed to employ both of these mechanisms. The engine interventions can be done in gasoline-engine cars by

controlling the throttle valve, the ignition timing, or by phasing out individual fuel injection pulses. In diesel-engine vehicles, the drive torque can only be manipulated by reducing the quantity of fuel injected into the combustion chambers. By taking advantage of the ABS hydraulic system, TCS can do both symmetric and asymmetric brake applications. Asymmetric brake applications can be used to regulate the differential speed, the difference between the rotational speeds of the left and right side wheel, at the driven axle. This allows the system to control the drive torque distribution to the driven wheels, which can be particularly useful in preventing wheelspin in situations where the left and right side wheels are on surfaces with different coefficients of friction. Moreover, TCS can mimic the functionality of a central differential lock, which controls the drive torque distribution between the two axles, in four-wheel drive vehicles. [3]

In order to function as effectively as possible, TCS needs to calculate a reference value for the slip ratio at which the longitudinal force produced by the tire is at its highest. Various different factors can be taken into account in these calculations, one of which is the friction coefficient between the tires and the road. [3] Additionally, the friction coefficient could be taken advantage of in calculating the drive slip of each wheel in a four-wheel drive vehicle. In two-wheel drive vehicles, the drive slip of the driven wheels can be easily calculated by comparing the rotational speeds of the non-driven wheels to those of the driven wheels. In four-wheel drive vehicles, however, all four wheels can have significant drive slip simultaneously during acceleration, making it impossible to accurately calculate the drive slips purely based on the signals of the wheel speed sensors. A reference velocity, used to estimate the slip ratios, could be calculated based on the maximum possible acceleration of the vehicle, which is dictated by the friction coefficient.

4.3.3 Electronic Stability Program

ESP enhances the directional stability of the vehicle and also further improves the exploitation of traction potential during periods when ABS and TCS are active [3]. Its main task, however, is to limit the side slip angle of the car [4]. Its purpose is to keep the vehicle on the road and reduce the risk of overturning. ESP exploits the braking system as a tool for steering the vehicle by braking individual wheels in order to control the yaw moment. For instance, the outer front wheel can be braked during oversteer to reduce the side slip angle, and the inner rear wheel can be braked during understeer in order to increase the yaw rate. ESP can also affect the yaw moment by using the engine to accelerate the driven wheels. [3]

The control logic of the ESP is based on monitoring and controlling the side slip angle and the yaw rate of the vehicle. The side slip angle is estimated using an intricate observer, which usually functions as a model for an Extended Kalman Filter (EKF) [5]. Vehicle side slip angle estimation alone is not sufficient, however, as it can be unreliable. Therefore, the ESP controller also compares the nominal yaw rate $\dot{\psi}_{No}$ requested by the driver to the actual yaw rate. The nominal yaw rate is defined as [4]:

$$\dot{\psi}_{No} = \frac{u \cdot \delta}{l \cdot \left[1 + \left(\frac{u}{u_{char}}\right)^2\right]}. \tag{4.1}$$

As discussed in Chapter 3, the characteristic speed is derived from the linear single-track model, meaning that the nominal yaw rate is valid only for the linear region of the lateral force-slip angle curve of the tires [5]. The characteristic speed mainly depends on the lateral

stiffness of the tires. Therefore, the behavior of the ESP may vary based on the tires the car is fitted with, and it must be checked to perform correctly with all released tires. [4]

As shown in equation (4.2), the nominal yaw rate is limited by the current maximum friction coefficient between the tires and the road, as it limits the lateral acceleration of the car [3]. Because of this, friction estimation can be greatly beneficial to the performance of ESP systems.

$$|\dot{\psi}_{No}| \leq \left|\frac{\mu \cdot g}{u}\right| \tag{4.2}$$

The car is considered to be oversteering when [67]:

$$|\dot{\psi}| > |\dot{\psi}_{No}| \tag{4.3}$$

and understeering when [67]:

$$|\dot{\psi}| < |\dot{\psi}_{No}|. \tag{4.4}$$

The control logic can be designed in such a way that there is a dead zone around the nominal yaw rate. If the yaw rate of the vehicle is outside of this dead zone, the system will create a yaw moment in order to either increase the yaw rate if it is too low, or decrease it if it is too high. [4]

4.3.4 Adaptive Cruise Control

The adaptive cruise control system maintains the velocity of the vehicle at a constant level. If there is a car in front, it adapts the velocity such that a safe gap is maintained by using the engine management system and the brake system. The system aims to maintain the gap such that the time required for the most forward point of the car with ACC to reach the current position of the rearmost point of the vehicle in front stays the same. In other words, as velocity increases, so does the gap. The driver can interrupt the system at any time by pressing either the gas or the brake pedal. In order to measure the distance to the car in front, ACC employs a ranging sensor. The sensor function and controller logic are built into a single unit. While the main application areas of ACC are expressways and multilane trunk roads with light to relatively high traffic densities, systems capable of functioning in slow-moving traffic, with the capability to bring the car to a complete stop and then accelerate again, have been developed. ACC can also be integrated with an automatic emergency stop system, which can detect an impending crash and perform an emergency braking maneuver faster than the driver could. [3]

Braking distances depend on the current friction coefficient between the tires and the road. Friction estimation is thus beneficial to the performance of ACC systems, as knowledge of the current friction coefficient allows the system to adjust the safety gap to the car in front accordingly, improving the safety and the effectiveness of the system. Additionally, if the system is made capable of heavy acceleration and emergency braking maneuvers, friction estimation will be of additional help due to the previously described beneficial effects it has on TCS and ABS. [3]

5 Research Vehicle and Sensor Equipment

In order to conduct experimental tests with the developed friction estimation algorithm, a test car was fitted with appropriate sensor equipment. This car was also modelled in the simulation software.

5.1 Research Vehicle

The vehicle that was used in the road tests is a 1.9-liter TDI version of a fifth generation Volkswagen Golf Variant. The car is equipped with TCS, ABS, and ESP. The wheel-integrated force transducer, attached to the right front wheel, and the optical velocity sensor, attached to the right front corner of the car, have been marked in figure 19 with a red and a blue circle.

Figure 19 Research vehicle

Most of the relevant parameters of the car were already known, as the car had been used in various previous projects. Those parameters are presented in table 2, which contains information from references [68; 69; 70; 71]. The torque versus revolutions-per-minute (RPM) and drag torque versus RPM curves (figure 20) were also available from a previous project. The curves had been obtained by scaling the curves of a smaller version of the same engine. Drag torque is the torque produced by the engine when no throttle pedal is applied. [69]

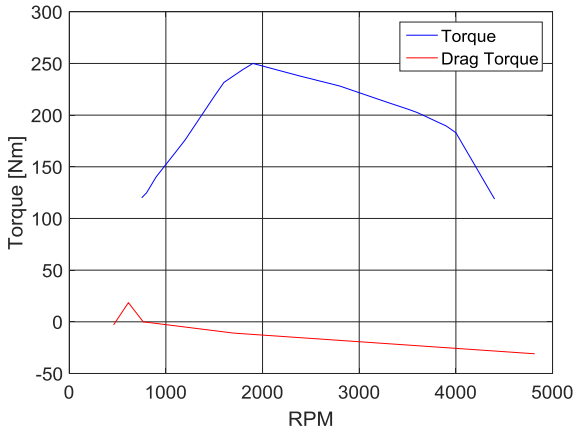

Figure 20 Torque and drag torque maps of the research vehicle

Table 2 Research vehicle parameters

Dimensions	Wheelbase	$2.578\ m$
	Track width front	$1.535\ m$
	Track width rear	$1.508\ m$
	Vehicle length	$4.556\ m$
	Rear overhang	$1.0329\ m$
	Height of center of mass	$0.58\ m$
Springs & stabilizers	Front spring stiffness	$24.5\ N/mm$
	Rear spring stiffness	$27.45\ N/mm$
	Front stabilizer stiffness	$33.3\ N/mm$
	Rear stabilizer stiffness	$29.2\ N/mm$
Dampers	Front damping (pull)	$810\ Ns/m$
	Front damping (push)	$1000\ Ns/m$
	Rear damping (pull)	$1300\ Ns/m$
	Rear damping (push)	$540\ Ns/m$
Suspension kinematics	Steering ratio	14.96
	Front suspension layout	Independent, McPherson
	Rear suspension layout	Multi-link
Aerodynamics	Frontal reference area	$2.11\ m^2$
Gear ratios	1st gear	3.78: 1
	2nd gear	2.06: 1
	3rd gear	1.35: 1
	4th gear	0.97: 1
	5th gear	0.74: 1
	Reverse gear	3.60: 1
	Front differential	3.78: 1
Tires	Dimensions	205/55 R16

Additionally, the wheel loads were measured with four scales that were situated underneath each tire. Based on these measurements, the overall weight, the longitudinal and lateral weight distributions, and the cross weight of the vehicle could be calculated. In order for the measurements to reflect the state of the vehicle during the test maneuvers, they were conducted with some fuel in the tank and with two people sitting in the front seats. The measurements and the values calculated based on them are presented in table 3.

The research vehicle was fitted with the non-studded winter tires Nokian Hakkapeliitta R, 205/55 R16 94R XL. The tire, which is shown in figure 21, features a complex tread pattern with various kinds of sipes in order to disperse water effectively and to provide optimum grip [72].

Table 3 Research vehicle weight measurements

Left front load	$453.0\ kg$
Right front load	$481.5\ kg$
Left rear load	$343.0\ kg$
Right rear load	$355.5\ kg$
Overall weight	$1633.0\ kg$
Longitudinal weight distribution	$57.23\ \%$ (front); $42.77\ \%$ (rear)
Distance of CoG from front axle	$1.1026\ m$
Distance of CoG from rear axle	$1.4753\ m$
Lateral weight distribution	$48.74\ \%$ (left); $51.26\ \%$ (right)
Cross weight	$50.49\ \%$ (right front + left rear)

Figure 21 Nokian Hakkapeliitta R non-studded winter tire [72]

5.2 Sensor Equipment

The research vehicle features various sensors that have been installed by the manufacturer. They serve as part of the information, control, and safety systems of the car. Of those sensors, the steering angle sensor, the brake pressure sensor, the gas pedal position sensor, and the wheel speed sensors are needed for the friction estimation algorithm. The outputs of these sensors are read from the CAN bus of the car. The wheel speed sensor values that can be obtained from the bus are the rotational speeds of the wheels multiplied by a constant value that is an approximation of the dynamic rolling radius. Additionally, the state (on/off) of the anti-lock braking and traction control systems can be read from the CAN bus. Knowledge of their states is needed for the algorithm.

The vehicle was equipped with three additional sensors: an inertial measurement unit, a wheel-integrated force transducer, and an optical velocity sensor. The IMU measures accelerations in all three directions and rotational speeds around all three axes [73]. Its purpose is to serve as the core component of the friction estimation algorithm. The wheel-integrated force transducer measures all of the tire-road forces and moments that were displayed in figure 9 [74]. Thus, it allows for accurate measurement of the tire-road friction, which can then be used for comparison with the friction estimation algorithm. The optical velocity sensor measures both the longitudinal and the lateral velocity of the vehicle [75].

5.2.1 Wheel-Integrated Force Transducer

In order to have a comparison point in the road tests for the friction potential calculated by the algorithm, the research vehicle was equipped with a wheel-integrated force transducer system. The transducer used was the Spinning Wheel Integrated Force Transducer (SWIFT) 20 manufactured by MTS. The system (figure 22) consists of multiple components. The transducer is mounted on a modified rim using an adapter, and a slip ring encoder is attached to it. The transducer has four beams with strain gauge bridges that measure the forces and moments of the tire. The encoder measures the angular position of the transducer, which is used to convert raw force and moment data from the rotating transducer to a vehicle-based coordinate system. Data is transmitted from the wheel via the slip ring. A calibration procedure must be executed before doing measurements so that the system knows the angular position of the wheel accurately. [74] The lateral, longitudinal, and overall tire-road friction coefficients can be calculated from the measured forces using equations (3.10), (3.11), and (3.13). The weight of the wheel causes an offset in the vertical load measurement. This offset was measured by lifting the right front corner of the car so that only the weight of the wheel would show in the vertical load measurement. The offset was -225 N, meaning that the weight of the wheel assembly is approximately 23 kg. The masses of the other three identical wheels were measured to be 20 kg each.

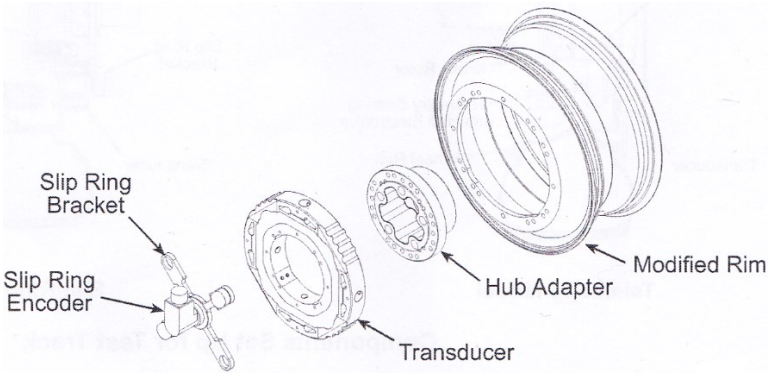

Figure 22 Transducer assembly [74]

5.2.2 Optical Velocity Sensor

The CORREVIT S-350 non-contact 2-axis optical sensor was used to obtain precise measurements of the lateral and the longitudinal velocity of the center of gravity. The sensor uses a high-intensity light source to illuminate the surface, and the optical component of the sensor is able to observe the stochastic microstructure of the surface via an objective lens. On top of the velocities, the sensor can also measure distance and angle. The sensor can measure velocities between 0.5 kph and 250 kph. The purpose of the sensor in this research was obtaining the longitudinal velocity and the side slip angle of the CoG of the vehicle to help with analyzing the measurement results. [68; 75]

As shown in figure 19, the optical sensor was attached to the right front corner of the car. The yaw rate of the vehicle causes the measured velocities to differ from those of the CoG due to the distances a and b that are demonstrated in figure 23.

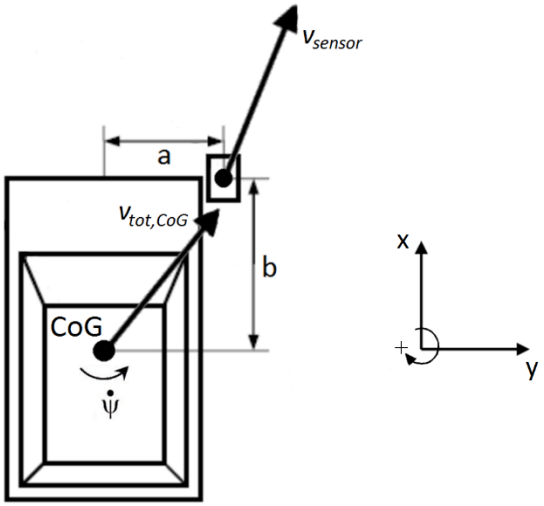

Figure 23 Optical velocity sensor and vehicle motion (figure is based on [68])

In order to transform the measured longitudinal and lateral velocities to the CoG, the following equations must be used [68]:

$$u = v_{x,sensor} + \dot{\psi} \cdot a, \tag{5.1}$$

$$v = v_{y,sensor} - \dot{\psi} \cdot b. \tag{5.2}$$

The distances a and b were measured to be 0.47 m and 2.05 m respectively.

5.2.3 Inertial Measurement Unit

The IMU chosen for this thesis was ADIS16362 by Analog Devices, which includes a triaxis gyroscope and a triaxis accelerometer. It can measure rotational speeds between -300 and +300 degrees per second and accelerations between -1.7 and +1.7 g. [73]

The sensor was placed in the middle of the footwell area of the rear seats. Thus, it was close to the centerline of the vehicle, meaning that its lateral distance from the center of gravity was small. It was also vertically close to the same level as the CoG. However, longitudinally it was situated significantly behind the CoG. Consequently, the measured lateral acceleration is not equal to that of the center of gravity. The measured lateral acceleration consists of the time derivative of the lateral velocity at the location of the sensor and the centripetal acceleration of the vehicle. Thus, the measured lateral acceleration can be formulated similarly to equation (3.4):

$$a_{y,m} = \dot{v}_{y,is} + u\dot{\psi} \tag{5.3}$$

where $\dot{v}_{y,is}$ is the time derivative of the lateral velocity of the vehicle at the location of the inertial measurement unit. The value of the centripetal acceleration is the same at the location of the sensor as it is for the center of gravity because yaw rate is equal for every point of the vehicle and the sensor is considered to have no lateral distance to the CoG, meaning that the longitudinal velocity at its location is equal to that at the CoG. However, the lateral velocity and its time derivative are not the same as at the CoG. The lateral velocity can be transformed to the CoG by exploiting equation (5.2). Combining equations (3.4) and (5.2) yields:

$$a_y = \frac{d}{dt}\left(v_{y,is} - \dot{\psi} \cdot b_{is}\right) + u\dot{\psi} = \dot{v}_{y,is} + u\dot{\psi} - \ddot{\psi} \cdot b_{is} \tag{5.4}$$

where b_{is} is the longitudinal distance between the center of gravity and the inertial measurement unit, which was measured to be approximately 0.62 m. Since the sensor is located behind the CoG, b_{is} must be defined as -0.62 m. Equations (5.3) and (5.4) can now be combined to obtain the equation that can be used to transform the measured lateral acceleration to the CoG:

$$a_y = a_{y,m} - \ddot{\psi} \cdot b_{is}. \tag{5.5}$$

Furthermore, the acceleration measurements of the IMU are affected by gravity. Unless the orientation of the sensor unit is perfectly level such that its z-axis is pointing directly towards the center of the Earth, a component of gravitational acceleration will show up on one of the other two axes or on both of them, depending on the orientation. For example, if the road features inclination, the measured acceleration along the x-axis will then be:

$$a_{x,m} = a_x + g \cdot \sin(\theta) \tag{5.6}$$

where a_x is the actual acceleration of the sensor along its x-axis, which is equal to that of the vehicle, and θ is the pitch angle. If the road features both inclination and bank angle, the measured lateral acceleration then becomes:

$$a_{y,m} = a_y + \ddot{\psi} \cdot b_{is} + g\cos(\theta)\sin(\varphi) \tag{5.7}$$

where φ is the bank angle. This property of the sensor can be exploited to measure the inclination and the bank angle of the road by comparing the sensor outputs to acceleration measurements obtained from other sources. [65; 76]

In reality, the body of the car pitches and rolls during cornering and acceleration due to the suspension, which means that the orientation of the IMU differs from that of the vehicle. However, these effects are neglected in the estimation algorithm, and it is assumed that the gravitational components affecting the longitudinal and lateral acceleration measurements are only caused by the angles of the road itself. This assumption will contribute to error in the friction estimation due to its effect on acceleration and wheel load estimations.

Moreover, the vertical acceleration measurements were neglected in the estimation algorithm because they were seen to contain significant amounts of noise and little useful information. Not using the vertical acceleration measured by the IMU will contribute to error in the wheel load calculations of the algorithm in situations where the vertical acceleration is non-zero.

The orientation of the sensor unit relative to the vehicle was measured to be such that when the vehicle was parked on a level ground, the x-axis of the sensor was pointing slightly downward with an angle of approximately 1.5 degrees. The compensation of this angle, and the exploitation of the sensor measurements to obtain the road inclination and bank angle are explained in detail in Chapter 7.

6 Simulation Model

The friction estimation algorithm was tested in simulations as well. The IPG CarMaker virtual test driving software was chosen for this purpose. The software can also be integrated with the Simulink block diagram environment, which is convenient for testing the algorithm, as it was created in the environment.

The research vehicle was modelled in CarMaker. While most of the significant parameters of the vehicle were known, for some the default values given by CarMaker were used. The tires were modelled using Pacejka's Magic Formula tire model. The parameters were estimated for the tire model such that the force versus slip curves had the shape a typical non-studded winter tire would have on a snowy surface. An inertial measurement unit was placed in the simulated vehicle. Electronic driver aids were also modelled. ABS and TCS algorithms were readily available for the software and required little modifications, but an ESP system had to be created. A simplified, bare-bones version of ESP was modelled.

6.1 Simulation Software

6.1.1 IPG CarMaker

The IPG CarMaker virtual test driving software allows for a wide variety of applications. On top of enabling testing the dynamic behavior of vehicles, chassis control, driver assistance systems, and system networks can be developed with it as well. The software can also be used in hardware-in-the-loop (HIL) simulations. [77]

The CarMaker software consists of two parts: the Virtual Vehicle Environment (VVE) and the CarMaker Interface Toolbox (CIT). The VVE simulates the vehicle, driver, road, and environment. The CIT, which consists of five main modules, allows complete control of the VVE. [78] The graphical user interface (GUI) module (figure 24) is used to access the various vehicle, road, driver, and maneuver parameters. The road, driver, and maneuver parameters are looked at more closely in Chapter 8. The other modules are also accessed from the GUI.

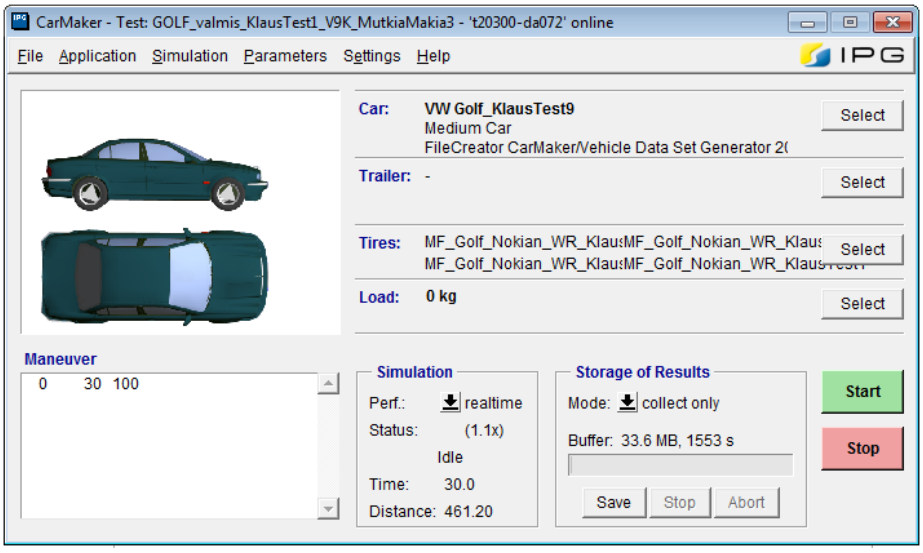

Figure 24 CarMaker GUI

The IPGMovie module (figure 25, left) is a 3D-animation tool that allows for viewing the maneuvers of the virtual car during or after the simulation. The module displays the tire-road forces and wheel loads as bars during the animation. The Instruments module (figure 25, right) displays the most important instruments, dials, and information about the vehicle's driving condition, including steering wheel angle, selected gear, ignition, speedometer, tachometer, and ESP and ABS warning lamps. [78]

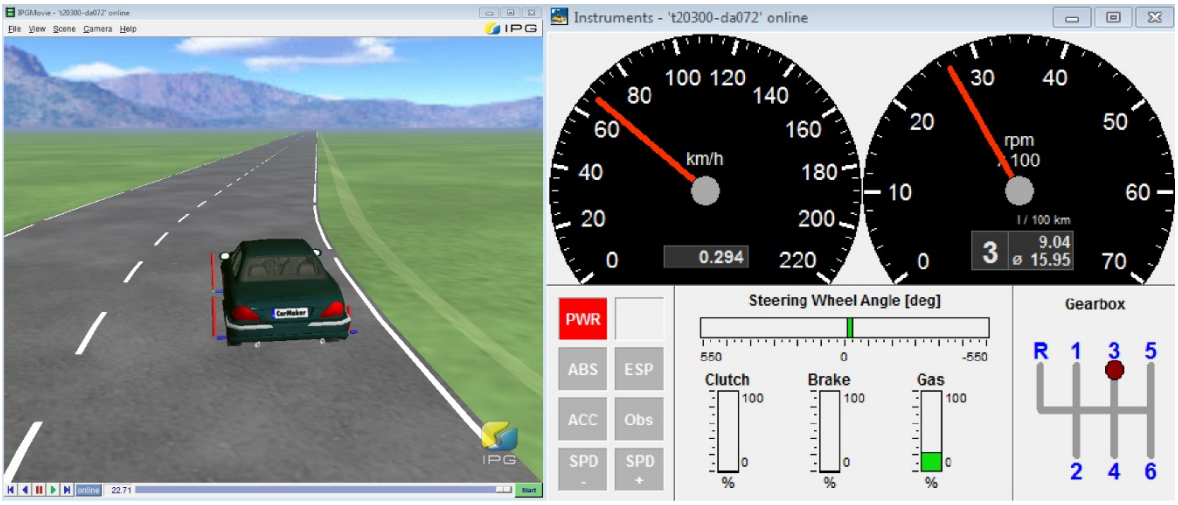

Figure 25 IPGMovie and Instruments modules

The IPGControl module (figure 26) serves as a visualization and data analysis tool. It is used to view the desired output quantities either in real-time during the simulation or afterwards [78].

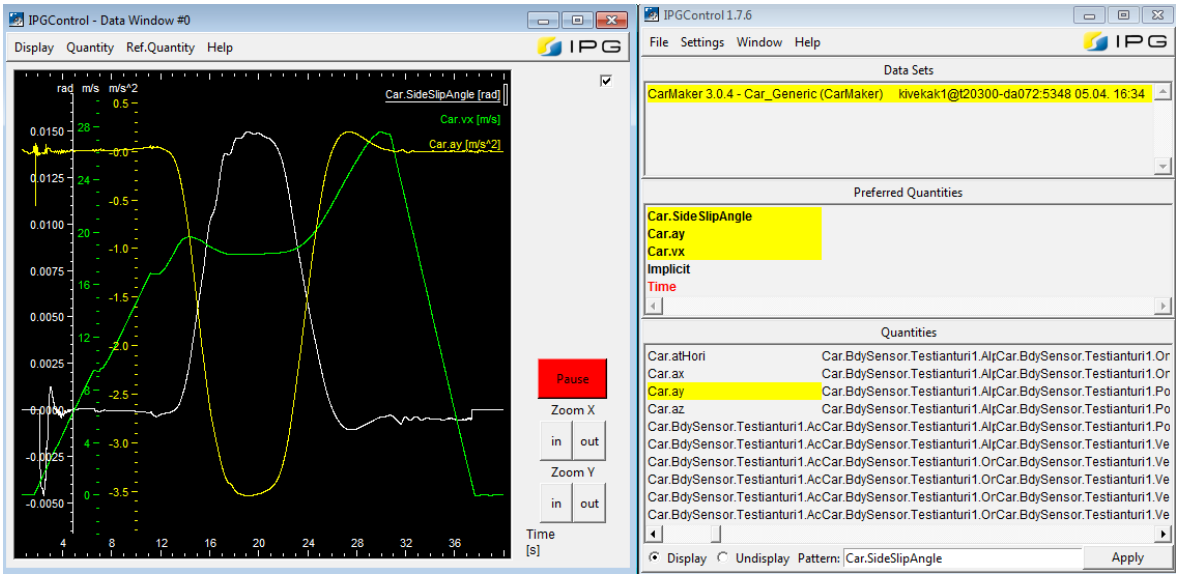

Figure 26 IPGControl

The last main module is IPGKinematics, which is designed to simulate a vehicle axle on an axle kinematics test bench. It is used to calculate the kinematics, steering kinematics, and elastokinematics of all types of suspension [79].

CarMaker uses a coordinate system that differs from the one presented at the start of Chapter 3. The positive y-axis points to the left rather than right, and the positive z-axis direction is upwards, meaning that the positive directions of yaw and pitch are reversed as well. [77] The CarMaker coordinate system will be used in this thesis from this point onwards.

6.1.2 MATLAB and Simulink

MATLAB is a versatile numerical computing environment and a proprietary high-level programming language developed by MathWorks. It can be used to analyze data, develop algorithms, and create models. It features add-on toolboxes for a wide range of engineering and scientific applications while also allowing the users to create their own custom apps and toolboxes. [80] Simulink is a block diagram environment for multidomain simulation and model-based design. It is integrated with MATLAB, meaning that MATLAB algorithms can be incorporated into Simulink models and simulation results can be exported to MATLAB for further analysis. [81]

CarMaker for Simulink is a complete integration of the CarMaker software into the MATLAB and Simulink modelling and simulation environment. It features a special CarMaker interface block set for Simulink, which allows for all of the internal variables of CarMaker to be read from and written to in Simulink. This also enables the user to create custom variables that can then be be monitored in the IPGControl module. The integration has been executed using S-functions and MATLAB and Simulink API functions. The functionality of CarMaker is not reduced in any way, and it can be operated from its GUI as usual. The vehicle model has been segmented into subsystems in Simulink for easy customization. The purpose of the integration is to enable Simulink models to be incorporated into CarMaker vehicle models, allowing custom controller models and other relevant algorithms to be designed and tested. [11; 82]

6.2 Simulated Vehicle

CarMaker simulates the vehicle body as a multibody system that features the main body and four wheel carriers, which are connected to each other with joints. The vehicle body module interacts with other modules from the vehicle library, as shown in figure 27. [77] The trailer module is disregarded in this thesis.

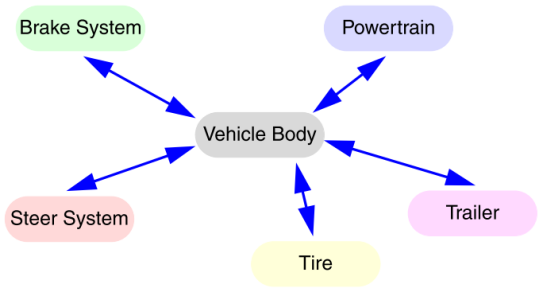

Figure 27 CarMaker vehicle model modules [77]

6.2.1 Vehicle Parameters

The vehicle editor contains 9 different tabs for the main body, masses, suspensions, steering, tires, brake, powertrain, aerodynamics, sensors, and vehicle animation graphics. The modelling of a car begins by using a vehicle data generator tool, which requests the basic

dimensions, mass, and type of the car. The software then calculates default values for all the rest of the parameters of the vehicle based on the values given by the user.

6.2.1.1 Main Body and Masses

The properties of the main body, including its mass, inertias, and location of the center of mass, are given on the "Main Body" tab (figure 28). The user can also choose whether the body should be rigid or flexible on that tab. The main body does not include the wheel carriers or wheels. Their values are given on the "Masses" tab (figure 29) along with the values of additional trim loads. The locations of all the bodies are given relative to a coordinate system that has its origin on the centerline at the rearmost point of the car, on ground level. Two trim loads were added to the car to simulate the driver and the passenger. The masses and locations of the bodies were chosen such that the vertical wheel loads are close to those presented in table 3 while keeping the known masses at the measured values. In particular, the masses of the front wheel carriers were manipulated to obtain the right wheel loads. The masses of the driver and the passenger were known in addition to the masses of the wheels and the overall vehicle, driver, passenger, and fuel combination. All the inertias were left to the default values given by CarMaker.

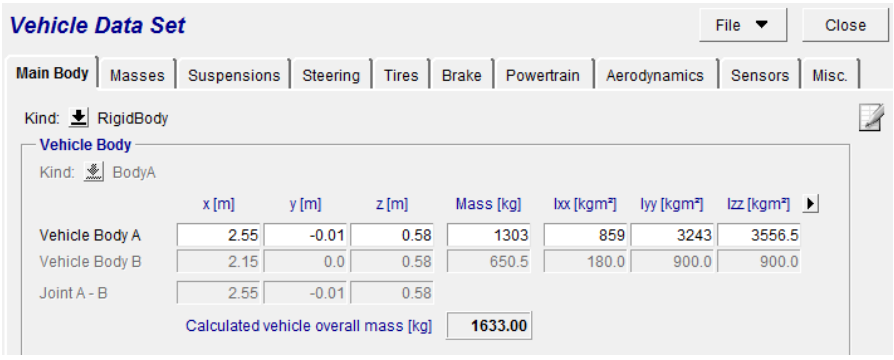

Figure 28 "Main Body" tab with chosen values

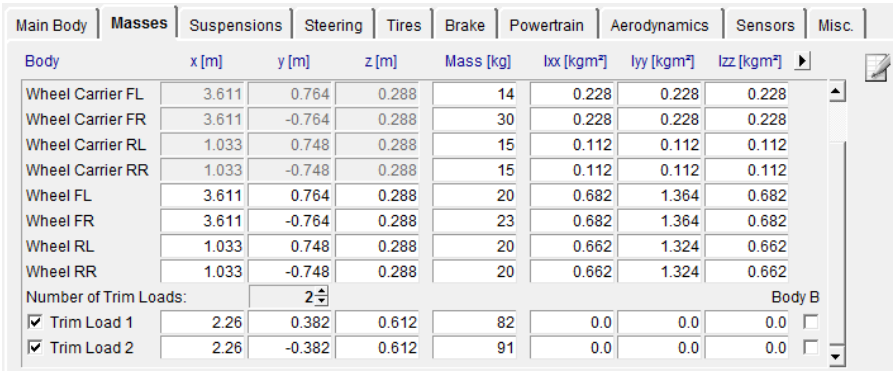

Figure 29 "Masses" tab with chosen values

6.2.1.2 Suspensions

On the "Suspensions" tab, the user can define the spring, buffer, and stabilizer stiffnesses in addition to the damper coefficients, as well as the kinematics, compliance, and wheel bearing friction of the front and rear suspensions. Furthermore, external forces acting on the suspensions can be defined in this tab. The spring and stabilizer stiffnesses, as well as the

damping coefficients from table 2 were given as inputs here. It is also possible to define curves for the spring stiffnesses and damping coefficients rather than defining them as being constant. The buffers, which are used to limit suspension travel, were left at the default values, as there was no measurement data available for them. The buffers are defined separately for the front and rear suspensions, as well as for suspension compression (push) and extension (pull). The default buffer curves are presented in figure 30. The amount of wheel travel required to engage the buffer is denoted by $tz0$ in the figure. [78]

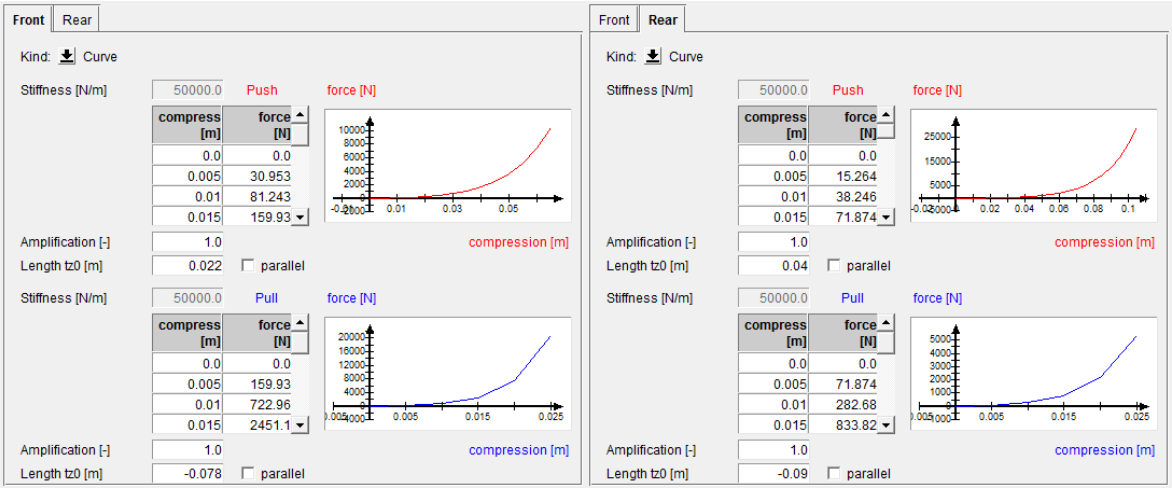

Figure 30 Buffer parametrization

Suspension kinematics describes the position and orientation of a wheel, and their variations according to wheel travel, steering rack displacement, and movement of the opposite wheel [78]. The suspension kinematics of the research vehicle had been measured and modelled in CarMaker as part of a previous project [83]. However, it was found that the modelled kinematics were unstable in many driving situations, and thus the default kinematics models were used instead. The "Linear3D" kinematics model was used for the front suspension. In that model, the kinematics depend linearly on the wheel travel, the steering rack displacement, and the movement of the opposite wheel. The "Linear2D" model was used for the rear suspension. It is similar to the model used for the front suspension, but it omits the effects of steering rack displacement. [78]

The default values given by CarMaker were used for all the parameters of both of the suspension kinematics models. They are presented in figure 31. The explanations and units for the parameters are given in figure 32. The "Static" column in figure 31 describes the values of the parameters when the wheel travel is null. The values in the "Compress" column give the variation of the parameters per meter of wheel travel, while the "Steering" and "Opposites" columns describe the variation of the parameters per meter of steering rack displacement and per meter of wheel travel of the opposite wheel. [78]

Suspension compliance refers to the position and orientation of the wheel changing when forces are applied. No information was available about the compliances of the research vehicle, so they were left undefined. Wheel bearing frictions were also left blank, as they had not been measured.

Front | Rear

Kind: Linear3D

	Static	Compr.	Oppos.	Steer
Translation tx	0	0	0.0	0
Translation ty	0	0	0.0	0
Translation tz	0	1.0	0.0	0.1
Rotation rx	0.01	0	0.0	0
Rotation ry	0	0	0.0	0
Rotation rz	0.003	0	0.0	5
Deflection lSpring	0.0	-1.0	0.0	0.0
Deflection lDamp	0.0	-1.0	0.0	0.0
Deflection lBuf	0.0	-1.0	0.0	0.0
Deflection lStabi	0.0	1.0	0.0	0.0

Front | Rear

Kind: Linear2D

	Static	Compr.	Oppos.
Translation tx	0	0	0
Translation ty	0	0	0
Translation tz	0	1	0
Rotation rx	0.01	0	0
Rotation ry	0	0	0
Rotation rz	0.002	-0.035	0
Deflection lSpring	0.0	-1.0	0.0
Deflection lDamp	0.0	-1.0	0.0
Deflection lBuf	0.0	-1.0	0.0
Deflection lStabi	0.0	1.0	0.0

Figure 31 Kinematics parameter values

Parameter	Description	Unit (Compress)	Unit (Steering or Opposite)
tx	wheel base variation (contribution of one axle)	$m/m_{wheel\ travel}$	$m/m_{steering\ rack\ dist}$ or $m/m_{opposite\ wheel\ travel}$
ty	track variation	$m/m_{wheel\ travel}$	$m/m_{steering\ rack\ dist}$ or $m/m_{opposite\ wheel\ travel}$
tz	wheel travel variation	$m/m_{wheel\ travel}$	$m/m_{steering\ rack\ dist}$ or $m/m_{opposite\ wheel\ travel}$
rx	camber variations	$rad/m_{wheel\ travel}$	$rad/m_{steering\ rack\ dist}$ or $rad/m_{opposite\ wheel\ travel}$
ry	caster variations	$rad/m_{wheel\ travel}$	$rad/m_{steering\ rack\ dist}$ or $rad/m_{opposite\ wheel\ travel}$
rz	toe variations	$rad/m_{wheel\ travel}$	$rad/m_{steering\ rack\ dist}$ or $rad/m_{opposite\ wheel\ travel}$
lSpring	Spring length variation	$m/m_{wheel\ travel}$	$m/m_{steering\ rack\ dist}$ or $m/m_{opposite\ wheel\ travel}$
lDamp	Damper length variation	$m/m_{wheel\ travel}$	$m/m_{steering\ rack\ dist}$ or $m/m_{opposite\ wheel\ travel}$
lBuff	Buffer length variation when activated	$m/m_{wheel\ travel}$	$m/m_{steering\ rack\ dist}$ or $m/m_{opposite\ wheel\ travel}$
lStabi	Stabilizer length (showing the vertical movement of the ARB at the point where the stiffness was measured) or angle variation, according to which unit you used for the ARB stiffness.	$m/m_{wheel\ travel}$ or $rad/m_{wheel\ travel}$	$m/m_{steering\ rack\ dist}$ or $m/m_{opposite\ wheel\ travel}$ or $rad/m_{steering\ rack\ dist}$ or $rad/m_{opposite\ wheel\ travel}$

Figure 32 Kinematics parameters

6.2.1.3 Steering System

As shown in table 2, the steering ratio of the research vehicle is 14.96. This value refers to the ratio between the angle of the steering wheel and the angle of the front wheels. However, in CarMaker, the steering gear ratio is input as the relationship between the angle of the steering wheel and the displacement of the steering rack. The displacement causes the front wheels to turn according to the front suspension kinematics. The steering-wheel-to-rack ratio required by CarMaker can be calculated as:

$$\tau_{swtr} = r_z \cdot \tau \tag{6.1}$$

where τ is the measured steering ratio, and r_z is the ratio between the angle of the front wheels and the displacement of the steering rack, which was defined as 5 rad/m in figure 31. The equation yields the value 74.8 rad/m.

6.2.1.4 Brake System

CarMaker features a comprehensive brake system model that incorporates a master cylinder, booster, pump, low pressure accumulator, valves, and pressure loss in the circuits. The system can be configured as having either diagonal circuits or one circuit per axle. In the diagonal system, which is the default configuration, each brake circuit operates one front wheel brake and the rear wheel brake on the opposite side. [77] No information was available about the brake system in the research vehicle. Thus, the default values provided by CarMaker were used.

6.2.1.5 Powertrain

The engine, clutch, gearbox, and differentials are configured in the "Powertrain" tab of CarMaker's vehicle editor. The type of the powertrain is also defined in this tab; it can be configured either as internal combustion engine based or as a hybrid system. The driven wheels are defined here as well.

As discussed in section 5.1, the engine torque maps were available from a previous project (reference [69]). The engine provides a maximum torque of 250 Nm at 1900 RPM and a maximum power of 77 kW at 4000 RPM. The fuel consumption map of the engine had also been modelled in CarMaker in the same project, though the map is not relevant to this thesis. The gear ratios are also defined in this tab, as well as the inertias of the engine, clutch, gearbox, and differential. The gear ratios shown in table 2 were given as inputs. The inertias were not known, so they were left at the default values. The front differential was modelled as featuring no locking system, since the properties of the differential in the research vehicle were unknown. An unlocked (open) differential allows the wheels to rotate at different speeds but always provides the same amount of torque to both of them [23].

6.2.1.6 Aerodynamics

CarMaker incorporates wind loads as 3 forces (drag, side force, and lift) and 3 torques (rolling, yawing, and pitching moment) on the vehicle body. All of them are dependent on the side slip angle, velocity, and frontal reference area of the car, as well as the density of the air. The only aerodynamics-related measurement that had been conducted with the car was the measurement of the frontal reference area, which had been determined to be 2.11 m^2 [69]. All of the coefficients of the forces and moments were left at the default values. The default drag coefficient at zero side slip angle given by CarMaker is 0.31.

6.2.2 Tire Model

Tires can be modelled in CarMaker with either Pacejka's Magic Formula (MF) version 5.2 or IPG's own IPGTire model. The Simulink integration also enables the user to create their own tire model. [77] The MF model was chosen for this thesis. The goal was to set the parameters of the model such that it could simulate the characteristics of a tire in both snowy and icy conditions. A maximum friction coefficient of 0.35 was chosen for snow and 0.15 for ice. The starting point of the modelling process was using the default parameters given by Pacejka in [24]. The parameters were then modified such that the curves would have roughly the same characteristics as those presented in figure 15, meaning that the curves on

snow would have a fairly flat peak that would get even flatter with higher wheel loads and the curves for icy road conditions would reach their peaks with less slip and the peaks would be sharper.

In the Magic Formula, the forces for pure lateral and longitudinal slips read [24; 77]:

$$F_{y0} = D_y \sin\left[C_y \tan^{-1}\left\{B_y\alpha_y - E_y\left(B_y\alpha_y - \tan^{-1}\left(B_y\alpha_y\right)\right)\right\}\right] + S_{Vy}, \tag{6.2}$$

$$F_{x0} = D_x \sin[C_x \tan^{-1}\{B_x\kappa_x - E_x(B_x\kappa_x - \tan^{-1}(B_x\kappa_x))\}] + S_{Vx} \tag{6.3}$$

where the new definition of slip angle is:

$$\alpha_y = \alpha + S_{Hy} \tag{6.4}$$

and the new definition of slip ratio is:

$$\kappa_x = \kappa + S_{Hx}. \tag{6.5}$$

The coefficients B_i, C_i, D_i, E_i, S_{Vi}, and S_{Hi} are calculated with auxiliary parameters. The shape coefficient C_i describes how much the curve declines after the peak. D_i, on the other hand, dictates the height of the peak. The coefficients B_i, C_i, and D_i together define the slope of the linear portion of the curve. The offsets due to plysteer, camber, caster, and conicity are incorporated in the shift terms S_{Vi} and S_{Hi}. [24] The coefficients and shift terms are calculated with their own equations that contain all the tunable p, r, and λ parameters. For the lateral force, the equations are:

$$C_y = p_{Cy1} \cdot \lambda_{Cy}, \tag{6.6}$$

$$D_y = \mu_y \cdot F_z, \tag{6.7}$$

$$\mu_y = \left(p_{Dy1} + p_{Dy2}df_z\right) \cdot \left(1 - p_{Dy3}{\gamma_y}^2\right) \cdot \lambda_{\mu y}, \tag{6.8}$$

$$\gamma_y = \gamma \cdot \lambda_{\gamma y}, \tag{6.9}$$

$$E_y = \left(p_{Ey1} + p_{Ey2}df_z\right) \cdot \left\{1 - \left(p_{Ey3} + p_{Ey4}\gamma_y\right)\mathrm{sgn}\left(\alpha_y\right)\right\} \cdot \lambda_{Ey}, \tag{6.10}$$

$$K_{y\alpha} = p_{Ky1}F_{z0} \sin\left(2 \tan^{-1}\left\{\frac{F_z}{p_{Ky2}F_{z0}}\right\}\right) \cdot \left(1 - p_{Ky3}|\gamma|\right) \cdot \lambda_{Ky\alpha}, \tag{6.11}$$

$$B_y = \frac{K_{y\alpha}}{\left(C_yD_y + \varepsilon_y\right)}, \tag{6.12}$$

$$S_{Vy} = F_z\left\{\left(p_{Vy1} + p_{Vy2}df_z\right) \cdot \lambda_{Vy} + \left(p_{Vy3} + p_{Vy4}df_z\right)\gamma_y \cdot \lambda_{\gamma y}\right\} \cdot \lambda_{\mu y}, \tag{6.13}$$

$$S_{Hy} = \left(p_{Hy1} + p_{Hy2}df_z\right) \cdot \lambda_{Hy} + p_{Hy3}\gamma_y \tag{6.14}$$

where F_z stands for the wheel load and F_{z0} is the nominal wheel load. [24; 77] Furthermore, df_z stands for the normalized change in vertical load, which is defined by the following equation [24; 77]:

$$df_z = \frac{F_z - F_{z0}}{F_{z0}}. \tag{6.15}$$

The nominal wheel load was set to 4000 N, as that is close to the average load carried by each wheel of the research vehicle when the vehicle is static.

For the longitudinal force, the coefficient equations read [24; 77]:

$$C_x = p_{Cx1} \cdot \lambda_{Cx}, \tag{6.16}$$

$$D_x = \mu_x \cdot F_z, \tag{6.17}$$

$$\mu_x = (p_{Dx1} + p_{Dx2} df_z) \cdot (1 - p_{Dx3} {\gamma_x}^2) \cdot \lambda_{\mu x}, \tag{6.18}$$

$$\gamma_x = \gamma \cdot \lambda_{\gamma x}, \tag{6.19}$$

$$E_x = \left(p_{Ex1} + p_{Ex2} df_z + p_{Ex3} {df_z}^2\right) \cdot \{1 - p_{Ex4} \mathrm{sgn}(\kappa_x)\} \cdot \lambda_{Ex}, \tag{6.20}$$

$$K_{x\kappa} = F_z \cdot (p_{Kx1} + p_{Kx2} df_z) \cdot \exp(p_{Kx3} df_z) \cdot \lambda_{Kx\kappa}, \tag{6.21}$$

$$B_x = \frac{K_{x\kappa}}{(C_x D_x + \varepsilon_x)}, \tag{6.22}$$

$$S_{Vx} = F_z \cdot (p_{Vx1} + p_{Vx2} df_z) \cdot \lambda_{Vx} \cdot \lambda_{\mu x}, \tag{6.23}$$

$$S_{Hx} = (p_{Hx1} + p_{Hx2} df_z) \cdot \lambda_{Hx}. \tag{6.24}$$

In combined slip situations, when the tire is experiencing both longitudinal and lateral slip simultaneously, the following equations define the forces [24; 77]:

$$F_y = G_{y\kappa} \cdot F_{y0} + S_{Vy\kappa}, \tag{6.25}$$

$$F_x = G_{x\alpha} \cdot F_{x0} \tag{6.26}$$

where the coefficient equations for the lateral force are:

$$G_{y\kappa} = \frac{\cos\left[C_{y\kappa} \tan^{-1}\left\{B_{y\kappa}\kappa_s - E_{y\kappa}\left(B_{y\kappa}\kappa_s - \tan^{-1}\left(B_{y\kappa}\kappa_s\right)\right)\right\}\right]}{G_{y\kappa 0}}, \tag{6.27}$$

$$G_{y\kappa 0} = \cos\left[C_{y\kappa} \tan^{-1}\left\{B_{y\kappa}S_{Hy\kappa} - E_{y\kappa}\left(B_{y\kappa}S_{Hy\kappa} - \tan^{-1}\left(B_{y\kappa}S_{Hy\kappa}\right)\right)\right\}\right], \tag{6.28}$$

$$\kappa_s = \kappa + S_{Hy\kappa}, \tag{6.29}$$

$$S_{Hy\kappa} = r_{Hy1} + r_{Hy2} df_z, \tag{6.30}$$

$$B_{y\kappa} = r_{By1} \cos\left[\tan^{-1}\{r_{By2}(\alpha - r_{By3})\}\right] \cdot \lambda_{y\kappa}, \tag{6.31}$$

$$C_{y\kappa} = r_{Cy1}, \tag{6.32}$$

$$E_{y\kappa} = r_{Ey1} + r_{Ey2} df_z, \tag{6.33}$$

$$S_{Vy\kappa} = D_{Vy\kappa} \sin\left[r_{Vy5} \tan^{-1}(r_{Vy6}\kappa)\right] \cdot \lambda_{Vy\kappa}, \tag{6.34}$$

$$D_{Vy\kappa} = \mu_y F_z \cdot \left(r_{Vy1} + r_{Vy2} df_z + r_{Vy3}\gamma_z\right) \cdot \cos\left(\tan^{-1}(r_{Vy4}\alpha)\right), \tag{6.35}$$

$$\gamma_z = \gamma \cdot \lambda_{\gamma z}. \tag{6.36}$$

The coefficient equations for the longitudinal force are [24; 77]:

$$G_{x\alpha} = \frac{\cos[C_{x\alpha} \tan^{-1}\{B_{x\alpha}\alpha_s - E_{x\alpha}(B_{x\alpha}\alpha_s - \tan^{-1}(B_{x\alpha}\alpha_s))\}]}{G_{x\alpha 0}}, \tag{6.37}$$

$$G_{x\alpha 0} = \cos[C_{x\alpha} \tan^{-1}\{B_{x\alpha}S_{Hx\alpha} - E_{x\alpha}(B_{x\alpha}S_{Hx\alpha} - \tan^{-1}(B_{x\alpha}S_{Hx\alpha}))\}], \tag{6.38}$$

$$\alpha_s = \alpha + S_{Hx\alpha}, \tag{6.39}$$

$$S_{Hx\alpha} = r_{Hx1}, \tag{6.40}$$

$$B_{x\alpha} = r_{Bx1} \cos([\tan^{-1}(r_{Bx2}\kappa)] \cdot \lambda_{x\alpha}), \tag{6.41}$$

$$C_{x\alpha} = r_{Cx1}, \tag{6.42}$$

$$E_{x\alpha} = r_{Ex1} + r_{Ex2} df_z. \tag{6.43}$$

When the friction coefficient of the road is changed to a value other than 1, CarMaker calculates a new parameter:

$$\mu_{effx,y} = \frac{\mu_{Road}}{\lambda_{\mu x,y}}. \tag{6.44}$$

where μ_{Road} is the friction coefficient of the road defined by the user. This parameter is then used instead of $\lambda_{\mu x}$ and $\lambda_{\mu y}$ in equations (6.8), (6.13), (6.18), and (6.23). [77]

The chosen parameters are presented in Appendix 1. The curves obtained with the parameters are shown in figure 33 (snow) and figure 34 (ice).

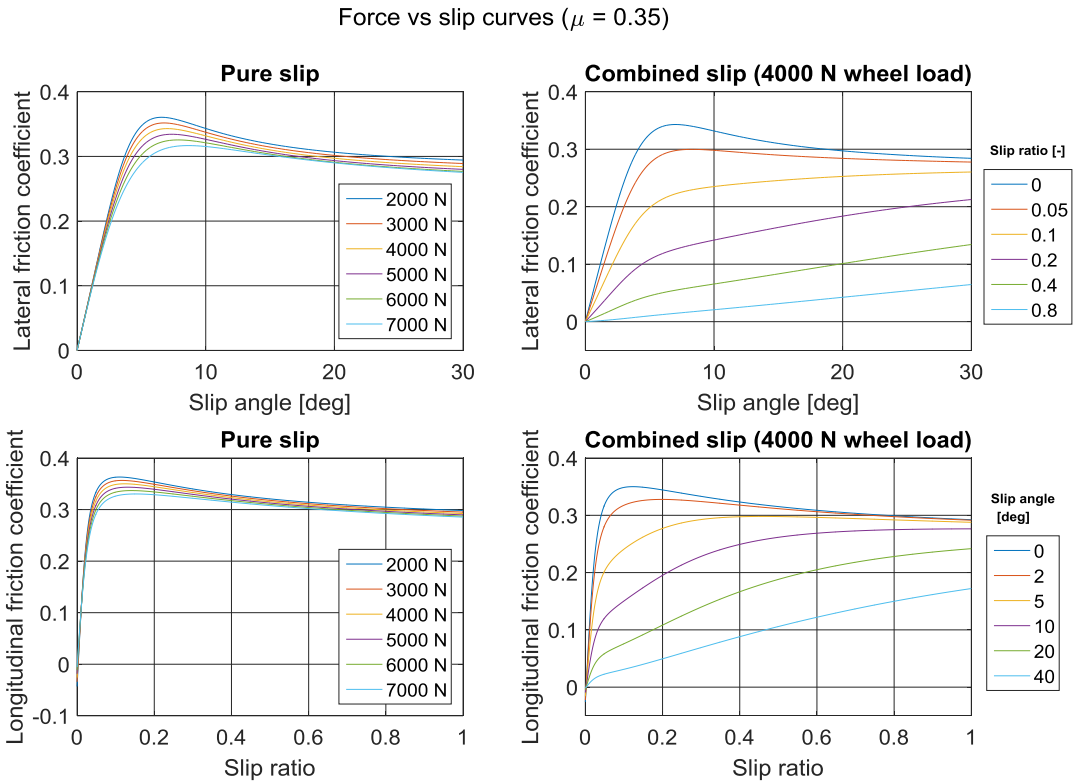

Figure 33 Tire force vs slip curves for snow, μ = 0.35

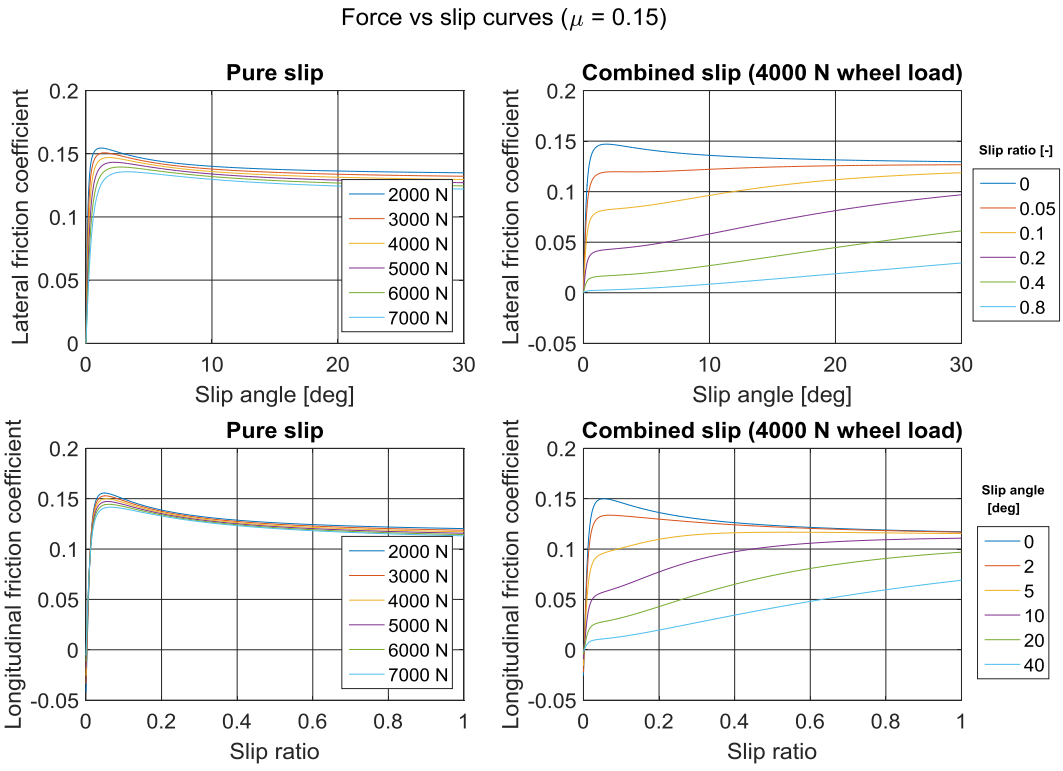

Figure 34 Tire force vs slip curves for ice, μ = 0.15

CarMaker also uses Pacejka's MF equations for calculating the tire moments. The parameters of the equations were left at the default values, as the moments are not relevant to this research. The equations and the default parameter values can be found in [24].

Furthermore, CarMaker also models the transient characteristics of tire forces. As the contact patch is connected flexibly to the wheel rim, the slip angle at the contact is not necessarily equal to that at the wheel. The same effect applies to the slip ratio. There is also delay in the effect that changes in vertical wheel load and camber have on the longitudinal and lateral forces. [5; 77] The relaxation length is the distance a tire has to roll before the force has fully built up [5]. The longitudinal and lateral relaxation lengths can be defined as:

$$\sigma_\kappa = F_z \cdot (p_{Tx1} + p_{Tx2} df_z) \cdot \exp(-p_{Tx3} df_z), \tag{6.45}$$

$$\sigma_\alpha = p_{Ty1} \sin\left[2 \tan^{-1}\left\{\frac{F_z}{p_{Ty2} F_{z0}}\right\}\right] \cdot \left(1 - p_{Ky3}|\gamma|\right) \cdot R_0 \lambda_{F_{z0}} \lambda_{\sigma\alpha} \tag{6.46}$$

where R_0 is the unloaded wheel radius, which is 0.3160 m in the case of the research vehicle. New definitions are now given for slip ratio and slip angle, which will be used to substitute κ and α in equations (6.4), (6.5), (6.29), and (6.39). They read:

$$\kappa' = \frac{u_{def}}{\sigma_\kappa} \operatorname{sgn}(v_x), \tag{6.47}$$

$$\tan(\alpha') = \frac{v_{def}}{\sigma_\alpha} \tag{6.48}$$

where the variables u_{def} and v_{def} describe the longitudinal and lateral deformations of the tire. They can be calculated from the following equations:

$$\sigma_\kappa \frac{du_{def}}{dt} + |v_x| u_{def} = -\sigma_\kappa (v_x - \Omega r_d), \tag{6.49}$$

$$\sigma_\alpha \frac{dv_{def}}{dt} + |v_x| v_{def} = \sigma_\alpha v_y. \tag{6.50}$$

In essence, these equations describe the transient behavior by low-pass filtering the slip ratio and the slip angle. [77]

6.2.3 Sensors and Sensor Noise

The friction estimation algorithm requires wheel speed sensor signals for each wheel, as well as acceleration and yaw, pitch, and roll rate signals from the IMU. CarMaker simulation models feature wheel speed sensors by default, though they need to be multiplied with the dynamic rolling radii of the wheels in order to have the signals in the same form as they are in the CAN bus of the real vehicle. Although CarMaker can output the constantly changing, accurate dynamic rolling radii during simulations, thus allowing them to be used as the multipliers, a constant estimate was used instead, as that is how the values in the CAN bus are calculated as well. The radius was estimated in CarMaker during a constant velocity simulation run. The obtained estimate was 0.3023 m. CarMaker also allows for custom

sensors to be attached to the body. Thus, an IMU was added to the simulated car in the same location and with the same orientation as in the real vehicle; on the centerline of the car, 0.62 m behind the CoG and 0.58 m above the ground with the positive direction of the x-axis pointing slightly downward with a pitch angle of 1.5 degrees.

The CarMaker sensor outputs contain no noise. Hence, it needs to be added manually. This can be done in Simulink by using the "Band-Limited White Noise" block to add some noise to the signals prior to them going into the friction estimation algorithm. In order to make the signals of the simulation model feature approximately the same amount of noise as the outputs of the real sensors, the variances of the noise in the real sensor signals were measured. The variances were calculated from data taken while driving in a straight line at a constant velocity, meaning that the accelerations, wheel speeds, and yaw, pitch, and roll rates were nearly constant. The measurement data was taken during driving rather than with the car being stationary because there is additional noise in the sensor outputs caused by vibrations when the vehicle is moving. In order for the noise variance in a virtual sensor to be equal to that of its real-world counterpart, the noise power value requested by the Simulink block, which is equal to the height of the power spectral density of the white noise, must be defined as the measured variance multiplied by the correlation time (sample time) of the noise [84]. The correlation time of the noise in the simulations was always set to 1 ms. The measured variances and the noise powers calculated based on them are presented in table 4.

Table 4 Sensor noise

Sensor(s)	Noise variance	Power spectral density height
Wheel speed sensors	$0.0035\ (m/s)^2$	$3.5 \cdot 10^{-6}\ (m/s)^2/Hz$
Longit. acceleration	$0.095\ (m/s^2)^2$	$9.5 \cdot 10^{-5}\ (m/s^2)^2/Hz$
Lateral acceleration	$0.16\ (m/s^2)^2$	$1.6 \cdot 10^{-4}\ (m/s^2)^2/Hz$
Yaw rate	$5 \cdot 10^{-5}\ (rad/s)^2$	$5 \cdot 10^{-8}\ (rad/s)^2/Hz$
Pitch rate	$3.9 \cdot 10^{-4}\ (rad/s)^2$	$3.9 \cdot 10^{-7}\ (rad/s)^2/Hz$
Roll rate	$8.3 \cdot 10^{-4}\ (rad/s)^2$	$8.3 \cdot 10^{-7}\ (rad/s)^2/Hz$

The estimation algorithm does also use the gas pedal position, brake pressure, and steering wheel angle sensor signals. However, those signals were seen to contain practically no noise. The simulated vehicles in CarMaker can output all of the aforementioned sensor signals by default.

6.2.4 Electronic Driver Aids

ABS, ESP, and TCS algorithms were implemented into the simulation model by using the Simulink-integrated version of CarMaker. The ABS and TCS algorithms that are supplied with the software were modified slightly, and a simple ESP system was created from scratch. These electronic driver aid models were not intended to be fully-fledged systems with the exact, complex operating principles of their real-world counterparts. Rather, their purpose was to function similarly to their real-world counterparts and indicate their states (on/off). The information about any one of the systems turning on could then be used as a trigger to start measuring the friction potential, as the vehicle would be on the limits of its handling.

6.2.4.1 Anti-lock Braking System

The ABS algorithm supplied with CarMaker for Simulink takes the longitudinal slip, rotational speed, and dynamic rolling radius of each tire as its inputs and controls the pressure at each wheel brake by adjusting the valves. The inputs are taken directly from CarMaker. Consequently, they are unrealistically accurate. To mitigate this issue, the system was changed to use the estimated constant value for the dynamic rolling radius. The user can control how much the algorithm gives weight to the slip ratio and the acceleration of the wheels in doing the valve adjustments.

Figure 35 demonstrates the behavior of the system during a heavy braking maneuver using the right front wheel as an example. It can be seen that the algorithm functions similarly to the Bosch anti-lock braking system presented in section 4.3.1.2. The velocity, acceleration, and brake pressure of the wheel keep repeating a cycle that gets shorter and shorter throughout the braking maneuver. At the end of the maneuver, the wheels lock up because the system is designed in such a way that it turns off once the velocity of the vehicle falls below 5 km/h.

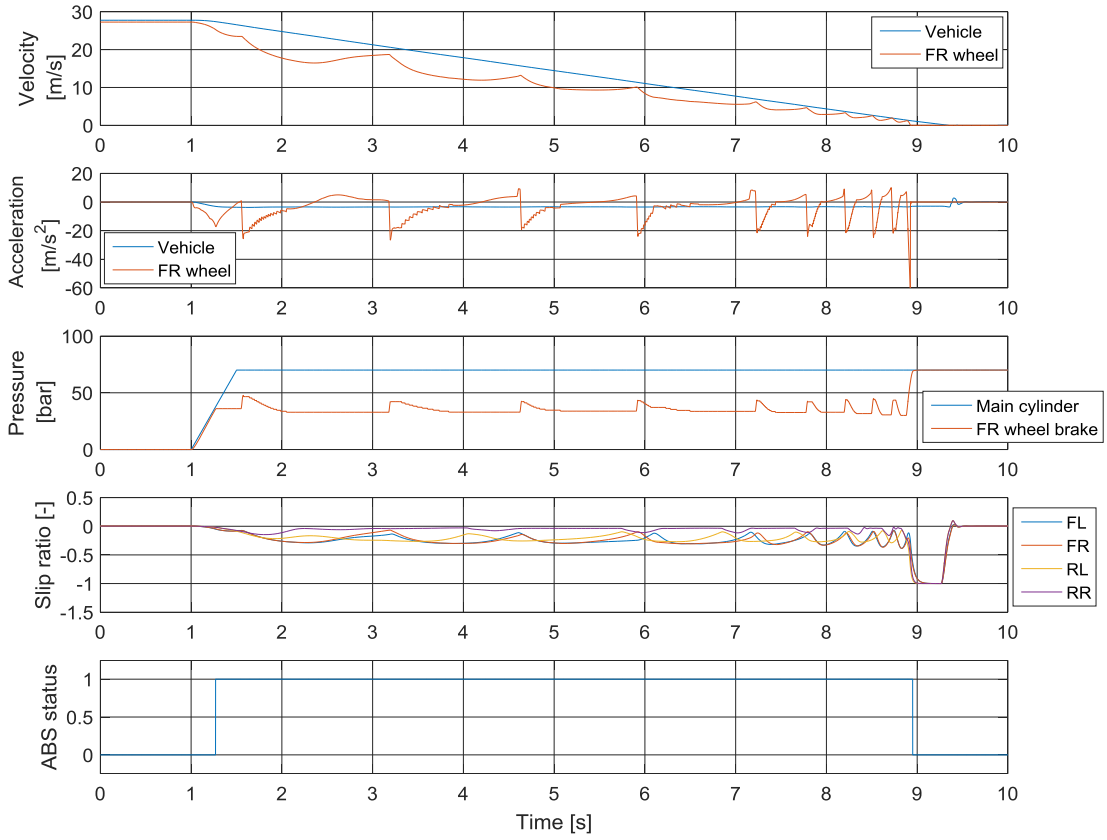

Figure 35 Heavy braking maneuver with ABS intervention, μ = 0.35

6.2.4.2 Electronic Stability Program

A simple ESP algorithm was created using the principles regarding yaw rate that were described in section 4.3.3. The system was designed to counter only oversteer, it does not react to understeer. It compares the actual yaw rate of the vehicle to the nominal yaw rate, which is calculated using equation (4.1). The nominal yaw rate is limited by the maximum

friction coefficient, as shown by equation (4.2). The characteristic speed of the vehicle, which is needed for the nominal yaw rate calculations, was obtained by doing a steady circle test, in which the simulated vehicle was accelerated slowly in a constant radius circle with the tire-road friction coefficient being 0.35. The yaw rate gain versus longitudinal velocity curve acquired from the test is presented in figure 36. The figure shows that the peak is achieved at approximately 15.915 m/s. The noise between 13.7 and 14.5 m/s was caused by the driver shifting gears.

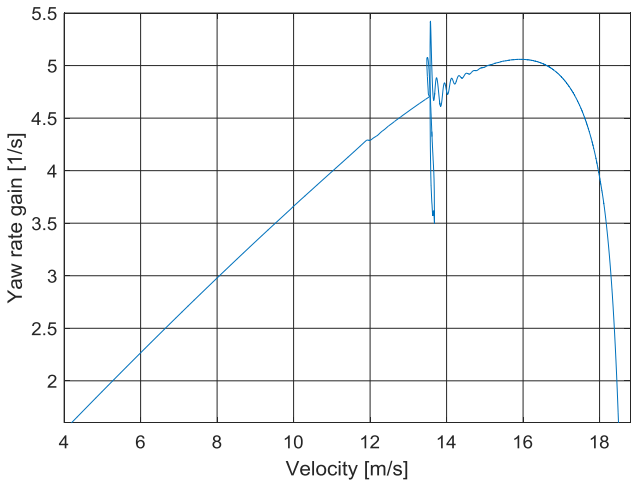

Figure 36 Yaw rate gain versus longitudinal velocity

The control system intervenes if the absolute value of the yaw rate is higher than the absolute value of the nominal yaw rate by a margin that is higher than a defined dead zone, i.e., the following equation holds true:

$$|\dot{\psi}| - |\dot{\psi}_{No}| > \varepsilon \tag{6.50}$$

where ε is the dead zone. The dead zone is a significant design parameter because it dictates how early on the intervention occurs. If the intervention is made at an early stage of a dangerous situation, the corrective action can be milder, and the probability of escalation is reduced. [85] The dead zone was defined as 1 °/s.

The block diagram of the controller is presented in figure 37. The “Wheel selection” block takes the yaw rate error, the sign of the yaw rate, and the longitudinal velocity as its inputs. Based on the sign, which indicates the direction of the cornering, it decides which front wheel it will forward the yaw rate error to. In order to combat oversteer, the outer front wheel must be braked, as the longitudinal braking force then generates a moment around the CoG that counters the rotation. The brake torques are kept at zero if the velocity of the vehicle is under 10 km/h. The yaw rate error goes into a lookup table, which outputs the additional torque that will be applied to the chosen front wheel brake. The yaw rate error must be higher than the dead zone in order for the added brake torque to be non-zero. The lookup table is defined such that when the error exceeds the dead zone, the torque increases by 45 Nm per 1 °/s of additional error.

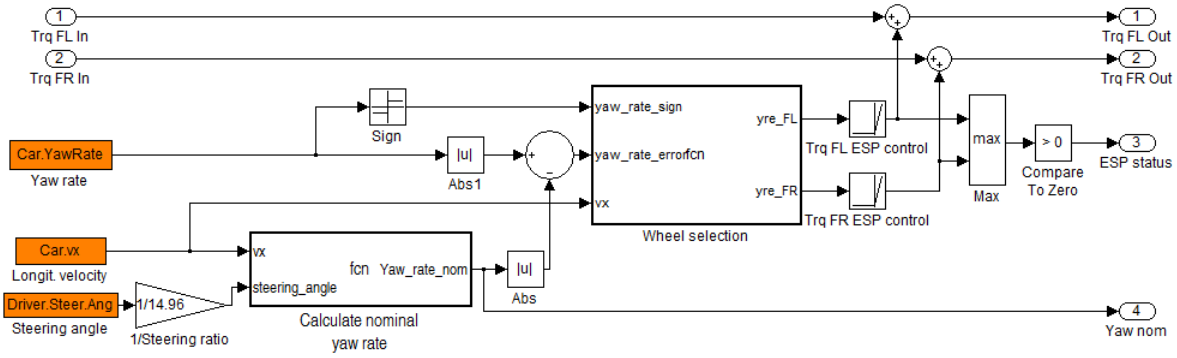

Figure 37 Block diagram of ESP controller

The ESP algorithm was tested by doing an ISO double lane change maneuver (figure 38) at 20 m/s with the friction coefficient being 0.35.

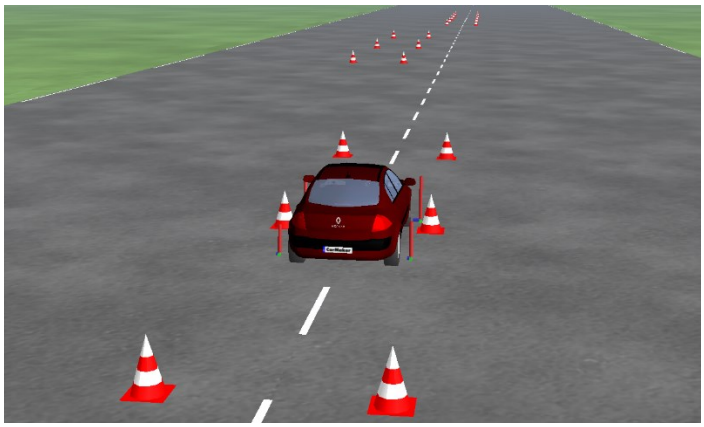

Figure 38 ISO double lane change in CarMaker

The test was run with and without the ESP system, and the results are presented in figure 39. The figure shows that the driver gradually lost control of the car in the test without ESP, eventually resulting in a spin. At the end of the maneuver, the car was travelling backwards; its side slip angle was nearly 200 degrees.

With the ESP turned on, the driver was able to complete the maneuver without issues; the absolute value of the side slip angle never exceeded 5 degrees. The figure shows that the ESP first braked the right front wheel as the driver steered to the left. Then, the left front wheel was braked as the car oversteered again when he steered right to go through the second set of cones and then aim for the final set. As the driver steered left in order to guide the car between the last set of cones, the ESP needed to perform a third intervention with the right front wheel. At that stage, the car was still slightly unstable, moving in a pendulum-like manner. Therefore, the ESP still had to do two smaller interventions to help straighten the car out.

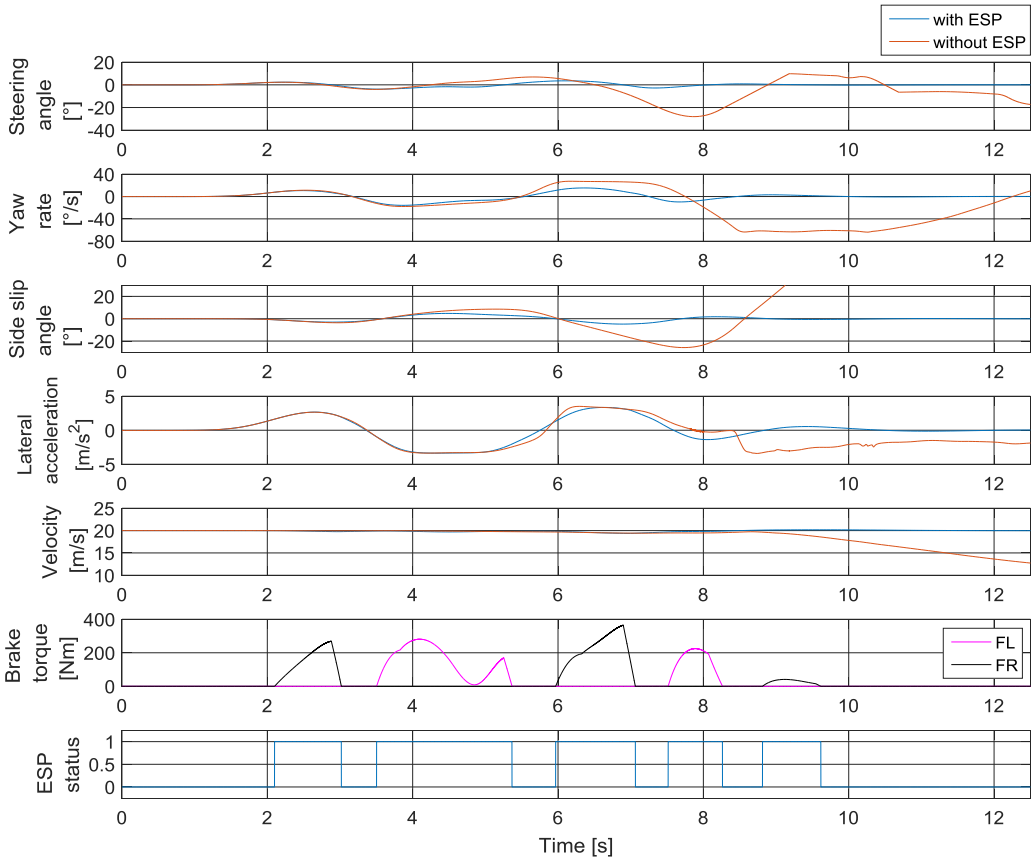

Figure 39 ISO double lane change at 20 m/s, μ = 0.35

6.2.4.3 Traction Control System

The traction control system (figure 40) controls the front wheel brake torques and the engine torque to keep the slip ratios of the driven wheels at a reasonable level. It aims to keep the ratios close to the value at which the longitudinal force reaches its peak. The system calculates the slip ratios of the front wheels with equation (3.12). The longitudinal velocity is calculated as the average velocity of the rear wheels. A minimum value is set for the velocity v_x that is beneath the division line in equation (3.12) so that the system thinks the slip ratios are smaller than they really are at speeds close to zero, thus intervening less. The minimum value was set to 1.67 m/s. The slip ratios are used as inputs in lookup tables that define the braking torques to be added to each of the front wheels. The torque is defined as zero up until the slip ratio of the wheel reaches the value 0.12, after which the torque starts to increase, reaching its maximum value of 500 Nm at a slip ratio of 0.22. The torques then enter a block where they will be disabled if the car is decelerating so that the system can only intervene during acceleration. The system also sets a limit to the maximum torque output of the engine. The maximum permissible torque is reduced by an amount equal to the current highest brake torque added by the TCS multiplied by 0.4. Thus, at lowest, the engine torque can be limited to a maximum of 50 Nm.

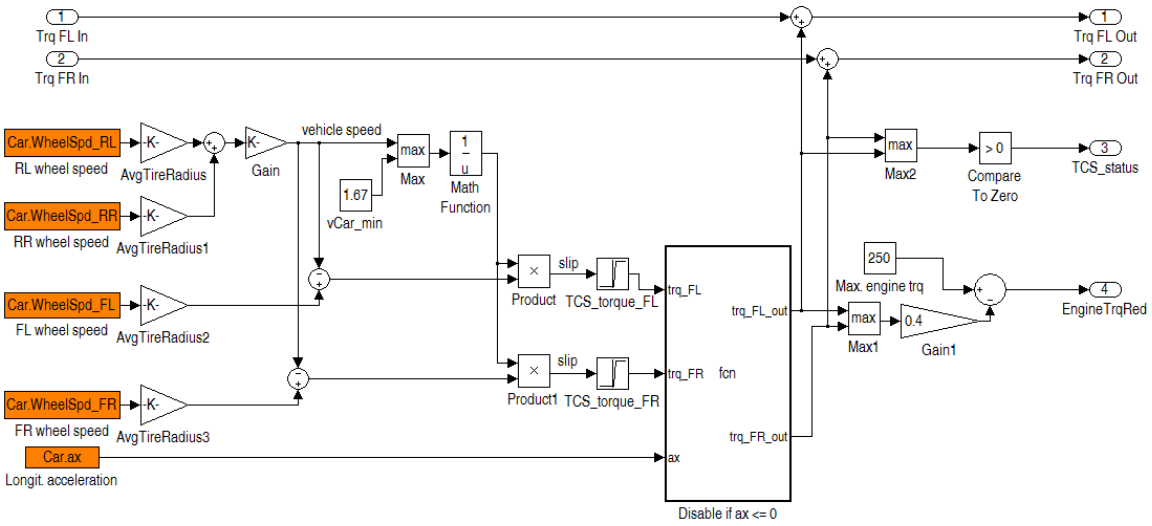

Figure 40 Block diagram of TCS controller

A test maneuver was run with the TCS enabled. Figure 41 shows that the slip ratios reached a high value at first as the added braking torques were low due to the set minimum velocity. As the maneuver progressed, the slip ratios were limited to approximately 0.18. It can also be seen that the system not only added brake torque but also limited the engine torque. As the driver engaged third gear at around 13 s into the maneuver, the traction control only had to intervene briefly despite the driver applying full throttle again. The driving torque at the wheels was not high enough anymore to cause the tires to reach the unstable region.

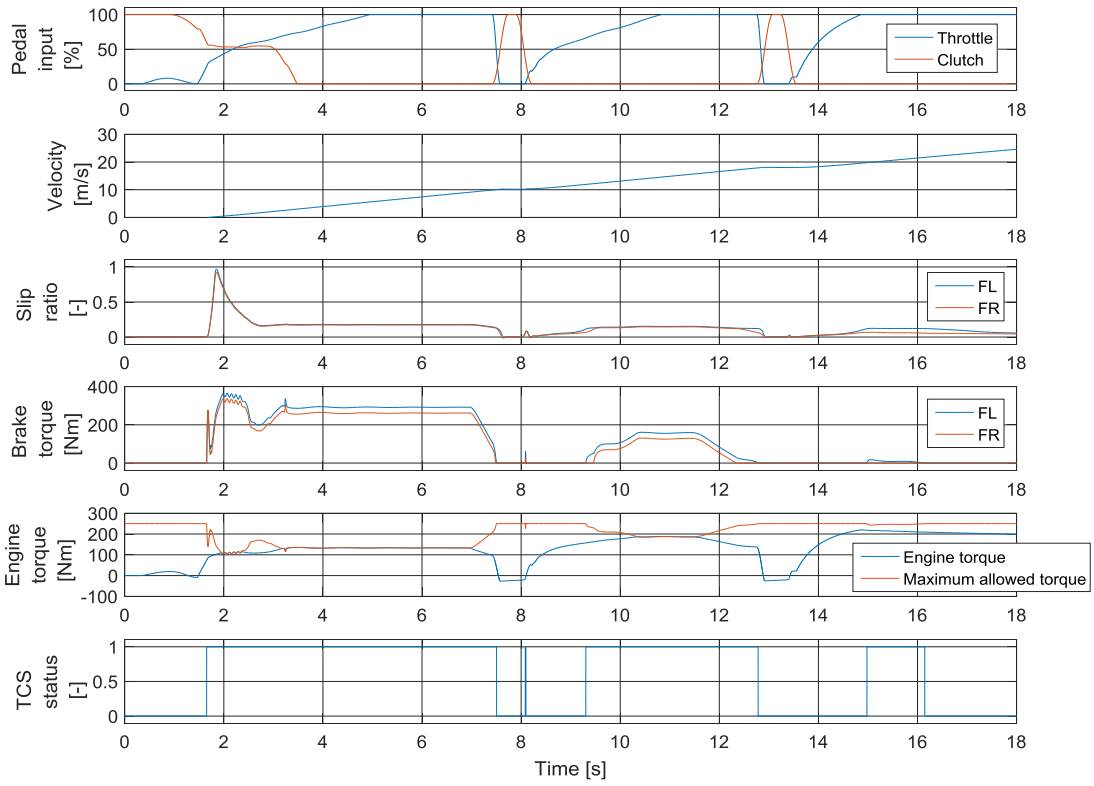

Figure 41 Acceleration with TCS intervention, μ = 0.35

7 Friction Estimation Algorithm

The operating principle of the friction estimation algorithm is largely based on the measurement data obtained with the inertial measurement unit. The longitudinal and lateral accelerations are limited by the friction potential and the inclination and bank angle of the road. Thus, by observing the accelerations while the vehicle is on the limits of its handling, the friction potential can be determined. The tire-road forces needed to change the yaw rate of the vehicle are also accounted for; this is done by using a modified version of the single-track model. In order to observe the effects of estimating the inclination and bank of the road on the accuracy of the estimation, three versions of the algorithm were created. The differences between them are as follows:

Version 1: Both the inclination and the bank angle are accounted for
Version 2: Only the inclination is accounted for
Version 3: Neither the inclination nor the bank angle is accounted for

The friction estimation algorithm does not take the suspension of the vehicle into consideration. Thus, it is assumed that the pitch and roll angles of the vehicle are equal to the inclination and bank of the road.

7.1 Signal Processing and Filtering

7.1.1 Moving Average Filter

The algorithm uses the moving average filter to reduce the noise in the sensor signals. The filter operates by averaging a specified number of data points from the input signal to produce each point in the output signal. It was chosen for filtering the sensor signals in the algorithm due to its effectiveness in reducing random noise whilst retaining a sharp step response. The filtering was configured such that the output is calculated as the average of N previous data points, including the latest point. Thus, in equation form, the output signal is written:

$$y[i] = \frac{1}{N}\sum_{j=0}^{N-1} x[i-j] \tag{7.1}$$

where $x[\,]$ is the input and $y[\,]$ is the output signal. [86] The delay caused by the filter is calculated with the following equation [87]:

$$d = (N-1)/2. \tag{7.2}$$

The filter reduces not only the amplitude of the noise but also the amplitude of the signal itself. Thus, the amount of data points used must be chosen so that the noise is adequately reduced while useful information in the signal is not lost. [86] Using 350 previous data points was seen to provide adequate filtering for the sensor signals listed in table 4. This yields a delay of 175 ms, as the sensors update their signals at a rate of 1000 Hz. The lateral acceleration measurement was corrected to the CoG according to equation (5.5) prior to filtering.

7.1.2 Kalman Filter

The Kalman filter estimates the state of a dynamic system by creating predictions of the state based on measurement data and then comparing new measurements to the predictions. The system is defined by the following equations [88]:

$$x_k = A_s x_{k-1} + w_{k-1}, \tag{7.3}$$

$$z_k = H x_k + v_k \tag{7.4}$$

where x_k is the state of the system, z_k is the measurement, A is the state transition matrix, H is the measurement matrix, and w_k and v_k represent the process and measurement noise. The *a priori* estimates of the current state x_k^- and error covariance P_k^- read:

$$x_k^- = A_s \hat{x}_{k-1}, \tag{7.5}$$

$$P_k^- = A_s \hat{P}_{k-1} A_s^T + Q \tag{7.6}$$

where Q is the process noise covariance matrix. $\hat{P}_{k-1}$ and $\hat{x}_{k-1}$ denote the estimated error covariance and state at the previous time step. The Kalman gain K_k is defined as:

$$K_k = P_k^- H^T (H P_k^- H^T + R)^{-1} \tag{7.7}$$

where R is the measurement noise covariance matrix. The *a posteriori* estimation of the current state $\hat{x}_k$ is calculated using the equation:

$$\hat{x}_k = x_k^- + K_k (z_k - H x_k^-) \tag{7.8}$$

where the Kalman gain is used to determine the weighting of the *a priori* estimate of the state and the residual $z_k - H x_k^-$. [88]

The Kalman filter assumes the process and measurement noise to be Gaussian white noise [59]:

$$p(w) \sim N(0, Q), \tag{7.9}$$

$$p(v) \sim N(0, R). \tag{7.10}$$

This assumption is not always correct during the operation of the algorithm. This will be discussed further in the upcoming sections.

When the filter is used for data fusion, the weighting of different measurement sources can be dynamically altered by changing the values in the measurement noise covariance matrix, as that then influences the Kalman gain. [66] This property of the filter is exploited in the algorithm in estimating the inclination angle of the road and the velocity of the vehicle. Additionally, the Kalman filter is also used to estimate the road bank angle. In order to employ the filter, the process and measurement noise covariance matrices must be defined, as well as the state-space representation. The measurement noise covariance matrices were defined by running appropriate maneuvers in the simulation software and measuring the

noise in the signals that the Kalman filters use as their measurement inputs. The process noise covariance matrices were then determined by iterating them and finding values that yielded the best results. The implementation of the filter for estimating the inclination, bank, and velocity will be discussed in more detail in the following sections.

7.2 Lateral Acceleration and Road Bank Estimation

The bank angle φ influences the cornering capabilities of the vehicle due to a component of gravity pulling the vehicle laterally. The wheel loads are also affected due to the direction of gravity no longer being parallel to that of the vertical tire-road forces. Additionally, when driving in a banked corner, the overall vertical load on the tires changes because of the vehicle having vertical acceleration. The lateral free body diagram of a vehicle is presented in figure 42. It is used in the algorithm to solve the total vertical load affecting the wheels. The total lateral force produced by the tires can also be solved from the diagram.

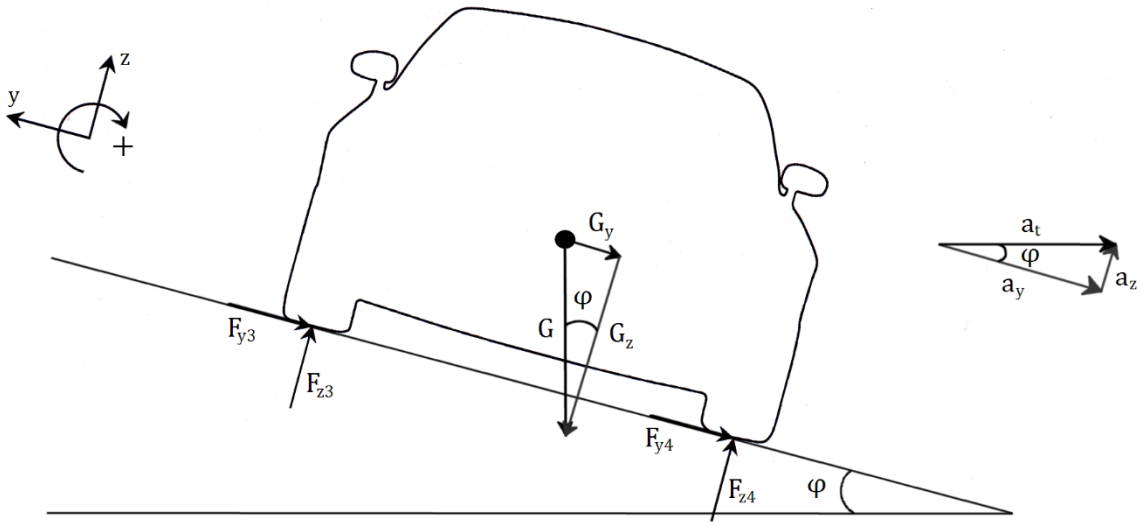

Figure 42 Free body diagram of a vehicle when viewed from behind

Vertical load transfers are neglected in the algorithm, resulting in the left and right side vertical loads being equal:

$$F_{z3} = F_{z4} = F_{z,tot}/2 \tag{7.11}$$

where $F_{z,tot}$ is the total combined vertical load of all the wheels.

Based on the free body diagram, Newton's equation of motion in the direction of the y-axis can be written as:

$$F_{y,tot} + G\sin(\varphi) = ma_y \tag{7.12}$$

where:

$$F_{y,tot} = \frac{F_{y3} + F_{y4}}{2}. \tag{7.13}$$

However, if the road also features inclination, the gravity that is visible in the free body diagram is no longer the full G, but $G \cdot \cos(\theta)$ instead. Equation (7.12) now becomes:

$$F_{y,tot} + G\cos(\theta)\sin(\varphi) = ma_y. \tag{7.14}$$

The total lateral force produced by the tires can be solved from equation (7.14):

$$F_{y,tot} = m\big(a_y + g\cos(\theta)\sin(\varphi)\big). \tag{7.15}$$

As has been discussed earlier, the acceleration measurements of the IMU are affected by gravity. Thus, when the road is banked, the lateral acceleration measurement features a component of the gravitational acceleration. Furthermore, the sensor is not located at the CoG, which must also be compensated for. The lateral acceleration at the CoG can be solved from equation (5.7), which yields:

$$a_y = a_{y,m} - \ddot{\psi} b_{is} - g\cos(\theta)\sin(\varphi). \tag{7.16}$$

Combining equations (7.15) and (7.16) yields:

$$F_{y,tot} = m\big(a_{y,m} - \ddot{\psi} \cdot b_{is}\big). \tag{7.17}$$

Assuming that the time derivative of the lateral velocity is zero at the center of gravity, the lateral acceleration can be solved from equation (3.4) as being equal to the centripetal acceleration:

$$a_y = u\dot{\psi}. \tag{7.18}$$

The bank angle can then be solved from equations (7.16) and (7.18):

$$\varphi_e = \sin^{-1}\left(\frac{a_{y,m} - \ddot{\psi} b_{is} - u\dot{\psi}}{g\cos(\theta)}\right). \tag{7.19}$$

The methods used to estimate the inclination angle θ and the longitudinal velocity u are explained in section 7.3. Additionally, the offset angle of the IMU, which was mentioned in section 5.2.3, causes some error in the yaw and roll rate measurements. Furthermore, when the bank angle is non-zero, the lateral acceleration measurement also contains error due to the offset, consequently affecting the bank estimation as well. However, such a small offset causes an almost negligible amount of error, and can thus be left unaccounted for in the lateral dynamics. It is only taken into consideration in estimating the inclination angle.

In order to improve the accuracy of the bank angle estimation, the algorithm uses a Kalman filter, which takes the measured roll rate and the estimated bank angle as its measurement inputs. Given that the bank angle can be written as:

$$\varphi_k = T_s\dot{\varphi}_{k-1} + \varphi_{k-1} \tag{7.20}$$

where T_s is the sample time and $\dot{\varphi}_{k-1}$ is the roll rate at instant $k-1$, the state-space representation for the Kalman filter is:

$$\begin{bmatrix}\dot{\varphi}_k \\ \varphi_k\end{bmatrix} = \begin{bmatrix}1 & 0 \\ T_s & 1\end{bmatrix}\begin{bmatrix}\dot{\varphi}_{k-1} \\ \varphi_{k-1}\end{bmatrix} + \begin{bmatrix}1 & 0 \\ 0 & 1\end{bmatrix}\begin{bmatrix}w_{\varphi,1,k-1} \\ w_{\varphi,2,k-1}\end{bmatrix}. \tag{7.21}$$

where $\dot{\varphi}_k$ is the roll rate and φ_k is the bank angle at instant k.

The measurement reads:

$$z_k = \begin{bmatrix}1 & 0 \\ 0 & 1\end{bmatrix}\begin{bmatrix}\dot{\varphi}_{m,k} \\ \varphi_{e,k}\end{bmatrix} \tag{7.22}$$

where $\dot{\varphi}_{m,k}$ is the roll rate measured by the IMU, and $\varphi_{e,k}$ is the bank angle estimation obtained using equation (7.19).

The values for the measurement noise covariance matrix were chosen by measuring the variance of the noise in the filtered roll rate and bank angle estimated with equation (7.19) during a cornering maneuver. The covariance matrix was defined as:

$$R_\varphi = \begin{bmatrix}2.5 \cdot 10^{-6} & 0 \\ 0 & 8.6 \cdot 10^{-6}\end{bmatrix}. \tag{7.23}$$

The process noise covariance matrix reads:

$$Q_\varphi = \begin{bmatrix}1.4 \cdot 10^{-10} & 0 \\ 0 & 1.4 \cdot 10^{-10}\end{bmatrix}. \tag{7.24}$$

The noise in the measurement signals is not always Gaussian white noise. When the time derivative of the lateral velocity of the CoG is non-zero, the lateral acceleration is no longer equal to the centripetal acceleration, as per equation (3.4). Thus, the road bank estimation will be adversely affected; it will gain an error offset. Similarly, error in the estimate of the inclination angle will cause an erroneus offset in the bank estimation, as can be seen from equation (7.19). However, the algorithm does not have the ability to calculate the side slip angle, nor can it know how accurate its own inclination angle estimate is. Consequently, the measurement noise covariance matrix cannot be altered based on how reliable the information in the incoming bank angle estimation is, as the reliability of the estimate cannot be known.

The bank angle estimation that the Kalman filter outputs is used by the algorithm to estimate the real lateral acceleration, compensating the effect of gravity from the lateral acceleration measurement of the IMU:

$$a_{y,e} = a_{y,m} - \ddot{\psi} b_{is} - g\cos(\theta_e)\sin(\varphi_e). \tag{7.25}$$

where φ_e is the bank angle output of the Kalman filter and θ_e is the inclination angle estimation that is acquired from the longitudinal dynamics.

The bank angle and the estimated lateral acceleration are then used to estimate the overall vertical force affecting the four wheels of the car. The equation of motion in the direction of the z-axis reads:

The vertical equation of motion reads:

$$F_{z,tot} - G\cos(\theta)\cos(\varphi) = ma_y \tan(-\varphi). \tag{7.26}$$

Equation (7.26) assumes that the inclination angle of the road is constant so vertical acceleration is only caused by the banking in the corner. By solving the total combined vertical load from equation (7.26), it can be estimated as:

$$F_{z,tot,1} = m\big(a_{y,e}\tan(-\varphi_e) + g\cos(\theta_e)\cos(\varphi_e)\big). \tag{7.27}$$

For the version of the algorithm that only accounts for the inclination angle, equation (7.27) reduces to:

$$F_{z,tot,2} = mg\cos(\theta_e), \tag{7.28}$$

and in the version that does not account for either the inclination or the bank, the total vertical load is calculated as:

$$F_{z,tot,3} = mg. \tag{7.29}$$

The estimated vertical loads can then be used in determining the axle loads based on the longitudinal dynamics of the vehicle, which will be explained in the following section.

7.3 Longitudinal Acceleration and Road Inclination Estimation

The error offset angle of the IMU needs to be accounted for in the longitudinal acceleration measurements. The measured acceleration is now written as:

$$a_{x,m} = a_x\cos(\varepsilon_{is}) + g\sin(-\theta - \varepsilon_{is}) \tag{7.30}$$

where ε_{is} is the error, which was measured to be +1.5 degrees. Due to the directions in the CarMaker coordinate system, the inclination angle gets a negative value in an uphill, which is why its sign has been changed from equation (5.6). The error in the acceleration measurement that is caused by the error angle is not constant; it depends on the acceleration and the inclination angle. However, the $\cos(\varepsilon_{is})$ term only causes a 0.3 % error for the a_x term, and the error caused in the $\sin(-\theta - \varepsilon_{is})$ term is almost constant at modest inclination angles. The error caused in the gravitational component seen in the acceleration measurement can be calculated as:

$$g_e = g\sin(-\theta - \varepsilon_{is}) - g\sin(-\theta). \tag{7.31}$$

As figure 43 demonstrates, the error g_e does not change drastically within the range of inclination angles typically found on real roads. Thus, the overall error in the longitudinal acceleration measurement caused by ε can be corrected by approximating it as a constant offset. The offset was chosen to be 0.2567 m/s^2, which is the absolute value of the error that ε causes when the vehicle has no longitudinal acceleration and the inclination angle is zero. Correcting the acceleration measurement with the offset means that the measured acceleration is approximated to be:

$$a_{x,m} = a_x + g\sin(-\theta) - a_{x,o} \tag{7.32}$$

where $a_{x,o}$ is the chosen offset. The offset-corrected measurement can thus be written as:

$$a_{x,m,c} = a_{x,m} + a_{x,o} = a_x + g\sin(-\theta). \tag{7.33}$$

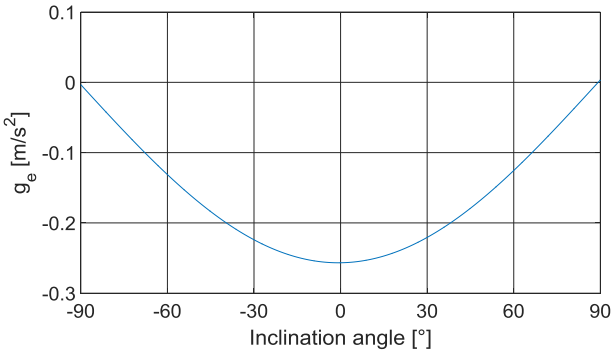

Figure 43 Error g_e as a function of inclination angle

The inclination angle affects the acceleration capabilities of the vehicle. When the angle is non-zero, a component of gravity is pulling on the vehicle longitudinally. Furthermore, the overall vertical load is reduced. The longitudinal free body diagram of a vehicle in an incline is presented in figure 44. It is used in the algorithm to calculate the vertical loads for each axle and to solve the total longitudinal force produced by the tires. The estimation of the inclination angle, velocity, and slip ratios will also be discussed in this section.

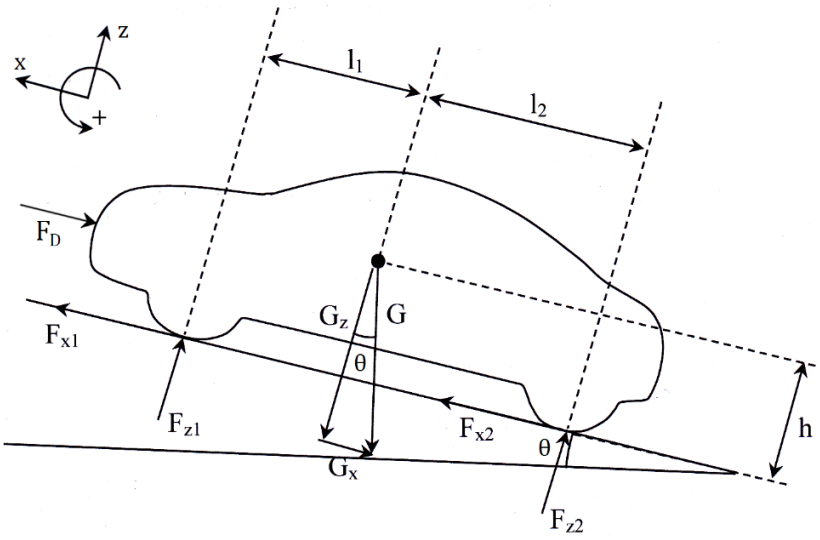

Figure 44 Free body diagram of a vehicle from the side

In the case of acceleration, the overall longitudinal force produced by the tires is equal to the longitudinal force produced by the front tires, as the vehicle is front-wheel driven. Under braking, all four tires produce longitudinal force. The equation of motion in the direction of the x-axis is:

$$F_{x,tot} - G\sin(-\theta) - F_D = ma_x \tag{7.34}$$

where $F_{x,tot}$ is the total longitudinal force produced by the tires and F_D is the aerodynamic drag. The tires also have a minor amount of rolling resistance but that is neglected in these calculations. The drag can be solved from the following equation [16]:

$$F_D = \frac{\rho}{2} c_D A u^2 \tag{7.35}$$

where ρ is the density of the air, c_D is the drag coefficient, and A is the frontal reference area. The total longitudinal force can be solved from equation (7.34) as:

$$F_{x,tot} = G\sin(-\theta) - \frac{\rho}{2} c_D A u^2 = m(a_x + g\sin(-\theta)) + \frac{\rho}{2} c_D A u^2. \tag{7.36}$$

Combining equations (7.33) and (7.36) yields:

$$F_{x,tot} = m a_{x,m,c} + \frac{\rho}{2} c_D A u^2. \tag{7.37}$$

The equation of motion in the direction of the z-axis can be written as:

$$F_{z1} + F_{z2} = F_{z,tot} \tag{7.38}$$

where $F_{z,tot}$ can be substituted according to equation (7.27), (7.28), or (7.29). The equation of rotational motion with respect to the CoG is:

$$F_{x,tot} h + F_{z1} l_1 - F_{z2} l_2 = 0. \tag{7.39}$$

It is assumed that the resultant point of the drag force is located at the height of the center of gravity, meaning that it does not cause any torque around the CoG. The front axle load can be solved from equation (7.39) by combining it with equations (7.37) and (7.38):

$$F_{z1} = \frac{-\left(m a_{x,m,c} + \frac{\rho}{2} c_D A u^2\right) h + F_{z,tot} l_2}{l}, \tag{7.40}$$

where l is the wheelbase of the vehicle. Substituting $F_{z,tot}$ with the three different versions from equations (7.27), (7.28), and (7.29) yields the front axle load for the three different variants of the algorithm. For the variant that accounts for both the inclination and the banking, the front axle load reads:

$$F_{z1,1} = \frac{-\left(m a_{x,m,c} + \frac{\rho}{2} c_D A {u_e}^2\right) h + m\left(a_{y,e}\tan(-\varphi_e) + g\cos(\theta_e)\cos(\varphi_e)\right) l_2}{l} \tag{7.41}$$

where u_e is the estimated longitudinal velocity. In the version that takes the inclination angle into consideration but assumes the bank angle to be zero at all times, the load is defined as:

$$F_{z1,2} = \frac{-\left(m a_{x,m,c} + \frac{\rho}{2} c_D A {u_e}^2\right) h + m g\cos(\theta_e)\, l_2}{l}, \tag{7.42}$$

and for the variant that assumes both inclination and bank angle to be zero, the load reads:

$$F_{z1,3} = \frac{-\left(ma_{x,m,c} + \frac{\rho}{2} c_D A {u_e}^2\right) h + mgl_2}{l}. \tag{7.43}$$

As equations (7.37) and (7.40) – (7.43) show, the inclination angle, bank angle, and longitudinal velocity need to be known in order to calculate the longitudinal and vertical axle forces. The inclination angle can be solved from equation (7.32) as:

$$\theta = \sin^{-1}\left(\frac{a_x - a_{x,m,c}}{g}\right). \tag{7.44}$$

As can be deduced from equation (7.44), an estimation for the longitudinal acceleration of the vehicle must be acquired in order to calculate the inclination angle. The acceleration can be estimated as a time derivative of a velocity estimation that is calculated based on the wheel speeds. First, the wheel speeds must be corrected from the wheel ground contact points to the center of gravity:

$$v_{x,FL,c} = \left(\Omega_{FL} r_{d,e} + \dot{\psi}\frac{b_1}{2}\right) \cdot \cos(\delta), \tag{7.45}$$

$$v_{x,FR,c} = \left(\Omega_{FR} r_{d,e} - \dot{\psi}\frac{b_1}{2}\right) \cdot \cos(\delta), \tag{7.46}$$

$$v_{x,RL,c} = \left(\Omega_{RL} r_{d,e} + \dot{\psi}\frac{b_2}{2}\right), \tag{7.47}$$

$$v_{x,RR,c} = \left(\Omega_{RR} r_{d,e} - \dot{\psi}\frac{b_2}{2}\right) \tag{7.48}$$

where $r_{d,e}$ is the estimated value of the dynamic rolling radius, which was defined as 0.3023 m, b_1 is the front track width, and b_2 is the rear track width. [66] An estimation for the velocity of the vehicle is then formed by calculating the velocity as the average speed of the two rear wheels while the vehicle is accelerating. When the brake pressure exceeds a defined threshold, the velocity is then taken as the highest of the four wheel speeds, as the wheels will start to slip. An estimation for the inclination angle is obtained by calculating the time derivative of this estimated velocity, which is then inserted into equation (7.44).

However, this estimate is not accurate when the vehicle is braked heavily, as all four wheels will be slipping at that point, and their accelerations will be in constant flux due to the interference of the anti-lock braking system. Thus, a Kalman filter was implemented to enhance the inclination estimation. The inclination angle can be written as:

$$\theta_k = T_s \dot{\theta}_{k-1} + \theta_{k-1} \tag{7.49}$$

where $\dot{\theta}_{k-1}$ is the pitch rate and θ_{k-1} the inclination angle at instant $k-1$. Therefore, the state-space equation for the Kalman filter is be defined as:

$$\begin{bmatrix}\dot{\theta}_k \\ \theta_k\end{bmatrix} = \begin{bmatrix}1 & 0 \\ T_s & 1\end{bmatrix}\begin{bmatrix}\dot{\theta}_{k-1} \\ \theta_{k-1}\end{bmatrix} + \begin{bmatrix}1 & 0 \\ 0 & 1\end{bmatrix}\begin{bmatrix}w_{\theta,1,k-1} \\ w_{\theta,2,k-1}\end{bmatrix}. \tag{7.50}$$

The measurement reads:

$$z_k = \begin{bmatrix}1 & 0 \\ 0 & 1\end{bmatrix}\begin{bmatrix}\dot{\theta}_{m,k} \\ \theta_{e2,k}\end{bmatrix} \tag{7.51}$$

where $\dot{\theta}_{m,k}$ is the pitch rate measured by the IMU, and $\theta_{e2,k}$ is the inclination angle estimate obtained using equation (7.44) at instant k.

Two different measurement noise covariance matrices were created for different driving situations in order to allow the Kalman filter to function effectively despite the noise not being white. By changing the matrix during operation, the emphasis that the Kalman filter places on each measurement input can be varied [66]. The values for the matrices were chosen by measuring the variance of the noise in the measurement signals $\dot{\theta}_{m,k}$ and $\theta_{e,k}$ during two different maneuvers. The first one was an acceleration maneuver, during which $\theta_{e,k}$ should be reliable due to the rear wheels not slipping, and the second one was a heavy braking maneuver. As was mentioned before, the inclination estimation acquired using equation (7.44) is not reliable during heavy braking, containing vast amounts of noise. The matrix that is based on the acceleration maneuver ($R_{\theta,1}$) is used by default, but when the brake pressure exceeds a set threshold, the matrix that was created based on the braking maneuver is used instead. An exception to this is when the velocity of the vehicle is zero (with certain tolerances). In that situation, $\theta_{e,k}$ is reliable even if the brake is being pressed heavily, and the filter will thus use the default matrix. By using these rules, the Kalman filter puts less emphasis on $\theta_{e,k}$ when it is known not to be reliable. The measurement noise covariance matrices were defined as:

$$R_{\theta,1} = \begin{bmatrix}1.0 \cdot 10^{-6} & 0 \\ 0 & 3.9 \cdot 10^{-6}\end{bmatrix}, \tag{7.52}$$

$$R_{\theta,2} = \begin{bmatrix}1.0 \cdot 10^{-6} & 0 \\ 0 & 5.0 \cdot 10^{-2}\end{bmatrix}. \tag{7.53}$$

The process noise covariance matrix reads:

$$Q_\theta = \begin{bmatrix}5.0 \cdot 10^{-10} & 0 \\ 0 & 5.0 \cdot 10^{-10}\end{bmatrix}. \tag{7.54}$$

The inclination-compensated longitudinal acceleration estimation can be written as:

$$a_{x,e} = a_{x,m,c} - g\sin(-\theta_e). \tag{7.55}$$

where θ_e is the inclination angle output of the Kalman filter. The rate of change of the inclination angle was limited to 1 degree per meter so that the angle would not suddenly change drastically as a consequence of bumps and other noise. The rate was not limited at low speeds, however, so that the algorithm could identify the inclination of the road when the vehicle is stopped.

As mentioned previously, the velocity estimate calculated for the inclination angle estimation is not reliable under heavy braking due to wheel slip. A more accurate estimate for the velocity can be acquired with a Kalman filter using the inclination-compensated acceleration and the wheel speeds calculated with equations (7.45) – (7.48). [66] This estimate should not be used to calculate the acceleration for the inclination estimation, as that would then create a loop between the inclination and velocity estimations, which could cause equations to become unsolvable. It was found, however, that the Kalman filter based velocity estimate could be used in the measurement noise covariance matrix selection logic of the filter that estimates the inclination.

The longitudinal velocity of the CoG can be written as:

$$u_k = T_s a_{x,k-1} + u_{k-1}. \tag{7.56}$$

Consequently, the state-space equation for the filter is:

$$\begin{bmatrix} a_{x,k} \\ u_k \end{bmatrix} = \begin{bmatrix} 1 & 0 \\ T_s & 1 \end{bmatrix} \begin{bmatrix} a_{x,k-1} \\ u_{k-1} \end{bmatrix} + \begin{bmatrix} 1 & 0 \\ 0 & 1 \end{bmatrix} \begin{bmatrix} w_{u,1,k-1} \\ w_{u,2,k-1} \end{bmatrix}. \tag{7.57}$$

The measurement reads:

$$z_k = \begin{bmatrix} 1 & 0 \\ 0 & 1 \\ 0 & 1 \\ 0 & 1 \\ 0 & 1 \end{bmatrix} \begin{bmatrix} a_{x,e} \\ v_{x,FL,c} \\ v_{x,FR,c} \\ v_{x,RL,c} \\ v_{x,RR,c} \end{bmatrix}. \tag{7.58}$$

In the version of the algorithm that does not account for inclination, the Kalman filter uses $a_{x,m,c}$ instead of $a_{x,e}$ in equation (7.58).

The wheel speeds contain systematic slip-dependent offsets, which contradicts the assumption about the measurement noise being white. The rear wheels have next to no longitudinal slip during any situation other than heavy braking. On the other hand, the front wheels may also slip during acceleration. The acceleration estimation that isn't inclination-compensated also has an offset when the inclination angle is non-zero. [66] In order to apply the Kalman filter in spite of these systematic errors, two measurement noise covariance matrices were created again for different driving situations. The default matrix $R_{u,1}$ represents the noise during heavy acceleration when the front wheels are slipping. The second matrix $R_{u,2}$ represents the noise in a heavy braking maneuver, during which all the wheel speed signals contain significant amounts of noise. The default matrix, which makes the Kalman filter put highest emphasis on the rear wheel speeds while still also accounting for the acceleration signal and the front wheel speeds, is used in all situations except when the brake pressure exceeds a set threshold. The second matrix forces the filter to rely almost solely on the acceleration signal. Similar to the way the inclination estimation was configured, the default matrix is used when the velocity is close to zero even if the brake pressure is high so that the estimation can correctly recognize when the vehicle is not moving. The variance of the acceleration signal was measured, as was the variance of the rear wheel speeds during acceleration. The rest of the values in the matrices were determined

by running simulated test runs and iterating them to find values that were seen to yield the most accurate estimation results. The same matrices were used for both versions of the filter. The measurement noise covariance matrices were defined as:

$$R_{u,1} = \begin{bmatrix} 9.8 \cdot 10^{-5} & 0 & 0 & 0 & 0 \\ 0 & 2.3 \cdot 10^{-4} & 0 & 0 & 0 \\ 0 & 0 & 2.3 \cdot 10^{-4} & 0 & 0 \\ 0 & 0 & 0 & 9.2 \cdot 10^{-7} & 0 \\ 0 & 0 & 0 & 0 & 9.2 \cdot 10^{-7} \end{bmatrix}, \tag{7.59}$$

$$R_{u,2} = \begin{bmatrix} 9.8 \cdot 10^{-5} & 0 & 0 & 0 & 0 \\ 0 & 1.2 & 0 & 0 & 0 \\ 0 & 0 & 1.2 & 0 & 0 \\ 0 & 0 & 0 & 1.2 & 0 \\ 0 & 0 & 0 & 0 & 1.2 \end{bmatrix}. \tag{7.60}$$

The process noise covariance matrix reads:

$$Q_u = \begin{bmatrix} 9.8 \cdot 10^{-9} & 0 \\ 0 & 9.8 \cdot 10^{-9} \end{bmatrix}. \tag{7.61}$$

With the inclination angle and the velocity being estimated, the total longitudinal force and the front axle vertical load can be estimated using equations (7.37) and (7.41) – (7.43). Furthermore, the slip ratio of each wheel can be estimated as:

$$\kappa_{ij} = -\frac{u_e - v_{x,ij,c}}{u_e} \tag{7.62}$$

where $v_{x,ij,c}$ stands for the wheel speeds calculated in equations (7.45) – (7.48). The estimated slip ratios are needed as part of the friction potential estimation trigger rules, which will be discussed in section 7.5. The slip ratio estimation is only started when the velocity of the vehicle exceeds 1 km/h.

7.4 Modified Single-Track Model

The tire-road forces are not only needed for the longitudinal and lateral accelerations but also for changing the yaw rate of the vehicle. To accommodate for this in the friction estimation algorithm, a modified version of the single-track model was used. This should improve the accuracy of the estimation particularly in low-speed cornering maneuvers where the yaw rate can change rapidly.

Most of the assumptions with the single-track model that were discussed in section 3.1 are now disregarded. It is still assumed that the suspension system is rigid, meaning that the body does not roll or pitch. Lateral load transfers are still disregarded, as the model is not capable of accounting for them. The longitudinal force produced by the tires on the front axle is now included. The model is used for calculating the friction coefficient only when the vehicle is not being braked, as adding the longitudinal force produced by the rear tires would make the equations unsolvable due to there being too many unknown variables. The modified version of the model is presented in figure 45. The side slip angle of the CoG is assumed to be zero.

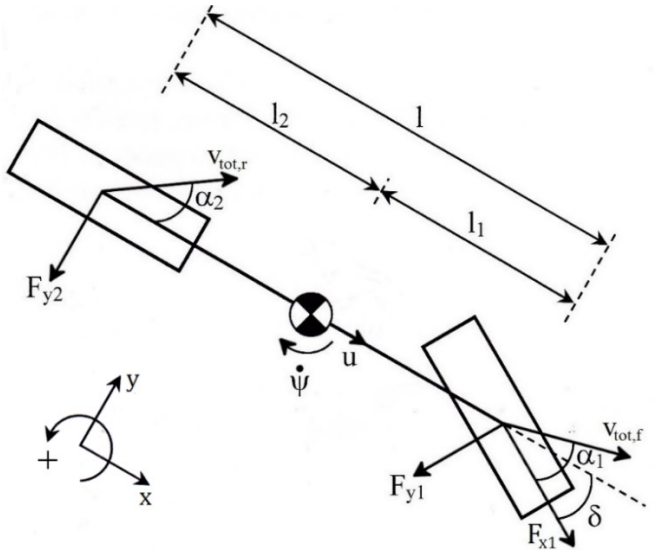

Figure 45 Modified single-track model used in the algorithm

The equations of motion can be written with the aid of equations (7.17) and (7.37) as:

$$\sum F_x = ma_{x,m,c} + \frac{\rho}{2} c_D A u^2 = F_{x1}\cos(\delta) - F_{y1}\sin(\delta), \tag{7.63}$$

$$\sum F_y = m\left(a_{y,m} - \ddot{\psi}\cdot b_{is}\right) = F_{x1}\sin(\delta) - F_{y1}\cos(\delta) + F_{y2}, \tag{7.64}$$

$$\sum M_z = I_{zz}\ddot{\psi} = \left(F_{x1}\sin(\delta) - F_{y1}\cos(\delta)\right)l_1 + F_{y2}l_2. \tag{7.65}$$

The front axle tire forces can be solved from equations (7.63) – (7.65) as:

$$F_{x1} = \frac{ma_{x,m,c} + \frac{\rho}{2} c_D A u^2}{\cos(\delta)} + \frac{\begin{pmatrix} I_{zz}\ddot{\psi} - \left(ma_{x,m,c} + \frac{\rho}{2} c_D A u^2\right)\tan(\delta) \\ +m\left(a_{y,m} - \ddot{\psi}\cdot b_{is}\right)l_2 \end{pmatrix}\tan(\delta)}{(\sin(\delta)\tan(\delta) + \cos(\delta))l}, \tag{7.66}$$

$$F_{y1} = \frac{I_{zz}\ddot{\psi} - \left(ma_{x,m,c} + \frac{\rho}{2} c_D A u^2\right)\tan(\delta) + m\left(a_{y,m} - \ddot{\psi}\cdot b_{is}\right)l_2}{(\sin(\delta)\tan(\delta) + \cos(\delta))l}. \tag{7.67}$$

The longitudinal velocity estimated with the Kalman filter is used in these equations. Thus, the version of the algorithm that does not account for inclination angle will acquire different values for these forces.

The current friction coefficient is then solved as:

$$\mu_e = \frac{\sqrt{F_{x1}^2 + F_{y1}^2}}{F_{z1}} \tag{7.68}$$

where F_{z1} is the vertical load of the front axle, which is calculated with equation (7.41), (7.42), or (7.43) depending on the version of the algorithm.

When the brake pressure exceeds a specified low threshold, the single-track portion of the algorithm is neglected. The estimation is then done based on the measured accelerations using equations (7.17), (7.27) – (7.29), and (7.39). Thus, the coefficient is estimated as an average of all four wheels rather than just the front wheels. The estimation reads:

$$\mu_e = \frac{\sqrt{F_{x,tot}^2 + F_{y,tot}^2}}{F_{z,tot}} \tag{7.69}$$

where $F_{x,tot}$ is calculated according to equation (7.37), $F_{y,tot}$ according to equation (7.17), and $F_{z,tot}$ according to equation (7.27), (7.28), or (7.29) depending on the algorithm version.

The coefficient is estimated continuously. However, the vehicle is not on the limits of its handling for most of the duration of its operation, meaning that the calculated coefficient is not equal to the friction potential. Hence, the algorithm contains rules about determining when the coefficient can be assumed to be close to the potential.

7.5 Friction Potential Estimation

The estimated coefficient is assumed to be close to the friction potential when either the TCS or the ABS is on. Thus, either of these systems being activated is used as a rule to start estimating the potential. Additionally, if the slip ratio of either of the front wheels exceeds 0.15, the potential estimation is triggered as well. This additional rule was set because the TCS may not activate at low speeds. The potential is calculated as the average of the estimated friction coefficient during any period that any of these three rules is fulfilled. If the potential estimation is triggered within 10 seconds of previously being active, the new data points are added to the previously saved data and the potential is calculated as the average of all of the saved data. If none of the rules are fulfilled for over 10 seconds, the next time the potential estimation is triggered the previously logged data will be forgotten, and the estimation will be started anew.

The activation of the ESP is also used as a trigger rule. However, when the ESP is on, the assumption about the estimated coefficient being equal to the potential is less reliable. Thus, the ESP-based estimation was made to work differently. The potential is estimated by creating a histogram of the friction coefficient estimation data acquired during the ESP being active. The histogram consists of 24 bins with the lower limit being 0 and upper limit at 1.2, meaning that each bin covers a friction coefficient range of 0.05. The potential is then estimated as the upper limit of the bin that contains the most values. If the ESP is reactivated within 10 seconds of being previously on, the new data points are added to the previous data. Otherwise, the previous data will be disregarded upon the ESP reactivating.

When the algorithm starts operating, the potential estimation defaults to 1 and stays at that value until one of the rules is fulfilled and an estimation is obtained. Additionally, if none of the trigger rules are fulfilled for 30 seconds, the estimated potential will start approaching 1 at a rate of 0.5 per minute, as the previous potential estimation becomes increasingly unreliable.

8 Tests and Measurements

The test maneuvers needed to allow for inspecting the reliability of the friction potential estimation in the various difficult circumstances the algorithm was designed to be able to cope with. This meant that tests were performed on inclined, banked, and level roads in order to observe the effect of road inclination and bank angle estimation on the accuracy of the friction potential estimation using the three different algorithm versions. The ability of the algorithm to estimate the friction potential in start maneuvers with high steering angles was also examined. Additionally, the effects of varying friction potential and location of center of gravity were tested using the simulation software. All the maneuvers were performed aggressively enough so that the corresponding electronic driver aid would be on for most of the duration of the maneuver.

8.1 Simulations

The CarMaker software features a virtual driver model that is capable of operating the vehicle with user-defined limitations regarding maximum longitudinal and lateral accelerations and the rapidity of the inputs. The driver can be configured to either attempt to reach and maintain a specific speed or to stop the vehicle. Alternatively, the driver inputs can be completely customized by the user. The road sections are also entirely customizable, including their friction potentials. All of the simulated roads featured a constant friction potential of 0.35 with the exception of the varying friction tests where the potential switched between 0.15 and 0.35.

8.1.1 Effect of Road Inclination and Bank Angle Estimation

In order to test the effect of road inclination angle estimation on the accuracy of the algorithm, acceleration and braking maneuvers were performed on an inclined road. The first test was an acceleration maneuver that was done in an uphill road section. The road had an inclination angle of 7 degrees. The acceleration was carried out aggressively enough that the traction control system had to intervene. A braking maneuver was also performed on the same road but in the opposite direction. The car was first accelerated to 80 km/h on a level bit of road and then braked hard in the downhill section such that the ABS system would activate. These maneuvers also made it possible to examine the accuracy of the inclination estimation and the effect of the inclination on the velocity estimation. Additionally, a test consisting of accelerating and braking the car on a level road was performed in order to observe if the inclination estimation would make any difference on the friction estimation in that situation.

In order to study the combined effect of inclination and banking on the algorithm, a test run was done in a banked downhill 90-degree corner with a radius of 100 m. The car was accelerated up to speed on a level road that then became banked, descending to the left, and two hundred meters later also started sloping downwards, finally turning left another two hundred meters after the beginning of the downhill. The virtual driver was made to take the corner fast enough that the ESP would intervene. The bank angle of the road was 7 degrees, while the angle of the downhill was 5 degrees. The double lane change maneuver, which was previously used to showcase the operation of the ESP, was also used for testing the effect of bank angle estimation on the performance of the algorithm during cornering on a level road.

Finally, a start maneuver was carried out with the steering wheel turned 360 degrees to the left. The purpose of this maneuver was to test the ability of the friction estimation algorithm to account for a large portion of the front tire forces going towards increasing the yaw rate. Thus, this maneuver would test the effectiveness of the single-track model portion of the algorithm.

8.1.2 Effect of Varying Friction Potential

On real roads, the friction potential varies constantly, particularly in snowy and icy winter conditions. In order to simulate this and inspect the effects on the friction potential estimated by the algorithm, acceleration tests were run on a 50-meter strip of road where the friction potential switched between 0.15 and 0.35. The frequency at which the switching occurred was changed between the tests. Ten different frequencies ranging from 0.1 m to 1.0 m were used in the tests. Additionally, two tests were done with each frequency with the front tires being on the higher friction surface at the start in one test and the lower friction surface in the other. Thus, 20 test runs were done in total. The driver inputs were kept identical for all of the runs. The acceleration was performed in such a way that the TCS was on during most of the maneuver.

8.1.3 Effect of Varying Location of Center of Gravity

The location of the center of gravity of the vehicle can change significantly due to luggage, changing fuel load, and a different number of people sitting in the car. The effect these changes have on the accuracy of the friction estimation was tested by repeating the same simulated acceleration maneuver while changing the longitudinal weight distribution of the vehicle. The maneuvers were performed on a 50-meter strip, and the driver inputs were kept identical for each run. The TCS was activated for almost the entire duration of the maneuver. Ten runs were done. The front axle weight ranged from 53 % to 62 % with increments of 1 %.

8.2 Road Tests

In order to validate the results obtained with the simulation model, similar maneuvers were performed with the research vehicle. The test runs were done on suitable public roads. Uphill acceleration and downhill braking maneuvers were done on an inclined road that was covered in ice. The inclination of the road was measured to vary between 4.5 and 6 degrees. The road angle measurements were done with a digital inclinometer. In addition, a test run consisting of accelerating and braking the vehicle was performed on a moderately level strip of road that was covered in snow and ice. The road had some minor elevation changes with the starting point being sloped slightly downwards, after which the road levelled out. A start maneuver with a high steering angle was also performed on the same road in a spot that was nearly perfectly level.

The friction estimation capabilities of the algorithm during cornering were tested by accelerating the vehicle in a turn such that the traction control system intervened. The acceleration was performed in a right-hand corner that was followed by a slightly tighter left-hand corner. The road featured a minor uphill with the inclination increasing during the section from approximately 0 degrees to 3 degrees, returning back to 0 after the second corner. The corners were also slightly banked with the road descending towards the inside of the turn in both corners. The peak absolute value of the bank angle in both turns was approximately 3 degrees. The road was covered in snow and ice.

9 Results and Discussion

The results of the simulations and road tests are presented and discussed in this chapter. The measurements and estimations appropriate for each maneuver are presented in different graphs. The simulation results are shown first so that they can then be validated with the road test results. After the results have been presented and discussed in sections 9.1 and 9.2, the sources of error are summarized in section 9.3, and some comparisons are made to relevant previous studies in section 9.4.

9.1 Simulation Results

The simulation results are presented and discussed in this section. The acceleration and braking maneuver results are shown in figures 46 – 48, and the effects of inclination estimation and compensation are discussed. The results of the downhill banked corner maneuver are displayed in figure 49, after which the effects of combined bank and inclination estimation and compensation are examined. The double lane change maneuver results are presented in figure 50, and the effects of bank estimation and compensation on the friction estimation while driving on a level road are discussed. The results of the start maneuver with a high steering angle are shown in figure 51, and the effectiveness of the modified single-track model is then examined. Finally, the results of the varying friction potential and CoG simulations are presented and analyzed in sections 9.1.2 and 9.1.3. The delay in the estimations caused by the filtering has not been compensated for in the result graphs. In the graphs, all the curves that are not explicitly stated to be estimations are CarMaker outputs. The longitudinal and lateral acceleration sensor outputs in the graphs have been plotted after passing through the moving average filter. The lateral acceleration sensor signal has been corrected with the yaw acceleration.

9.1.1 Effect of Road Inclination and Bank Angle Estimation

The uphill acceleration maneuver results are presented in figure 46, which contains eight different graphs. The graphs represent the longitudinal velocity and acceleration, front tire slip ratios, car pitch angle and inclination estimation, TCS status (on/off), front axle vertical load, current friction coefficient, and estimated friction potential. The car pitch output by CarMaker is the sum of the inclination angle of the road and the pitch angle of the body relative to the road, which is caused by longitudinal load transfers affecting the suspension. Versions 2 and 3 of the algorithm are compared in these graphs, as the bank angle estimation is not relevant to this maneuver.

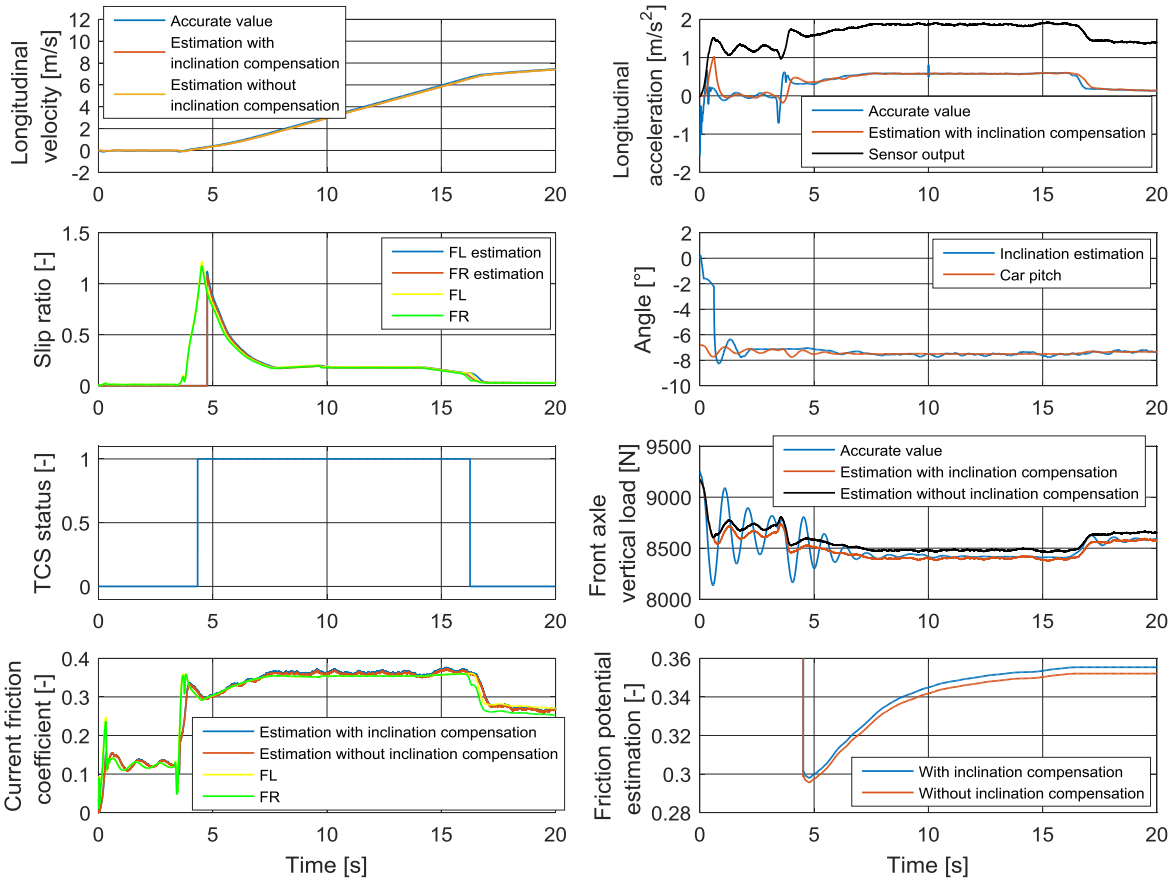

Figure 46 Simulated uphill acceleration maneuver results

The traction control system intervenes almost immediately when the car starts moving. It triggers the potential estimation before the vehicle reaches 1 km/h, and thus the slip ratio estimation does not serve a purpose in this maneuver. The estimated velocities are accurate, and there is next to no difference between the velocity estimations of the two algorithms. This is because both of them base their estimations primarily on the wheel speeds of the rear wheels in this situation. Thus, the longitudinal acceleration output of the IMU, which is much higher than the actual acceleration due to the inclination angle, does not skew the velocity estimation of the algorithm version that does not account for the inclination. During the period of steady acceleration between 8 s and 15 s, the sensor output shows the acceleration to be approximately 1.85 m/s^2 whereas the actual acceleration and the inclination-compensated estimation show it to be around 0.58 m/s^2. As there is no difference between the velocity estimations, there is also no difference between the two versions in the aerodynamic drag force calculations. Although, the drag force is small and inconsequential at such low speeds anyway. Thus, the longitudinal forces estimated by the two versions must also be nearly identical because the estimated velocity is the only variable that can cause a difference between them, as equation (7.66) shows. As a result, any differences between the friction coefficient and potential estimations of the two versions in this maneuver are left up to the front axle vertical load estimation.

The algorithm estimates the uphill, the angle of which is 7 degrees, to be slightly steeper than it really is. This is because the body pitches slightly as a result of the rear axle load increasing due to the inclination and the longitudinal acceleration. During the period of

steady acceleration between 8 s and 15 s, the pitch output of CarMaker is 7.5 degrees. The estimated inclination matches the output with good accuracy. Thus, the inclination-compensated longitudinal acceleration estimate is also close to the actual acceleration. It can be seen, however, that the difference in the front axle load estimation between the two versions is only in the range of approximately 70 to 80 N throughout the maneuver. This is because in both algorithm versions the effect of longitudinal tire forces on the front axle load is calculated from the sensor output, which does contain a component of gravitational acceleration as a result of the inclination angle, and thus in that respect the version that was not designed to account for the inclination angle does still take the inclination into consideration. The only difference between the vertical load estimations of the two versions comes from the effect of the inclination angle on the overall vertical load, as can be deduced from equations (7.42) and (7.43). That is, in version 2 of the algorithm the overall vertical load term in the front axle load equation is $mg\cos(\theta_e)\,l_2$ whereas in version 3 the inclination is assumed to be zero. The inclination-compensated vertical load estimation is more accurate of the two. The actual load can be seen to oscillate significantly for the first 8 seconds. The oscillation seemed to be caused by instability in the simulation; the vehicle was seen to start pitching back and forth at the start of the simulation. While the estimated values do also oscillate, their amplitudes are not as high. The real value has a significantly higher amplitude because the suspension-related pitching influences the axle loads, but the algorithm assumes the suspension to be rigid. The oscillation of the estimated front axle load values is caused by the inclination angle estimation oscillating due to the pitching.

After the TCS deactivates and the friction potential estimation ends, the potential estimated by version 2 is 0.3554 whereas version 3 shows the potential to be 0.3521. The difference is this minuscule due to the aforementioned reasons regarding the estimated longitudinal and vertical forces. The estimations are slightly higher than the defined potential of the road, which is 0.35. However, it can be seen in the friction coefficient graph that the coefficients of the front tires do actually go slightly higher than the defined potential value, reaching a peak of approximately 0.36. Nonetheless, the friction coefficient graph does show that the estimated coefficients are slightly higher than the actual coefficients of the front tires during most of the maneuver. This is likely caused by the pitching of the car, as that then causes an additional component of gravitational acceleration to be included in the longitudinal acceleration measurement of the IMU. This component is not adequately compensated for in the longitudinal and vertical force equations due to them assuming that the suspension is rigid and that the sensor output thus only consists of the actual acceleration and the gravitational acceleration component caused by the inclination angle.

The downhill braking maneuver results are shown in figure 47. The graphs for the same quantities are presented as in the uphill acceleration results, but the brake pressure is now also displayed, and the slip ratios and current friction coefficients are now presented for all four wheels. The slip ratio estimations are not shown, as they are only used by the algorithm in acceleration situations.

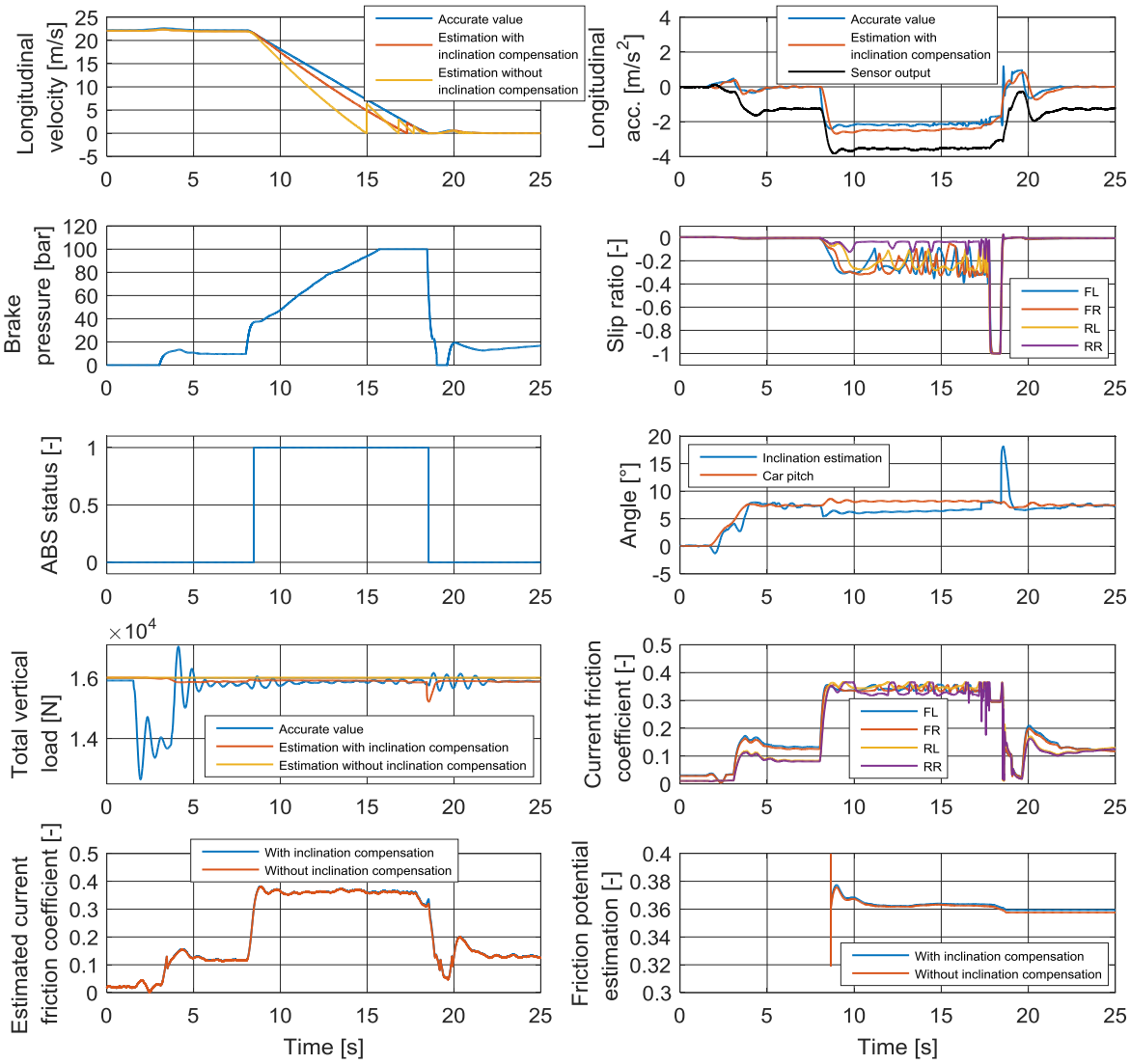

Figure 47 Simulated downhill braking maneuver results

At approximately 1.5 s, the vehicle arrives at the point where the road starts to slope downhill. The driver begins to slow the car down at 8 s, and the ABS activates almost immediately. When the heavy braking maneuver is started at 8 s, the estimated inclination angle becomes lower than the actual angle. This happens despite the car pitching slightly, which should cause the estimated inclination to show the angle as higher than it is. This phenomenon occurs due to the inclination-estimating Kalman filter waiting to switch the measurement noise covariance matrix until the specified brake pressure threshold is hit, at which point the wheel-speed-based deceleration estimation is higher than the real deceleration due to increasing wheel slip. Thus, at the point when the matrix is switched, the inclination estimation is lower than the real angle, and the filter cannot correct this offset during the heavy braking maneuver due to now primarily relying on the pitch rate. This in turn causes the inclination-compensated longitudinal deceleration estimation to be slightly higher than the actual deceleration of the vehicle. The inclination estimation is also seen to show an erroneous peak when the vehicle is about to stop. This is because the Kalman filter switches the measurement noise covariance matrix back to the default one when the velocity is not at zero yet and the wheels are locked, as the slip ratio graph shows.

During the maneuver, there is a significant difference in the two velocity estimations. As the heavy braking maneuver is started, the velocity-estimating Kalman filter switches to primarily relying on its longitudinal acceleration measurement input. As the deceleration shown by the IMU is significantly higher than the actual deceleration, the inclination-compensating algorithm version produces a much more accurate estimation of the velocity than the version that does not account for the inclination. When the deceleration is fairly constant between 9 s and 17 s, the sensor output shows the acceleration to be around -3.5 m/s^2 whereas the real deceleration is approximately -2.1 m/s^2. However, even the inclination-compensated estimation does show the velocity falling faster than the accurate value, which is due to the previously discussed inaccuracies in the inclination and longitudinal acceleration estimations. The error in the inclination-estimated acceleration is in the range of 0.25 – 0.3 m/s^2 during the braking maneuver between 9 s and 17 s. The estimated velocities are also 0.1 m/s lower that the real velocity during the first 8 seconds, which is likely due to the rolling radii of the rear tires being slightly higher than the estimated value.

There is an approximately 90 N difference between the total vertical load estimations of the two algorithm versions in the downhill section. Additionally, the inclination-compensated version has an erroneous peak at around 18.5 s that is caused by the aforementioned issue with the inclination estimation when the vehicle is about to stop. The estimations also do not follow the actual value when the vehicle is on the section of road where the inclination angle changes. This is because the vertical acceleration of the vehicle is not accounted for in the algorithm.

The minor differences in the estimated vertical loads and velocities cause there to be a small difference between the friction coefficient and potential estimations of the two versions. The inclination-compensated version shows the potential as 0.3593 after the ABS has deactivated, and the other version shows it to be 0.3575. Both values are slightly higher than the set tire-road friction potential of 0.35. However, the actual friction coefficients of the tires can be seen to reach peaks as high as 0.365. The coefficients change continuously during the braking maneuver due to the ABS trying to control the slip ratios of the wheels.

The results of the acceleration and braking maneuver performed on a level road are presented in figure 48. The figure contains the longitudinal velocity and acceleration, slip ratios, inclination estimation and CarMaker pitch angle output, TCS and ABS status, friction coefficient, and estimated friction potential graphs.

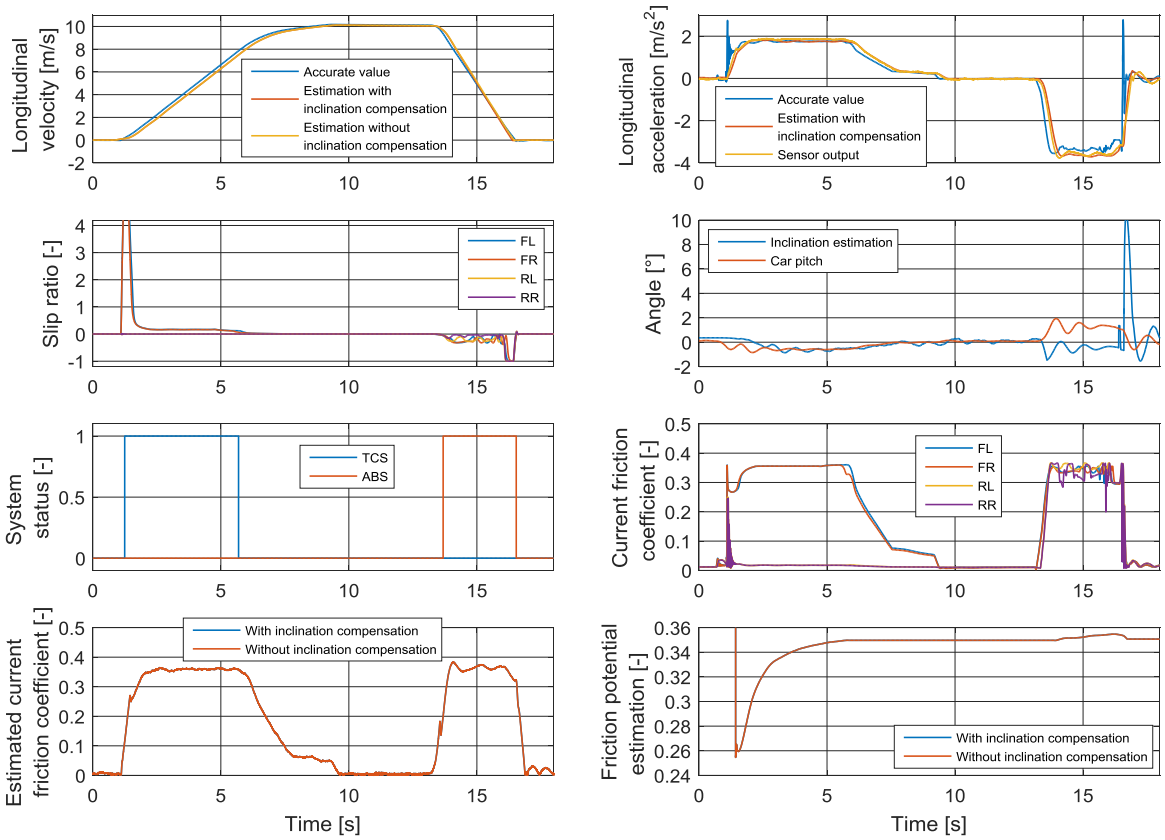

Figure 48 Simulated level road acceleration and braking maneuver results

While the traction control system does intervene early on, the slip ratios reach a high peak as the vehicle starts moving. This causes a brief peak in the longitudinal acceleration as the ratios reach the value at which the highest longitudinal force is produced and then exceed it. It seems that the effect of this peak disappears in the friction coefficient estimation due to filtering, as it cannot be seen in the coefficient estimation graph. The inclination estimation follows the pitch of the car during the acceleration, but during the heavy braking maneuver the estimation has a significant offset, which is caused by the same effect with the inclination-estimating Kalman filter as in the downhill braking maneuver. Another similarity is the brief peak seen in the inclination estimation as the vehicle is about to stop. Because of the inaccuracy in the inclination estimation, the deceleration during the braking maneuver is estimated as slightly higher than the real value with the difference varying between 0.2 and 0.4 m/s^2, which also then influences the velocity estimation. The difference in the friction coefficient and potential estimations between the two algorithm versions is marginal. After the acceleration maneuver they show the potential to be 0.3497. Once the ABS has deactivated, the value is at 0.3507. Because the ABS activates less than 10 seconds after the TCS deactivated, the coefficient data saved during the acceleration maneuver is combined with the data measured during braking, meaning that the potential is calculated as the average of all the recorded data while the ABS is active.

The results of the cornering maneuver that was done in a banked downhill corner are displayed in figure 49. All three versions of the algorithm are compared in these graphs. The car roll angle output of CarMaker is the sum of the bank angle of the road and the roll angle of the body relative to the road, which is caused by lateral load transfers affecting the suspension.

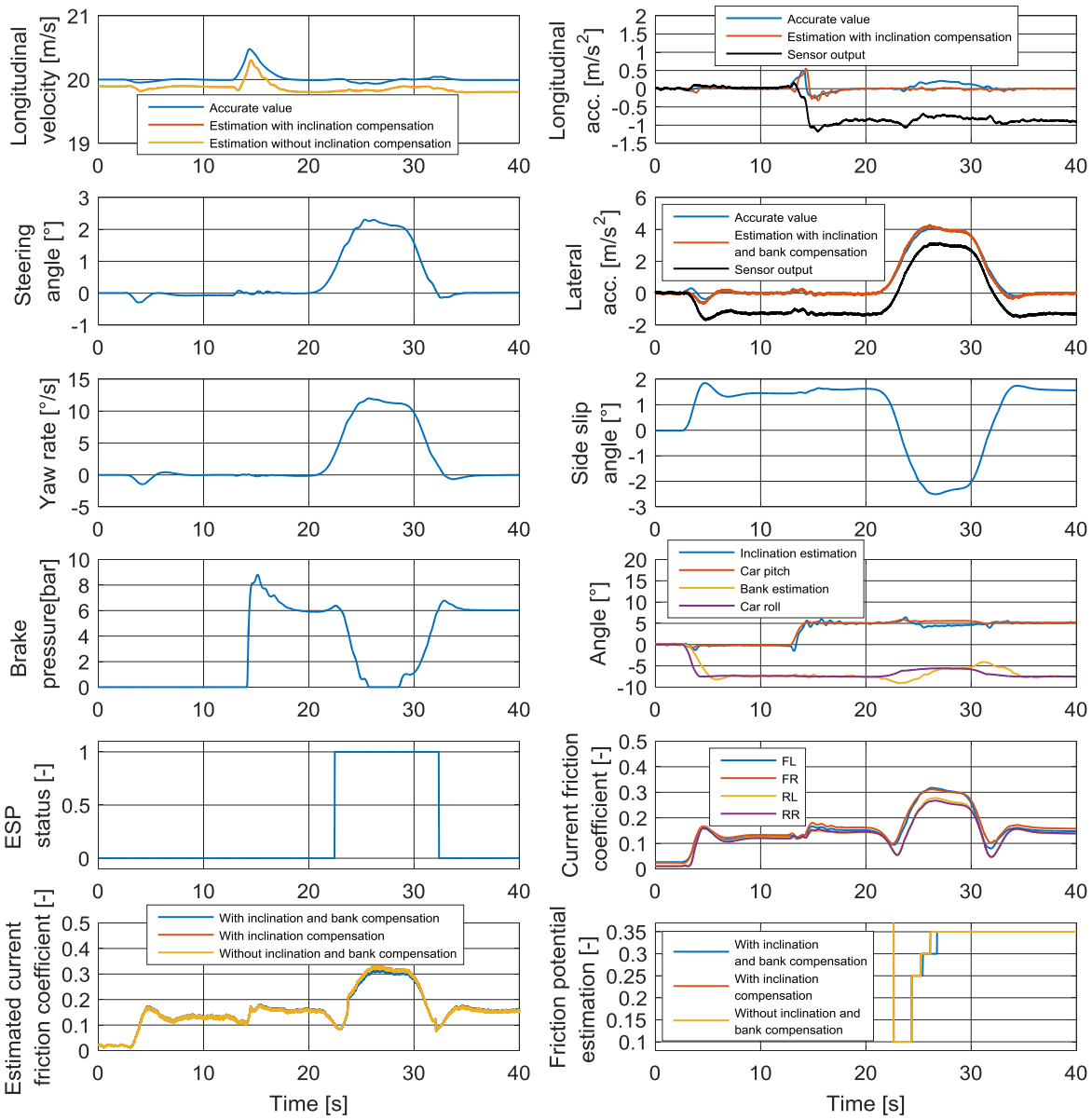

Figure 49 Downhill banked turn cornering maneuver results

The road starts to become banked at approximately 3 s and then inclined at 13 s. The bank angle of the road is -7 degrees and the inclination is 5 degrees. The driver begins to apply the brakes lightly in the inclined part in order to maintain the velocity stable at 20 m/s. The vehicle enters the corner at around the 21-second mark. The inclination and bank estimations accurately reflect the pitch and roll outputs of CarMaker until the cornering maneuver begins. At that point, the bank estimation shows the bank to increase even though the body actually rolls in the opposite direction due to lateral load transfer. The bank estimation peaks at approximately -9 degrees during the beginning of the cornering maneuver. At the same time, the inclination estimation falls slightly such that it is approximately 1 degree below the pitch output of CarMaker (4.5 ° vs 5.5 °) throughout the maneuver. Towards the end of the turn, starting at approximately 30 s, the bank estimation starts to erroneously show the absolute value of the bank angle as reducing with the value going as low as 4.1 °. Error in

the bank angle estimation adversely influences the vertical load calculations, which in turn affects the accuracy of the friction estimation.

These errors in the bank and inclination estimation can be explained by changes in the side slip angle of the CoG. As the vehicle begins cornering, the side slip angle starts to become negative, reaching a negative peak of -2.5 degrees at 26.5 s. A negative side slip angle means that the CoG has lateral velocity to the right. Thus, the vehicle is oversteering in this left-hand turn. Changes in the lateral velocity influence the lateral acceleration measurements because the measured acceleration then also contains the time derivative of the lateral velocity. When the velocity starts to become more negative at the 21 s mark, it has a reducing effect on the lateral acceleration as well, as equation (3.4) shows. This in turn causes the bank estimation to become more negative because the difference between the measured lateral acceleration and the multiplication of the longitudinal velocity and the yaw rate increases. Once the side slip angle reaches its negative peak at approximately 26.5 s and becomes more stable for a few seconds, the estimated bank angle also returns to being nearly equal with the roll output of CarMaker. The lateral velocity starts to become more positive again at approximately 30 s, which causes the bank estimation to swing erroneously in the other direction.

When the CoG has side slip angle during cornering, the longitudinal acceleration is affected by the angle as it then contains a component of the centripetal acceleration of the vehicle. This is why the measured and the real longitudinal accelerations increase slightly when the vehicle starts cornering. The difference between the measured acceleration and the wheel-speed-based acceleration estimation reduces because of this, which in turn causes the estimated inclination angle to erroneously decrease. The inclination-compensated acceleration measurement does not show the centripetal acceleration component because it gets erroneously compensated due to the aforementioned error in the inclination estimation. The estimated longitudinal velocities have a slight error offset again compared to the actual velocity, likely caused by the dynamic rolling radii of the tires not being equal to the estimated value. This will cause a tiny error in the drag force calculations. Furthermore, when the side slip angle is non-zero, an aerodynamic side force and a resulting yaw moment affect the car [77]. However, these effects have been neglected in the estimation algorithm, as it assumes the side slip angle of the CoG to always be zero.

Despite these issues, it can be seen that the version of the algorithm that accounts for both the inclination and the bank estimates the current friction coefficient slightly more accurately during the cornering maneuver than the other two versions. The actual coefficients of the front tires peak at approximately 0.315, which is also the peak that version 1 of the algorithm shows. The other two versions show the peak to be at approximately 0.33. The friction potential estimation is triggered by the ESP in this maneuver. As a result of that, there is little difference between the estimations of the three versions due to the low resolution of the ESP-based potential estimation, and they all show the same value (0.35) after the ESP has deactivated.

The double lane change maneuver results are presented in figure 50. Versions 1 and 2 of the algorithm are compared in these result graphs.

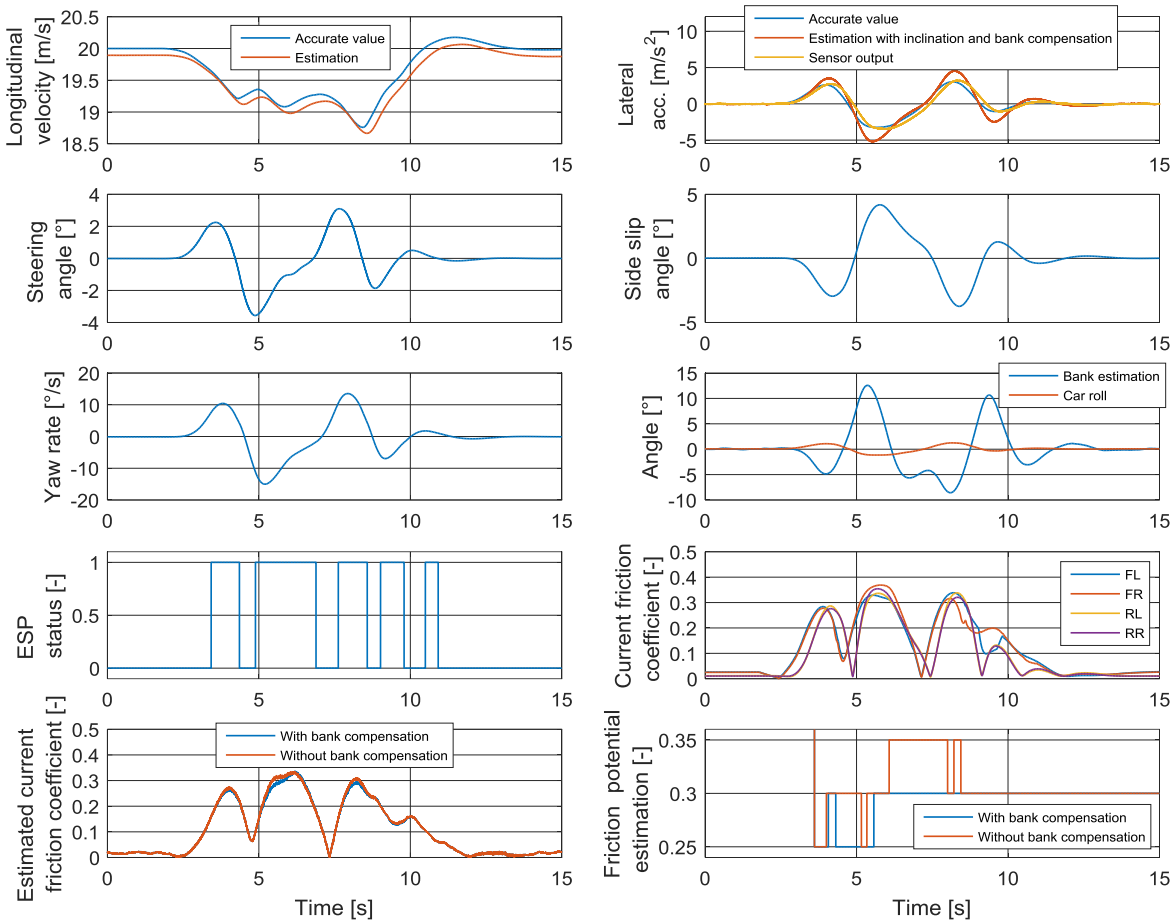

Figure 50 Double lane change maneuver results

The absolute value of the side slip angle reaches even higher values in this maneuver than in the previous one. When the vehicle is first turned to the left, the side slip angle becomes negative. Then, the angle becomes positive when the driver steers to the right, and finally it becomes negative again as the driver steers left to go through the final set of cones. Thus, the vehicle oversteers throughout the entire maneuver. Similar to the previous maneuver, the time derivative of the lateral velocity of the CoG affects the lateral acceleration and causes the bank estimation to go wrong. The bank angle estimation exceeds 12 degrees at 5.5 s, while the body roll angle never even exceeds 1.25 degrees. Additionally, the bank angle estimation has the opposite sign compared to the roll angle for most of the duration of the maneuver. This is caused by the sign of the time derivative of the lateral velocity being opposite to the sign of the multiplication of the yaw rate and the longitudinal velocity. This phenomenon is the same that appeared in the results of the previous maneuver, but this time it is more drastic due to the side slip angle varying more rapidly. The error in the bank estimation causes the bank-compensated lateral acceleration estimation to also contain error. These errors should then affect the vertical load estimation, which in turn affects the friction coefficient and potential estimations. The errors appear to largely cancel each other out, however, as can be seen in the graph depicting the estimated current friction coefficients. The differences between the estimations of the two algorithm versions are small. The coefficients estimated by both versions peak at approximately 0.33 at 6.2 s. At that point, the actual coefficients of the front right and front left tire are 0.36 and 0.32.

The ESP activates multiple times in succession to combat oversteer. As the time gap between it deactivating and then reactivating never exceeds 10 seconds, the histogram used for calculating the friction potential is plotted for all of the saved friction coefficient data points throughout the whole maneuver. Both algorithm versions show the potential as 0.3 after the ESP deactivates for the final time.

Results of the start maneuver performed with the wheel turned 360 degrees to the left are displayed in figure 51. The longitudinal and lateral force plots are presented along with the actual forces produced by the front tires so that the functionality of the modified single-track model can be assessed.

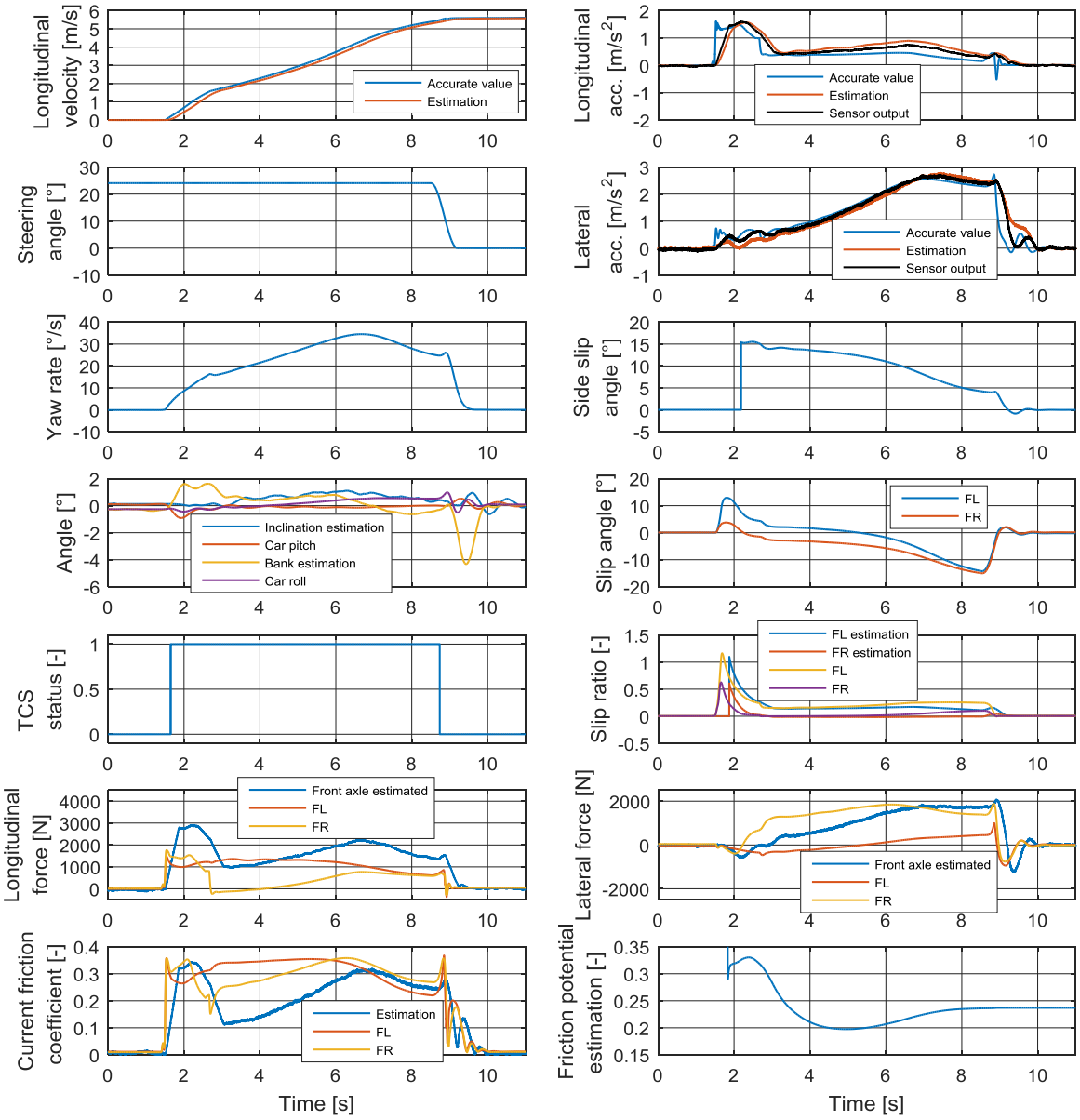

Figure 51 Results of the simulated start maneuver with high steering angle

The side slip angle shows that the vehicle understeers significantly during the maneuver. When the car first starts moving at 2.2 s, the side slip angle is 15.4 degrees. Additionally, the slip angle of the left front wheel is positive until the 5 s mark. The slip angle of the right

front wheel is also positive for the first half a second after the car starts to move but then turns negative. This results in the front tires producing lateral force in opposite directions. The left front wheel produces a force that opposes the rotation of the vehicle. However, the absolute value of the lateral force produced by the right front wheel is much higher.

The longitudinal forces also help significantly with rotating the vehicle during the maneuver. During the first half a second of the car moving, the longitudinal forces are rotating the vehicle while the lateral forces object the rotation. The longitudinal force graph shows that the longitudinal force produced by the right front tire falls drastically at 2.65 s as its slip ratio drops close to zero. The force even becomes negative for a couple of seconds. This drop may be caused by the traction control system.

The pitch angle of the vehicle is marginal throughout the maneuver. However, the estimated inclination erroneously shows the inclination to be in the range of 0.5 – 1.1 ° between 3 s and 9 s, meaning that the wheel-speed-based acceleration estimation is slightly higher during that period than the measured longitudinal acceleration. This also causes error in the longitudinal acceleration estimation. The bank angle estimation also contains some error. When the car starts moving, the estimation jumps to 1.6 ° while the actual roll angle of the vehicle is slightly negative. The estimation also has a negative peak of -4.3 ° at 9.4 s. These issues may be caused by the side slip angle and its time derivative.

The single-track model considers the tires on each axle as one single unit. Thus, the calculated front axle longitudinal and lateral forces should be equal to the combination of the forces produced by both tires. The estimated front axle longitudinal force appears to be close to the sum of the longitudinal forces produced by the front tires although it is slightly too high between 6 s and 8.5 s. This is likely due to the measured longitudinal acceleration being too high. The estimated front axle lateral force appears to be slightly too low throughout most of the maneuver and particularly during the period between 2.5 s and 7.5 s.

The estimated current friction coefficient appears to be relatively accurate during the first second of the vehicle moving. However, it then falls to 0.1 at 3 s even though the left front coefficient is still at 0.25 and the right front coefficient at 0.34. While this issue is in part due to the front axle lateral force estimation being lower than the sum of the actual lateral forces produced by each front tire, it is compounded by the fact that one of the tires uses its friction potential almost entirely to produce longitudinal force and the other to produce lateral force. The single-track model senses the friction coefficient as:

$$\mu_e = \sqrt{\mu_{x1} + \mu_{y1}} = \sqrt{\left(\frac{F_{x1,3} + F_{x1,4}}{F_{z1}}\right)^2 + \left(\frac{F_{y1,3} + F_{y1,4}}{F_{z1}}\right)^2} \tag{8.1}$$

where $F_{x1,3}$, $F_{x1,4}$, $F_{y1,3}$, and $F_{y1,4}$ are the longitudinal and lateral forces produced by the left front and right front tire. If one front tire produces only longitudinal force and the other only lateral force, and the coefficient of each tire is equal to the potential, the equation can then be written as:

$$\mu_e = \sqrt{\left(\frac{\mu_{pot}}{2}\right)^2 + \left(\frac{\mu_{pot}}{2}\right)^2} = \frac{\mu_{pot}}{\sqrt{2}} \tag{8.2}$$

assuming that there are no lateral load transfers. This shows that even though both front tires are using the entire friction potential in this situation, the coefficient that the single-track model acquires is equal to the potential divided by $\sqrt{2}$. Equation (8.1) indicates that the smaller the angle between the overall forces produced by the left front and right front tire is, the closer the calculated friction coefficient is to the average of the friction coefficients of the two tires. As the angle increases, the calculated value reduces. As the force graphs show, the angle between the overall forces produced by the front tires is large from 2.5 s onwards, which causes significant error in the estimated friction coefficient. The estimated potential is 0.2369 after the TCS deactivates, which is 0.1131 lower than the actual potential of 0.35.

9.1.2 Effect of Varying Friction Potential

The results of the varying friction potential tests are presented in figure 52. The graph features three friction potential vs friction strip length plots. The friction potential was taken as the value that the algorithm was showing at the end of each maneuver. The blue plot represents the situation where the front tires of the vehicle are on the higher friction surface at start. The red plot depicts the front tires being on the lower friction surface at the start, and the yellow plot is the average of the two.

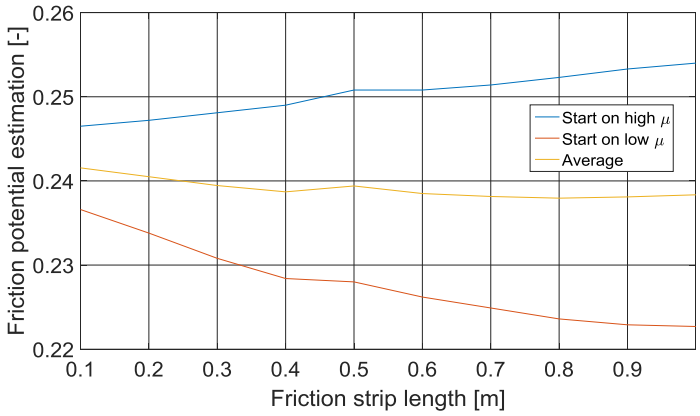

Figure 52 Varying friction potential simulation results

As the figure clearly demonstrates, the surface that the tires are on at the start influences the potential estimation significantly. When the tires are on the higher friction surface at the start, the potential estimation increases as the friction strip length increases. The opposite happens when the tires are on the lower friction surface when the vehicle starts to move. The average of the two changes only slightly when the friction strip length changes. The reason behind these results is that the vehicle spends more time on the first strip than any of the other ones, as its velocity keeps increasing and the strips are crossed faster and faster. Because the potential is calculated as the average over time rather than distance, the friction coefficient measured during the first strip is weighted the most in calculating the potential. If the tires are on the lower friction surface at the start, the vehicle will spend a higher amount of time on the first strip, and it will be emphasized even more. The longer the strip length is, the more time the vehicle spends on the first strip. This is why the estimated potential increases when the strip length increases in the high-friction situation, and the opposite happens in the low-friction situation. The estimation is closest to the actual average friction potential of the road (0.25) in these tests when the tires are on the high-friction surface at the start and the strip length is 0.4 – 0.6 m. The effect that the surface the tires are on at the start has on the acceleration and the friction estimation is demonstrated in figure 53.

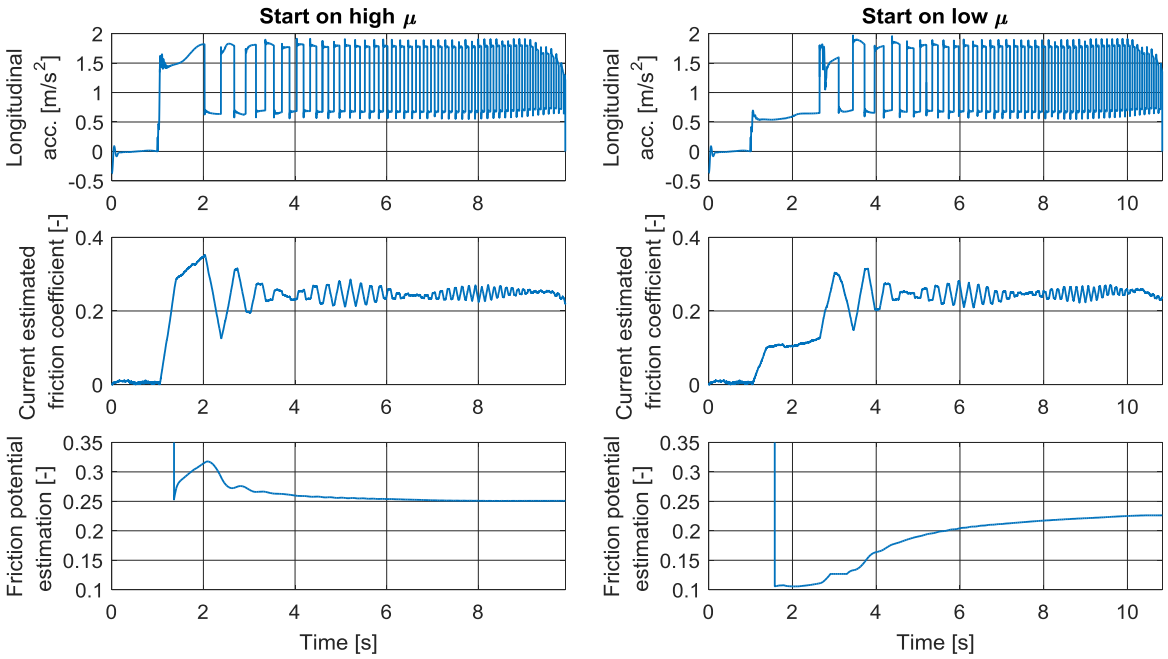

Figure 53 Varying friction potential results with a friction strip length of 0.6 m

The acceleration graphs show that the acceleration varies based on the surface the front tires are on. The frequency of the variation increases as the maneuver progresses due to the velocity increasing. When the tires are on the high-friction surface at the start, the acceleration reaches 1.5 m/s^2 immediately as the vehicle starts moving whereas on the low-μ surface the acceleration barely exceeds 0.5 m/s^2. It can also be seen from these acceleration graphs that in the high-μ run the vehicle spends approximately 0.5 s on the first strip. In contrast, in the low-μ version it spends almost a second on the first strip. The friction estimation graphs reflect these differences. The estimations also show the variance of the friction coefficient although it appears that the amplitudes are reduced due to the filtering in the algorithm. The friction potential begins at a high value in the high-friction maneuver and then descends as the maneuver progresses whereas the opposite occurs with the low-μ run. The potential is estimated as 0.2508 and 0.2262 at the end of the high-μ and low-μ tests.

9.1.3 Effect of Varying Location of Center of Gravity

The results of the simulations that were run in order to investigate the effect of the location of the center of gravity on the accuracy of the friction potential estimation are shown in figure 54. The friction potential shown by the algorithm at the end of each maneuver is plotted as a function of the front axle weight percentage in the graph.

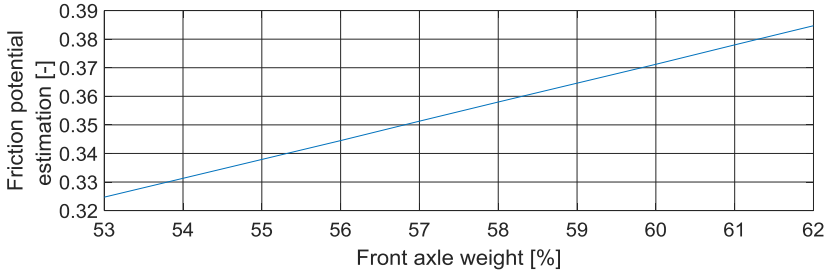

Figure 54 Varying location of CoG simulation results

The graph clearly shows that the relationship between the longitudinal weight distribution and the estimated friction potential is linear. This result is due to the fact that the longitudinal force estimation is not affected by the longitudinal weight distribution of the vehicle, as can be seen from equation (7.66). However, as equation (7.40) shows, the vertical load of the front axle is linearly dependent on the longitudinal distance l_2 between the CoG and the rear axle, which in turn is linearly dependent on the front axle weight percentage. Thus, when the longitudinal weight distribution changes but the algorithm assumes it to be constant, the friction estimation changes linearly with the percentage.

9.2 Road Test Results

The results of the tests that were conducted with the research vehicle and sensor equipment are presented and discussed in this section. The longitudinal velocity measured by the Correvit optical sensor that shows up in the graphs has been corrected with the yaw rate according to equation (5.1). Similarly, the side slip angle has been calculated based on the longitudinal and lateral velocities that have been corrected to the CoG according to equations (5.1) and (5.2). The tire-road forces measured by the wheel-integrated force transducer system that are also presented in the graphs have been filtered with a moving average filter. The friction coefficient of the right front wheel, which serves as a comparison point for the estimated coefficients, has been calculated based on the measured tire forces using equation (3.13).

The uphill acceleration maneuver results are presented in figure 55. Same quantities are displayed as in figure 46. In the case of the uphill acceleration, downhill braking, and level road acceleration and braking maneuvers, versions 2 and 3 of the algorithm are compared.

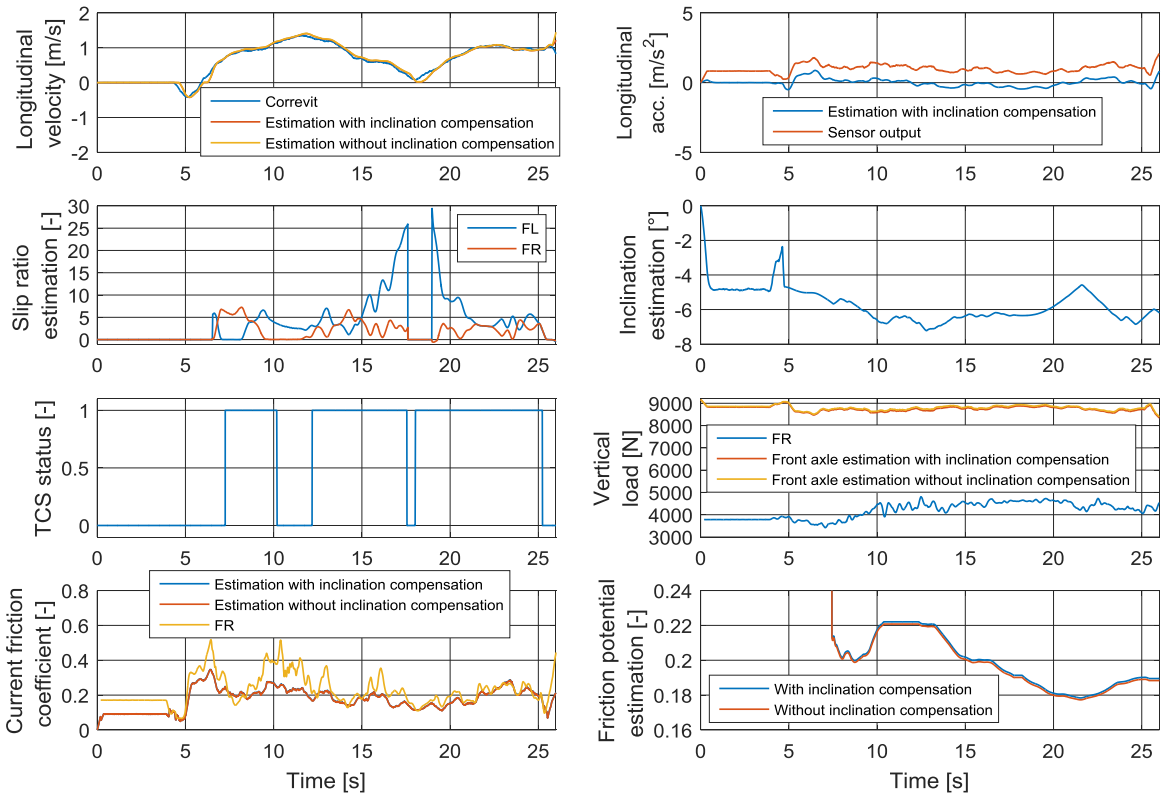

Figure 55 Uphill acceleration maneuver results

Like in the simulated uphill acceleration maneuver, the traction control system is on for most of the duration of the maneuver. However, it does not activate as soon as it did in the simulated maneuvers, and thus the friction potential estimation is initially triggered by the estimated slip ratios. The TCS activates when the velocity is approximately 2.5 km/h. The estimated velocity appears to be relatively accurate, which was the case in the simulated maneuver as well. The hill was slippery at the time of the test. Even though the inclination is not as steep as the simulated uphill, the vehicle struggled to get going. It can be seen in the results that the acceleration never exceeds 1 m/s^2 and the velocity only reaches a peak of approximately 1.4 m/s. The slip ratios get much higher than they did in the simulations. This indicates that the traction control system of the real vehicle does not intervene as aggressively as its simulated counterpart.

The inclination estimation appears show values in the correct range as well. As mentioned before, the inclination angle of the hill was measured to vary between 4.5 and 6 degrees. The estimation does show the inclination to reach over 7 degrees at times, but this may be due to the body pitching because of the acceleration and the inclination.

As was the case with the simulated maneuver, the inclination-compensated front axle vertical load is slightly lower than the non-compensated estimation. The difference is around 50 N in this case. This causes a small difference between the two algorithm versions in the friction coefficient and potential estimations. It can be seen that the measured friction coefficient is markedly higher than the estimated values during the beginning of the maneuver. The estimated and measured values reach their peak at 6.45 s with the measured one being 0.52 and the estimated ones being 0.35. The gap then reduces between 10 s and 15 s.

The measured vertical force is lower at the start of the maneuver than it would be expected to be. The value then increases in the period between 7 s and 10 s to a more reasonable level. This effect was likely caused by the force transducer system. It was seen that when the vehicle is stopped, there may be some tensions left in the wheel, which then cause the measured forces to be erroneous. In this case, part of the vertical load appeared to show up in the longitudinal force measurement. The vehicle needs to travel a small distance for these errors to disappear. The measured longitudinal force being slightly too high and the vertical load too low explains the gap between the measured and estimated coefficients during the beginning of the maneuver.

At the end of the maneuver, the inclination-compensated algorithm shows the friction potential as 0.1895 whereas the non-compensated version shows it as 0.1883. This difference is slightly smaller than it was in the simulated maneuver, which can at least partly be explained by the more gently sloping hill. Nonetheless, the differences between the friction estimations of the two algorithm versions are marginal in both cases.

The results of the downhill braking maneuver, which was conducted in the same hill as the previous maneuver, are shown in figure 56. The longitudinal velocity and acceleration, brake pressure, inclination estimation, ABS status, measured right front tire forces, estimated and measured friction coefficients, and estimated friction potential are displayed in the figure.

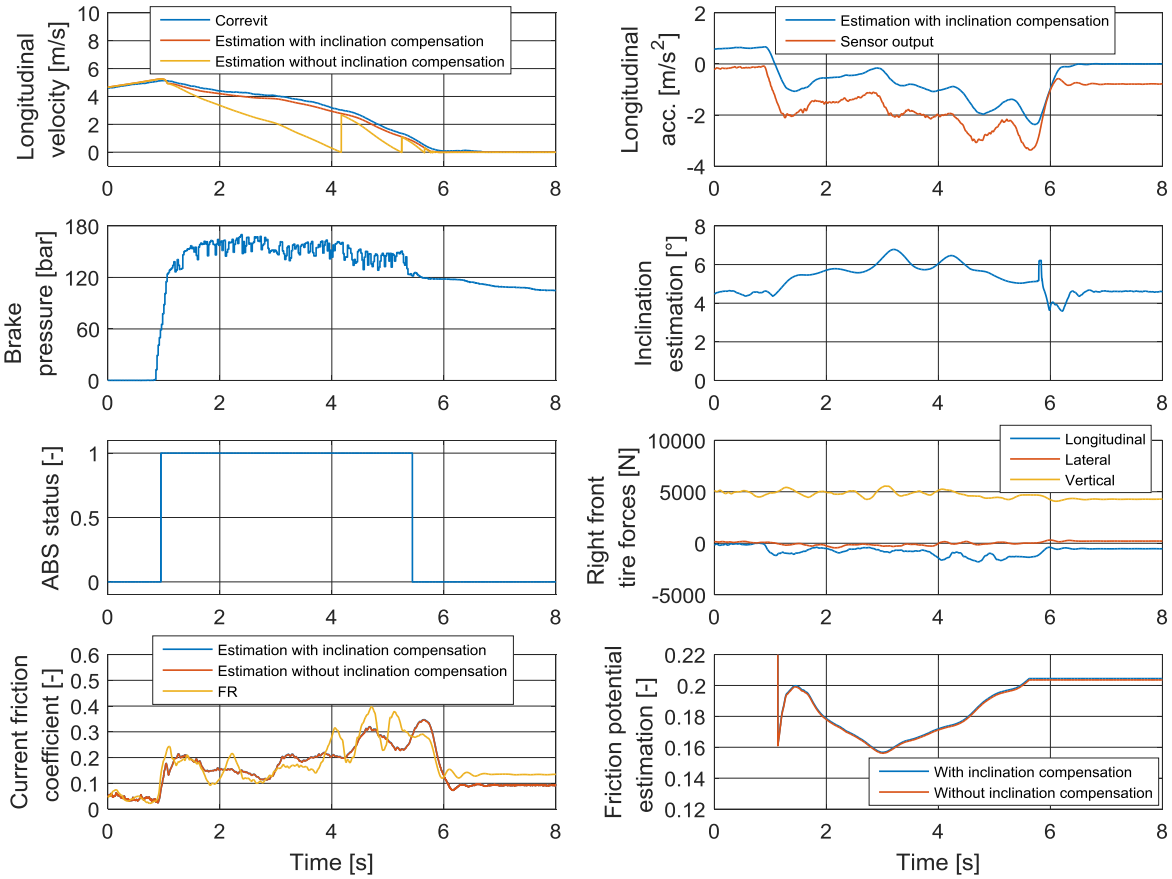

Figure 56 Downhill braking maneuver results

Similar to the simulated downhill braking maneuver, the inclination-compensated velocity estimation is much more accurate than the non-compensated one. This happens because the velocity-estimating Kalman filter switches the measurement noise covariance matrix and starts to rely mostly on its acceleration measurement input. The sensor output shows the deceleration as too high due to the downhill, which then causes the non-compensated velocity estimation to have significant error.

The inclination estimation appears to yield values in the correct range again. It does seem to show the downhill as slightly steeper than it is during the braking maneuver, which is likely a result of the car pitching. Unlike in the simulated maneuver, the estimated angle does not fall this time when the braking maneuver is started. This disparity is likely caused by differences between the braking systems of the simulated and the real vehicle. If the real vehicle requires a higher brake pressure in order to produce the same braking forces, the braking forces are lower and there is likely less slip when the brake pressure threshold where the inclination-estimating Kalman filter switches its measurement noise covariance matrix is reached. Consequently, the inclination estimation obtained by comparing the acceleration sensor output and the wheel-speed-based acceleration estimate contains less error when the matrix is switched. In other words, an offset is not caused in the inclination angle estimated by the Kalman filter in this case because the matrix is switched before the sensor-and-wheel-speed-based estimation becomes notably erroneous due to increasing wheel slips.

Still, the differences between the friction estimations of the two versions are minuscule, just like they were in the simulated downhill braking maneuver. The inclination-compensated version shows the friction potential to be 0.2044 after the ABS has deactivated and the non-compensated versions shows it as 0.2036. These values are close to the values obtained from the uphill acceleration maneuver in the same hill. The coefficient estimations can be seen to match the measured coefficient rather well although the measured value seems to oscillate more. The oscillation is likely due to the interference of the ABS.

Based on the results of the two presented maneuvers, it would appear that the friction potential in the hill was erratic; it seems to have varied between 0.1 and 0.4. This seems plausible, as the hill was covered inconsistently in ice, snow, and gravel.

The results of the acceleration and braking maneuver that was performed on a relatively level bit of road are displayed in figure 57. The same quantities are presented as for the previous maneuver.

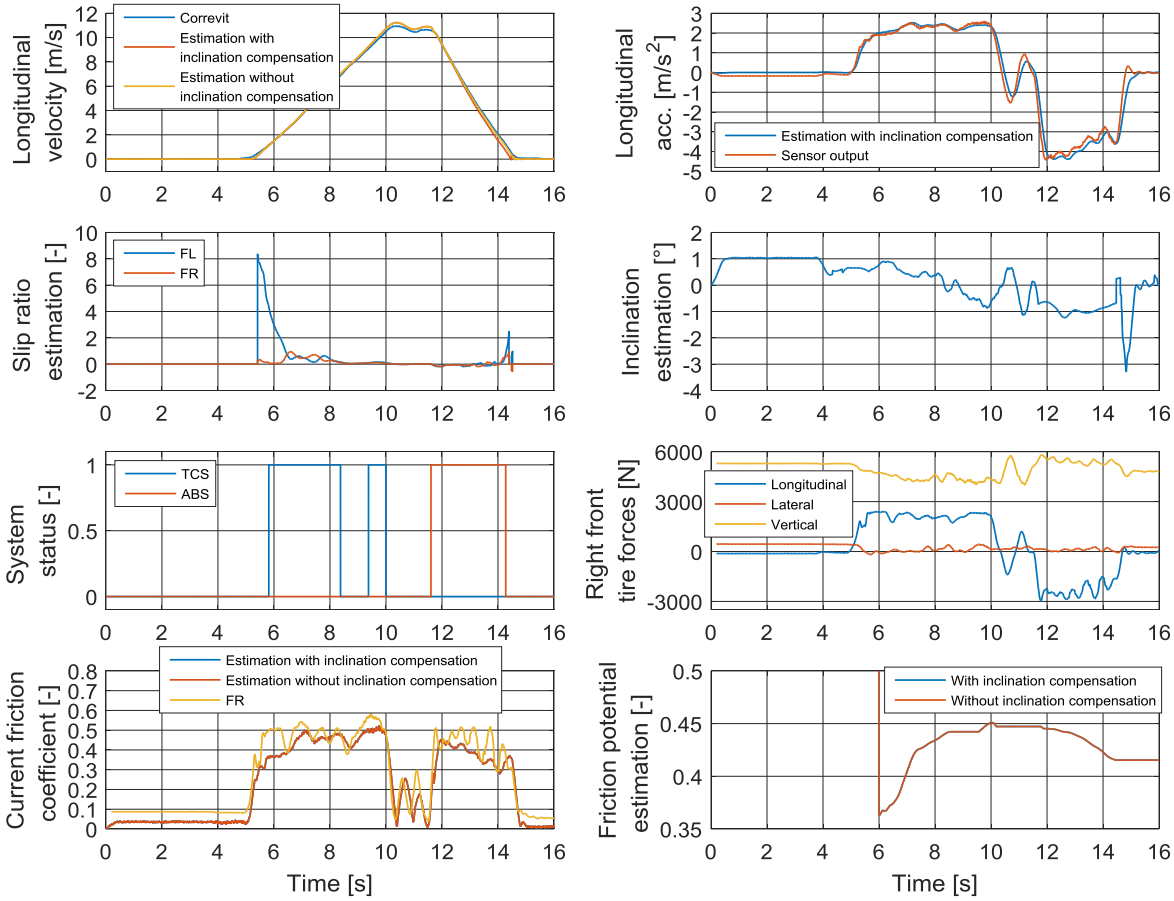

Figure 57 Level road acceleration and braking maneuver results

While the inclination estimation showed a slight uphill due to the pitch of the vehicle in the simulated version of this maneuver, in this case the estimation actually shows a slight downhill until 8.3 s. After that point, the estimation shows a slight degree of uphill. The downhill part does reflect the elevation changes of the road that were described in section 8.2, but the uphill does not. The inclination estimation was negative also during the braking phase of the simulated version of this maneuver. In that case it was due to the same issue

with the matrix switching of the inclination-estimating Kalman filter that was discussed when examining the results of the previous maneuver. That may be the cause in this case as well. The inclination estimation also features a peak right when the vehicle stops. The direction of the peak is opposite to that of the peaks in the estimation in the simulated braking maneuvers. It seems to occur as the inclination-estimating Kalman filter switches the measurement noise covariance matrix back to the default one but the velocity is not yet at zero. A negative peak could be explained by the wheel in the process of locking up as the matrix is switched, as the wheel-speed-based deceleration would then be higher than the measured deceleration.

It can be seen that the estimated velocities are higher than the measured velocity by approximately 0.1 – 0.2 m/s during the periods of acceleration and relatively stable speed between 5 s and 11.5 s. This would imply that the rolling radii of the rear tires are actually smaller than the estimated radius, which is the opposite of what the case tended to be with the simulations. However, the difference is still small. When the braking is started, the inclination-compensated velocity estimation starts to fall more rapidly than the real velocity. The non-compensated velocity matches the real value more closely. This means that the inclination-compensated deceleration is too high, and thus the estimated inclination has error. This same effect occurred in the simulated maneuver.

The slip ratios cause the friction potential estimation to be triggered before the TCS intervenes. It can be seen that the slip ratio of the left front wheel reaches an estimated peak of 8.34 when the vehicle starts to move, while the slip ratio of the right front peaks at 0.94. While this could be due to the left front tire being on a more slippery surface, it is likely that it is caused by the unequal inertias of the front wheels. The inertia of the right front is higher than that of the other wheels due to the wheel-integrated force transducer system. It appears that the differential and the TCS of the vehicle are not able to properly cope with this difference. The longitudinal force produced by the left front wheel is limited during the period that it has such a high slip ratio. Thus, the estimated friction coefficient is lower than the coefficient measured from the right front wheel during the period between 5.5 s and 6.5 s. After that, the measured and estimated coefficients are more equal. The measured value is a bit higher during the braking maneuver although it oscillates again. It may be that the right side tires were on a surface that had slightly more grip during the deceleration. The oscillation is caused by the ABS, as the slip ratios can be seen to vary a lot during the braking phase. The slip ratio estimations are relatively unreliable during heavy braking, though, due to the inaccuracy of the velocity estimation, which also causes the peaks in the estimated ratios when the vehicle is about to stop.

Just like in the simulated maneuver, there is practically no difference between the friction estimations of the two algorithm versions. Both versions show the potential to be 0.447 after the acceleration maneuver. After the ABS has deactivated, they show the potential as 0.4153.

The results of the corner acceleration maneuver are presented in figure 58. The longitudinal velocity and acceleration, steering angle, lateral acceleration, yaw rate, side slip angle, estimated slip ratios of the front wheels, inclination and bank estimations, TCS status, right front tire forces, estimated and measured friction coefficients, and estimated friction potential are displayed in the graphs. Versions 1 and 2 of the algorithm are compared.

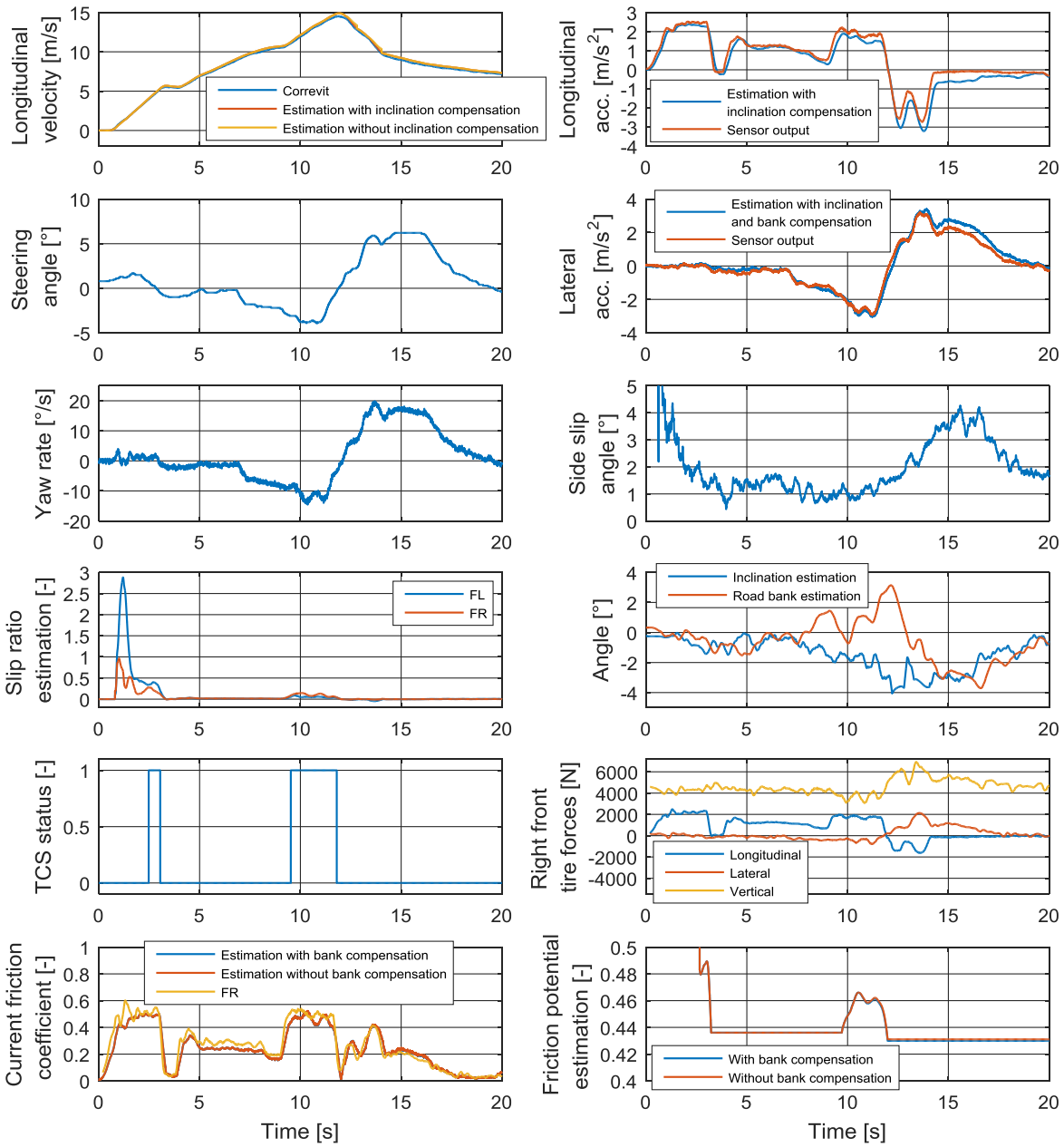

Figure 58 Acceleration during cornering maneuver results

As was the case in the previous maneuvers, the slip ratios initially trigger the friction potential estimation because the TCS does not activate immediately after the vehicle starts moving. It can be seen that, like in the previous test, the slip ratio of the left front wheel has a much higher peak than the slip ratio of the right front. This happens likely for the same reason as before, which is the increased inertia of the right front wheel. The friction potential is estimated as 0.436 by both of the algorithm versions after the initial acceleration.

The vehicle then enters the right-hand corner at approximately 7 s, and an aggressive acceleration maneuver is started at 10.5 s, forcing the TCS to intervene. After the acceleration, a left-hand turn is taken. The inclination estimation appears to roughly agree with the measured values. The road slopes slightly upwards with the highest measured inclination being 4 degrees. It can be seen that the absolute value of the estimated inclination

does increase a bit when the vehicle is accelerated in the corner. This increase may be caused in part by the body pitch angle changing due to the acceleration. The estimated bank angle also seems to agree with the measured angles. As was mentioned in section 8.2, the corners were slightly banked such that the road descended towards the inside of the turn in both corners. The highest estimated bank angle during the right-hand corner is approximately 3.1 degrees, and the angle then falls as low as -3.7 degrees during the left-hander. The side slip angle may have a minor effect on the bank and inclination estimations, but the angle stays fairly low, barely exceeding 4 degrees at its peak, and does not change rapidly during the maneuver, so the time derivative of the lateral velocity is small.

During the acceleration in the corner, the bank-compensated lateral acceleration exceeds 3 m/s^2 and the inclination-compensated longitudinal acceleration reaches 1.9 m/s^2. Both of them have an approximately 0.2 m/s^2 difference compared to the respective sensor output during the moments of highest acceleration between 9 s and 11.5 s. The estimated friction coefficients are close to the measured value during the corner acceleration. The bank-compensated estimation reaches a peak of 0.5213, and the non-compensated value peaks at 0.5234. The peak of the measured coefficient is at 0.53 during that period. After the TCS deactivates for the second time, the inclination-compensated friction potential is at 0.4299, and the non-compensated value is at 0.4311. The TCS appears to stay on for a small amount of time even after the slip ratios have fallen close to zero after the corner acceleration. This causes the friction potential estimation to fall unnecessarily. It may be that the TCS status signal in the CAN bus of the vehicle has slight delay.

The results of the start maneuver with high steering angle are shown in figure 59. Version 1 of the algorithm is used for the estimation.

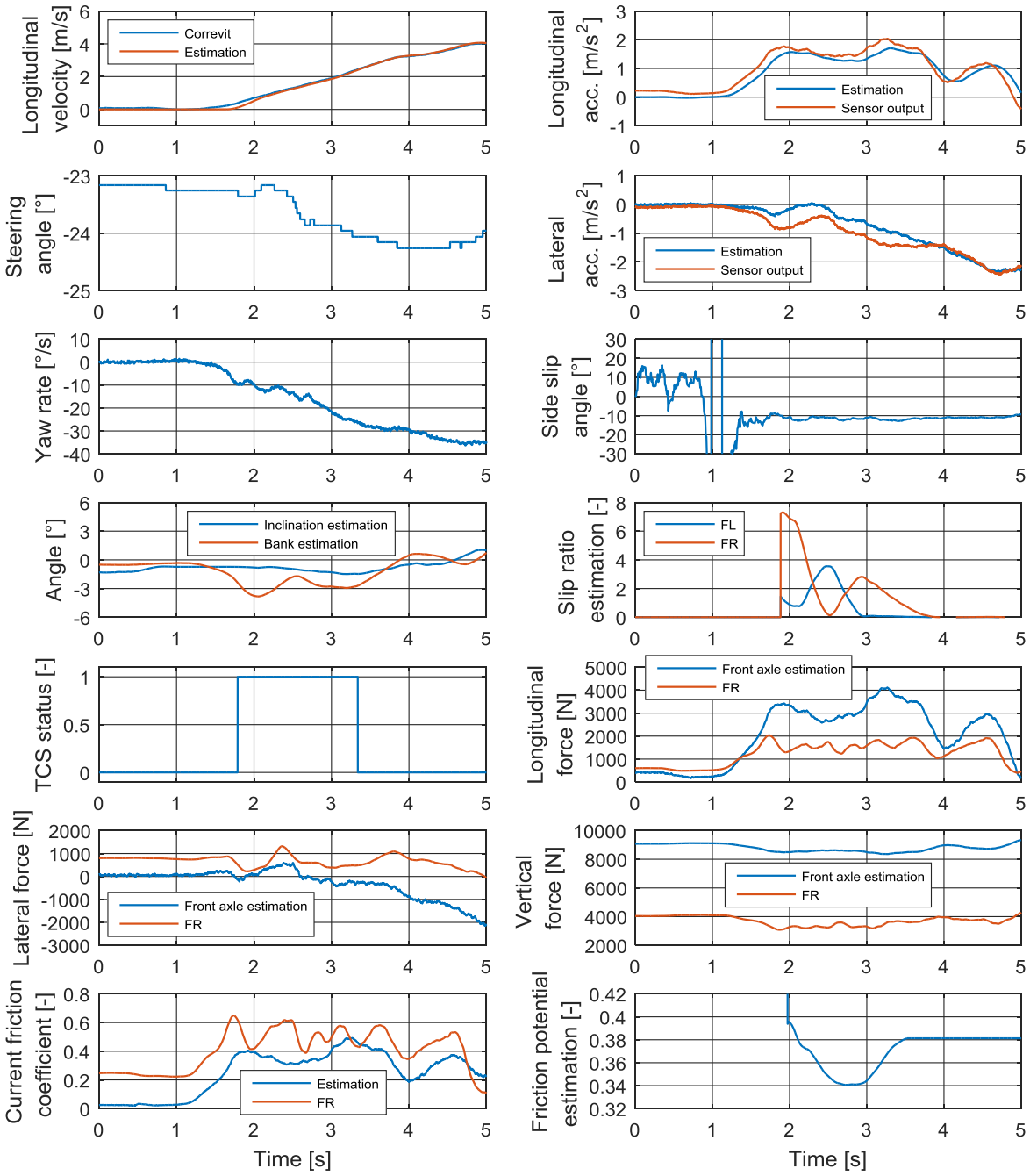

Figure 59 Results of the start maneuver with high steering angle

Much like in the simulated version of the maneuver, the vehicle is seen to understeer. The side slip angle is around -10 degrees throughout the maneuver. The angle appears to be erroneous until the vehicle starts moving, as it should be zero until then. The error in the bank angle estimation is also similar to that in the simulated maneuver. Another similarity to the simulation is that the inside front wheel, which in this case is the right front, produces a lateral force that opposes the rotation of the vehicle. As was discussed when examining the results of the simulated maneuver, this significantly compromises the friction estimation. The lateral force is high even before the vehicle starts moving. This is likely due to tensions in the wheel causing the force transducer to show erroneous values. It can also be seen in the vertical force graph that the wheel load of the right front tire is significantly lower than half

of the front axle load, even when the velocity is zero. The lateral load transfer is likely caused by the front suspension geometry. The cambers change due to the caster angle when the wheels are turned. If the caster angle is positive, the camber angle of the outer front wheel becomes more negative, and the angle of the inner front wheel becomes more positive. [23] This causes the body to tilt, which in turn causes load to shift laterally onto the outer wheels. Lateral load transfers further compromise the friction estimation due to load sensitivity changing the friction potentials of the tires.

Similar to the simulated maneuver, the estimated friction coefficient is markedly lower than the measured coefficient throughout most of the maneuver. The gap between the two values appears to range from 0 to slightly over 0.2. The measured value peaks at 0.65, while the estimated coefficient reaches a peak of 0.4912. The friction potential estimation shows a value of 0.3813 after the estimation has ended.

9.3 Error Analysis of the Algorithm

The error sources are summarized in this section. The results show that the algorithm is capable of estimating the friction potential with a high degree of accuracy in acceleration and braking maneuvers on both inclined and level roads. In the simulations, the estimated potential is within 0.01 of the actual potential. The slight amount of error is caused by the algorithm disregarding the effects of the suspension. The body pitches during acceleration and braking due to the suspension, which influences the component of gravitational acceleration that the acceleration measurements contain. The measurements are used to calculate the tire-road forces in the algorithm with the assumption that the gravitational acceleration component they contain is only caused by the inclination. The inclination estimation has slight error as well due to the aforementioned issue with the acceleration measurements, and that in turn affects the estimated axle loads. The matrix-switching of the inclination-estimating Kalman filter can also cause some offset in the inclination estimation in heavy braking maneuvers. Furthermore, the estimated velocity contains error during braking due to the velocity-estimating Kalman filter relying almost solely on the inclination-compensated acceleration measurement. That in turn causes error in the estimated longitudinal tire-road forces, as the estimated aerodynamic drag force is slightly erroneous. The lack of accounting for the vertical acceleration can also cause error in the friction estimation, as the estimated vertical load will contain significant error when the inclination of the road is changing.

The assumption about the suspension being rigid causes error in the bank angle and lateral tire-road force estimations as well. The body has roll angle due to lateral load transfer, which influences the measured lateral acceleration. The lateral tire-road forces are calculated based on the measured lateral acceleration with the assumption that the gravitational acceleration component it contains is only caused by the bank angle of the road. The bank angle and lateral force estimations are further compromised by the side slip angle of the vehicle. When the side slip angle is changing, the time derivative of the lateral velocity of the CoG is non-zero, and that affects the measured lateral acceleration, which then also has a significant impact on the bank angle and lateral force estimations. The side slip angle also influences the longitudinal acceleration, as it then contains a component of the centripetal acceleration. The algorithm also neglects the effect of aerodynamic side forces, which will add some further error. The issues caused by the side slip angle are particularly obvious in the double lane change maneuver results in figure 50, as was discussed earlier. Additionally, the friction potential estimation has a limited resolution during maneuvers that cause the ESP to be

activated due to the way that the potential is calculated using a histogram. Nonetheless, the results show that the algorithm is capable of estimating the friction potential with good accuracy in cornering maneuvers on inclined, banked, and level roads. The highest amount of error is seen in the double lane change maneuver where the estimated potential is 0.05 lower than the actual potential.

The estimated friction potential contains significant error in start maneuvers where the steering angle is high. The front tires produce force in different directions in such situations, which causes the single-track model to sense the friction coefficient as lower than it really is because the model only sees the combined force of the two front tires. In the simulated maneuver, the estimated potential is 0.1131 lower than the actual potential. The results of the maneuver performed with the research vehicle show a similar tendency with the estimated coefficient being markedly lower than the measured value throughout the maneuver.

During start maneuvers on roads with varying friction, the friction potential estimation places greater emphasis on the potential of the road at the point where the maneuver is started due to the potential being calculated as the average friction coefficient over time rather than distance. Furthermore, changes in the longitudinal location of the CoG impact the accuracy of the friction potential estimation. The estimated potential changes linearly with the front axle load in acceleration maneuvers. The location of the CoG keeps changing in daily use due to passengers, luggage, and fuel load. The algorithm assumes the location to be fixed.

9.4 Comparisons to Previous Works

Kim et al. [58] developed an algorithm that estimates the friction coefficient of each tire in real time based on the acceleration and yaw, pitch, and roll rate measurements of an IMU. The calculations of the algorithm are based on a full-vehicle model that consists of four interlinked one-wheel models. The road inclination and bank angle are not accounted for. The algorithm was tested by performing a heavy braking maneuver. The results show that the estimated friction coefficients were close to the coefficients measured with a force transducer. This result is similar to the findings in the braking maneuver tests in this thesis. The advantage of their algorithm is that the coefficient is estimated for each wheel, which allows the electronic driver aids to function even more efficiently, as the friction potential may vary between the tires due to load sensitivity, the condition of the tires, and road conditions. [58]

Klomp et al. [89] created an algorithm that uses an IMU for estimating the longitudinal velocity and the inclination of the road. The principles of the algorithm are similar to those used for estimating the velocity and the inclination in this thesis. The results show good correlation with the velocity and inclination estimations produced by the algorithm developed in this research. [89]

10 Conclusions and Further Developments

The objective of this master's thesis was to develop and examine the accuracy of a novel IMU-based friction estimation algorithm that would account for the effects of road inclination and bank angle. Three different versions of the algorithm were created in order to investigate the effects of the road angles. Tests were conducted with a research vehicle and with a simulated version of the vehicle. The tests were focused on low-friction conditions. Based on the simulation and road test results, the following conclusions can be drawn.

The novel algorithm is capable of estimating the tire-road friction potential with a high degree of accuracy in acceleration, braking, and cornering maneuvers on inclined, banked, and level roads. In the simulations, the estimated potential was within 0.05 of the actual potential, and the results of the maneuvers conducted with the research vehicle also showed the estimation to be accurate. The algorithm also provides accurate estimates of the inclination and bank angle of the road, as well as the longitudinal velocity of the vehicle. The algorithm is also capable of estimating the slip ratios of the driven wheels with good accuracy in acceleration maneuvers. These estimations are useful for the electronic driver aid systems of the vehicle. However, the friction potential estimation does contain significant error in start maneuvers where the steering angle is high.

The results of this research also demonstrate that it is not necessary to try to estimate and account for the inclination and the bank angle in an IMU-based algorithm, as the differences between the friction estimations of the three different algorithm versions were almost negligible. Compensating the effect of the inclination angle was seen to create a tiny difference in the friction estimation in the uphill and downhill acceleration and braking maneuvers. The inclination angle estimated by the algorithm reflected the real angle with reasonable accuracy. However, it was affected by the pitch angle of the body and the effects caused by the Kalman filter switching the measurement noise covariance matrix at the start of heavy braking maneuvers. Using the inclination-compensated acceleration measurement in the velocity-estimating Kalman filter was seen to produce significantly more accurate velocity estimations during heavy braking maneuvers. This means that the inclination compensation might cause a greater difference in the friction estimation in uphill and downhill braking maneuvers that are started at a high velocity, as the aerodynamic drag force would then be a larger factor in the longitudinal force calculations.

The bank angle estimation and compensation was seen to yield a small improvement in the friction coefficient estimation in the simulated maneuver performed in a downhill banked turn. However, the difference did not show up in the friction potential estimation due to the estimation being triggered by the ESP and thus having a low resolution. A major issue with the bank angle estimation is that its accuracy is sensitive to changes in the side slip angle of the vehicle. When the side slip angle is changing, the time derivative of the lateral velocity is non-zero, which affects the lateral acceleration. Furthermore, the inclination estimation is also influenced by the side slip angle during cornering because of a portion of the centripetal acceleration then showing up in the longitudinal acceleration. Consequently, combining the created algorithm with a side slip angle estimation algorithm could substantially increase its effectiveness in cornering maneuvers.

Compensating for the inclination and bank angle makes little difference in the friction estimation because the angles are partially compensated even in the versions of the algorithm that were not specifically designed to account for them. This is because the equations that the longitudinal, lateral, and vertical tire forces are solved from use the longitudinal and lateral acceleration measurements of the IMU, which in turn contain components of gravitational acceleration when the road is not level. As a consequence, a major part of the effect of the road angles is compensated in the force calculations regardless of the algorithm version. Nonetheless, estimating the inclination and the banking is still beneficial for the electronic driver aids, as the angles have a significant influence on the acceleration capabilities of the vehicle. The driver aid systems use the information about the maximum possible acceleration in their control logics. Compensating the inclination angle is beneficial also for anti-lock braking systems because, as the results showed, the velocity is then estimated much more accurately during braking, which in turn improves the ability of the system to estimate the slip ratios. Thus, the ratios can be kept close to the optimum value more effectively.

During acceleration maneuvers on roads that have a varying friction potential, the friction potential estimation is not only heavily dependent on how frequently the potential changes but also on the friction of the surface the acceleration maneuver is started on. This is due to the potential being estimated as the average coefficient over time rather than distance. The results also showed that the friction potential estimation is, during acceleration maneuvers, linearly dependent on the longitudinal weight distribution of the vehicle.

The main intention behind incorporating the single-track model into the algorithm was to improve the accuracy of the friction estimation in start maneuvers where the steering angle is high. However, the front wheels appear to produce force in vastly different directions in such situations. This is problematic for the single-track model, as it only senses the combined effect of the forces. The smaller the angle between the total forces produced by the front wheels is, the more accurate the friction estimation will be. It can be concluded based on the results of this research that the single-track model is not an effective solution for estimating the friction potential in these types of maneuvers.

In addition to merging the developed algorithm with a side slip angle estimation algorithm, a system could be developed that estimates the longitudinal weight distribution of the vehicle. The accuracy of the friction estimation would then not be dependent on changes in the weight distribution, as the algorithm would always have accurate information about the location of the center of gravity. Further research could also be done on the ESP-based friction potential estimation, as its resolution is currently relatively low. Additionally, the ESP system developed for the simulation software could be significantly improved. The system appeared to intervene prematurely in most situations. Control rules based on the side slip angle of the vehicle could also be incorporated into it.

Bibliography

[1] **National Highway Traffic Safety Administration.** *Critical Reasons for Crashes Investigated in the National Motor Vehicle Crash Causation Survey.* Washington, DC : National Center for Statistics and Analysis, 2015.

[2] *Automated driving - Where are we heading?* **Hübner, Dr. Hans-Peter.** [ed.] Peter E. Pfeffer. Munich : Springer Vieweg, 2014. 5th International Munich Chassis Symposium Proceedings. pp. 23-33. ISBN 978-3-658-05977-4.

[3] **Robert Bosch GmbH.** *Safety, Comfort and Convenience Systems.* Plochingen : Robert Bosch GmbH, 2006. ISBN 0-8376-1391-4.

[4] *Evolution of Electronic Control Systems for Improving the Vehicle Dynamic Behavior.* **Zanten, Anton T. van.** Hiroshima, Japan : JSAE, 2002. Proceedings of AVEC '02.

[5] **Tuononen, Ari and Koisaari, Tapio.** *Ajoneuvojen liikedynamiikka.* Espoo : Autoalan Koulutuskeskus, 2014.

[6] *Tire-Road Friction Estimation for Enhancing the Autonomy of Wheel-Driven Vehicles.* **Kim, Chang-Sei, et al.** Seoul, South Korea : IEEE, 2007. International Conference on Control, Automation and Systems, 2007. pp. 273-277. ISBN 978-89-950038-6-2. DOI: 10.1109/ICCAS.2007.4406921

[7] *Measurement of tyre/road-friction ahead of the car and inside the tyre.* **Breuer, Bert, Eichhorn, Ulrich and Roth, Jürgen.** Yokohama, Japan : JSAE, 1992. Proceedings of the International Symposium on Advanced Vehicle Control 1992. pp. 347-353.

[8] *Prediction and monitoring of tyre-road friction.* **Eichhorn, U. and Roth, J.** London, UK : s.n., 1992. Proceedings of XXIV FISITA Congress. pp. 67-74. ISBN 0-85298-837-0.

[9] *Road Surface Recognition Method Using Optical Spatial Filter.* **Uno, Tetsuya, et al.** Tsukuba, Japan : JSAE, 1994. Proceedings of the International Symposium on Advanced Vehicle Control 1994. pp. 509-515.

[10] *Tire-road Friction-Coefficient Estimation.* **Rajamani, Rajesh, et al.** 4, 2010, IEEE Control Systems Magazine, Vol. 30, pp. 54-69. ISSN 1066-033X. DOI: 10.1109/MCS.2010.937006

[11] **MathWorks.** CarMaker for use with Simulink. [Online] [Cited: March 15, 2016.] http://se.mathworks.com/products/connections/product_detail/product_35636.html.

[12] **Société de Technologie Michelin.** *The Tyre Grip.* 2001.

[13] **Kindt, Peter.** *Structure-Borne Tyre/Road Noise due to Road Surface Discontinuities.* Department of Mechanical Engineering, Catholic University of Leuven, Faculty of Engineering Technology. 2009. PhD Thesis. ISBN 978-94-6018-085-9.

[14] **Matilainen, Mika.** *Tyre Friction Potential Estimation by Aligning Torque and Lateral Force Information.* Department of Engineering Design and Production, Aalto University School of Science and Technology. Espoo, Finland : s.n., 2010. Master's thesis.

[15] **Erman, Burak, Mark, James E. and Roland, C. Michael.** *The Science and Technology of Rubber.* 4th edition. Boston : Elsevier Academic Press, 2013. ISBN 978-0-12-394584-6.

[16] **Reif, Konrad.** *Automotive Handbook.* [ed.] Karl-Heinz Dietsche. 8th edition. Plochingen : Robert Bosch GmbH, 2011. ISBN 978-0-8376-1686-5.

[17] **Marshal Tyre.** Tyre tread design. [Online] [Cited: February 26, 2016.] http://www.marshaltyre.co.uk/design.php.

[18] **Yokohama Tire Corporation.** Tread patterns. [Online] [Cited: February 27, 2016.] http://global.yokohamatire.net/technology/tireknowledge/treadpatterns.html.

[19] **National Cooperative Highway Research Program.** Guide for Pavement Friction. [Online] 2009. http://onlinepubs.trb.org/onlinepubs/nchrp/nchrp_w108.pdf.

[20] **Marshal Tyre.** Tyre choice by season. [Online] [Cited: February 27, 2016.] http://www.marshaltyre.co.uk/season.php.

[21] **Bridgestone Corporation.** Studded snow tires vs studless snow tires. [Online] [Cited: February 27, 2016.] http://www.bridgestonetire.com/tread-and-trend/drivers-ed/snow-tires-studded-tires-vs-studless-tires.

[22] **British Columbia Ministry of Transportation and Infrastructure.** How to Choose from 4 Types of Tires for Winter Driving in BC. [Online] [Cited: February 27, 2016.] http://tranbc.ca/2014/10/24/how-to-choose-from-4-types-of-winter-tires-for-winter-driving-in-bc/#sthash.5yt9ZwnH.7vyw0edF.dpbs.

[23] **Milliken, William F. and Milliken, Douglas L.** *Race Car Vehicle Dynamics.* 3rd edition. Warrendale : SAE International, 1995. ISBN 1-56091-526-9.

[24] **Pacejka, Hans B.** *Tyre and Vehicle Dynamics.* 2nd edition. Oxford : Elsevier Ltd, 2006. ISBN 978-0-7506-6918-4.

[25] **Dukkipati, Rao, et al.** *Road Vehicle Dynamics.* Warrendale : SAE International, 2008. ISBN 978-0-7680-1643-7.

[26] **Peussa, Pertti and Koskinen, Sami.** *Final Report of EU project FRICTI@N.* VTT. 2009.

[27] *Tire slip-angle force measurements on winter surfaces.* **Coutermarsh, Barry A. and Shoop, Sally A.** 4, s.l. : Elsevier, 2009, Journal of Terramechanics, Vol. 46, pp. 157-163. ISSN 0022-4898. DOI: 10.1016/j.jterra.2008.08.002

[28] **Saalimo, Mikko.** *Ajoneuvomallin validointi ja rengasparametrien määritys kokeellisesti talviolosuhteissa.* Department of Engineering Design and Production, Aalto University. 2013. Master's thesis.

[29] *The "Intelligent Tire" Utilizing Passive SAW Sensors - Measurement of Tire Friction.* **Pohl, Alfred, Steindl, Reinhard and Reindl, Leonhard.** 6, s.l. : IEEE Instrumentation and Measurement Society, 1999, IEEE Transactions on Instrumentation and Measurement, Vol. 48, pp. 1041-1046. ISSN 0018-9456. DOI: 10.1109/19.816111

[30] *Highly sensitive AlGaAs/GaAs position sensors for measurement of tyre tread deformation.* **Brandt, M., et al.** 8, s.l. : Institution of Engineering and Technology, 1998, Electronics Letters, Vol. 34, pp. 760-762. ISSN 0013-5194. DOI: 10.1049/el:19980520

[31] *The sidewall torsion sensor system.* **Becherer, T.** Darmstadt, Germany : s.n., 1998. Proceedings of the 2. Darmstädter Reifenkolloquium.

[32] *On-Line Determination of Tyre Deformation, a Novel Sensor Principle.* **Mágori, Valentin, Mágori, Valentin R. and Seitz, N.** 1998. Proceedings of the IEEE Ultrasonics Symposium. pp. 485-488. ISSN 1051-0117.

[33] *Optical position detection to measure tyre carcass deflections.* **Tuononen, Ari.** 6, s.l. : Taylor & Francis, 2008, Vehicle System Dynamics, Vol. 46, pp. 471-481. DOI: 10.1080/00423110701485043

[34] *Optical Position Detection Sensor to Measure Tyre Carcass Deflections in Aquaplaning.* **Tuononen, Ari and Hartikainen, Lassi.** 3, s.l. : Inderscience Enterprises Ltd., 2008, International Journal of Vehicle Systems Modelling and Testing, Vol. 3, pp. 189-197. ISSN 1745-6436. DOI: 10.1504/IJVSMT.2008.023837

[35] **Dr. D. Wehrhahn.** Deformation measurement (static/dynamic). [Online] [Cited: March 23, 2016.] http://www.drwehrhahn.de/englisch/sites/03anwendungsbereiche-en/en02reifen-und-gummi/en-09reifen-und-gummi.html.

[36] **Casselgren, Johan.** *Road Surface Characterization Using Near Infrared Spectroscopy.* Luleå University of Technology. Luleå : s.n., 2011. Doctoral thesis. ISSN 1402-1544, ISBN 978-91-7439-273-9.

[37] *Concurrent Monitoring of In-plane Strain and Out-of-plane Displacement of Tire Using Digital Image Correlation Method.* **Hiraoka, Naoki, Matsuzaki, Ryosuke and Todoroki, Akira.** 11, 2009, Journal of Solid Mechanics and Materials Engineering, Vol. 3, pp. 1148-1159. ISSN 1880-9871. DOI: 10.1299/jmmp.3.1148

[38] **Green, Russell Wright.** *A Non-contact Method for Sensing Tire Contact Patch Deformation Using a Monocular Vision System and Speckled Image Tracking.* Auburn University. 2011. Master's Thesis.

[39] *Wireless flexible capacitive sensor based on ultra-flexible epoxy resin for strain measurement of automobile tires.* **Matsuzaki, Ryosuke and Todoroki, Akira.** 1, s.l. :

Elsevier, 2007, Sensors and Actuators A, Vol. 140, pp. 32-42. ISSN 0924-4247. DOI: 10.1016/j.sna.2007.06.014

[40] *Embedded Flexible Force Sensor for In-Situ Tire-Road Interaction Measurements.* **Zhang, Yizhai, Yi, Jingang and Liu, Tao.** 5, 2013, IEEE Sensors Journal, Vol. 13, pp. 1756-1765. ISSN 1530-437X. DOI: 10.1109/JSEN.2013.2241051

[41] *On a road tire deformation measurement system using a capacitive-resistive sensor.* **Sergio, M., et al.** 6, 2006, Smart Materials and Structures, Vol. 15, pp. 1700-1706. ISSN 0964-1726. DOI: 10.1088/0964-1726/15/6/023

[42] *Estimation of Tire-Road Friction Coefficient Using a Novel Wireless Piezoelectric Tire Sensor.* **Erdogan, Gurkan, Alexander, Lee and Rajamani, Rajesh.** 2, s.l. : IEEE Sensors Council, 2011, IEEE Sensors Journal, Vol. 11, pp. 267-279. ISSN 1530-437X. DOI: 10.1109/JSEN.2010.2053198

[43] **MTS.** Spinning Wheel Integrated Force Transducer (SWIFT). [Online] [Cited: March 23, 2016.] www.elhys.com.pl/download.php?id=51.

[44] *Three Three-Axis Accelerometers on the Inner Liner of a Tyre for Finding the Tyre-Road Contact Friction Indicators.* **Niskanen, Arto and Tuononen, Ari.** 2014, Sensors Journal, Vol. 15, pp. 19251-19263. ISSN 1424-8220. DOI: 10.3390/s150819251

[45] *New Regressors for the Direct Identification of Tire Deformation in Road Vehicles Via "In-Tire" Accelerometers.* **Savaresi, Sergio M., et al.** 4, s.l. : IEEE Control Systems Society, 2008, IEEE Transactions on Control Systems Technology, Vol. 16, pp. 769-780. ISSN 1063-6536. DOI: 10.1109/TCST.2007.912245

[46] *Measurement of contact forces and patch features by means of accelerometers fixed inside the tire to improve future car active control.* **Braghin, F., et al.** 1, s.l. : Taylor & Francis, 2006, Vehicle System Dynamics: International Journal of Vehicle Mechanics and Mobility , Vol. 44, pp. 3-13. DOI: 10.1080/00423110600867101

[47] *Tyre-road friction coefficient estimation based on tyre sensors and lateral tyre deflection: modelling, simulations and experiments.* **Hong, Sanghyun, et al.** 5, s.l. : Taylor & Francis, 2013, International Journal of Vehicle Mechanics and Mobility, Vol. 51, pp. 627-647. ISSN 1744-5159. DOI: 10.1080/00423114.2012.758859

[48] *Piezoelectric Vibration-Based Energy Harvesters for Next-Generation Intelligent Tires.* **Singh, Kanwar Bharat and Taheri, Saied.** 4, 2013, Tire Science and Technology, Vol. 41, pp. 262-293. ISSN 0090-8657.

[49] *Estimation of the Maximum Tire-Road Friction Coefficient.* **Müller, Steffen, Uchanski, Michael and Hedrick, Karl.** 4, s.l. : The American Society of Mechanical Engineers, 2003, Journal of Dynamic Systems, Measurement, and Control, Vol. 125, pp. 607-617. DOI: 10.1115/1.1636773

[50] *An Estimation Method of the Maximum Tire-road Friction Coefficient Using an Electric Power Assist Steering.* **Takagi, Fumiaki, et al.** Loughborough, UK : JSAE, 2010.

Proceedings of the 10th International Symposium on Advanced Vehicle Control, AVEC '10. pp. 779-782.

[51] *Estimation of Tire Slip Angle and Friction Limits Using Steering Torque.* **Hsu, Yung-Hsiang Judy, Laws, Shad M. and Gerdes, J. Christian.** 4, s.l. : IEEE Control Systems Society, 2010, IEEE Transactions on Control Systems Technology, Vol. 18, pp. 896-907. ISSN 1063-6536. DOI: 10.1109/TCST.2009.2031099

[52] *The Tyre As A Sensor To Estimate Friction.* **Pasterkamp, Wim R. and Pacejka, Hans B.** Aachen, Germany : s.n., 1996. Proceedings of AVEC '96. pp. 839-854.

[53] *Tire friction potential estimation from measured tie rod forces.* **Matilainen, Mika J. and Tuononen, Ari J.** Baden-Baden, Germany : IEEE, 2011. 2011 IEEE Intelligent Vehicles Symposium (IV). pp. 320-325. ISSN 1931-0587. DOI: 10.1109/IVS.2011.5940528

[54] *Estimation of individual tire-road friction coefficients based on tire force information.* **Cho, Wanki, Chung, Taeyoung and Yi, Kyongsu.** Manchester, UK : s.n., 2011. The 22nd International Symposium on Dynamics of Vehicles on Roads and Tracks.

[55] *Robust Nonlinear Observer To Estimate Road Friction Coefficient and Tire Slip Angle.* **Ahn, Changsun, Peng, Huei and Tseng, H. Eric.** Loughborough, UK : JSAE, 2010. Proceedings of the 10th International Symposium on Advanced Vehicle Control, AVEC '10. pp. 12-17.

[56] **Svendenius, Jacob.** *Tire Modeling and Friction Estimation.* Department of Automatic Control, Lund University. Lund, Sweden : s.n., 2007. Doctoral Thesis. ISSN 0280-5316.

[57] *Estimation of Tyre Friction for enhanced ABS-Systems.* **Kiencke, U. and Daiß, A.** Tsukuba, Japan : JSAE, 1994. Proceedings of the International Symposium on Advanced Vehicle Control 1994. pp. 515-520.

[58] *Estimation of Tire-Road Friction Based on Onboard 6-DoF Acceleration Measurement.* **Kim, Chang-Sei, et al.** 8, s.l. : IEEE Vehicular Technology Society, 2015, IEEE Transactions on Vehicular Technology, Vol. 64, pp. 3368-3377. ISSN 0018-9545. DOI: 10.1109/TVT.2014.2358616

[59] *A New Approach to Linear Filtering and Prediction Problems.* **Kalman, Rudolf E.** 1, 1960, Transactions of the ASME – Journal of Basic Engineering, Vol. 82, pp. 35-45. DOI: 10.1115/1.3662552

[60] *Combined Estimation of Vehicle States and Road Friction Coefficients Using Dual Extended Kalman Filter.* **Hu, Dan, Zong, Changfu and Na, Xiaoxiang.** Loughborough, UK : s.n., 2010. Proceedings of the 10th International Symposium on Advanced Vehicle Control, AVEC '10. pp. 309-314.

[61] *Development of Identification of Tire-road Friction Conditions.* **Lian, Yufeng, et al.** Guangzhou, China : s.n., 2012. 12th International Conference on Control Automation

Robotics & Vision (ICARCV). pp. 1812-1817. ISBN 978-1-4673-1871-6. DOI: 10.1109/ICARCV.2012.6485425

[62] *A new nonlinear observer using unscented Kalman filter to estimate sideslip angle, lateral tire road forces and tire road friction coefficient.* **Cheng, Qi, Correa-Victorino, Alessandro and Charara, Ali.** Baden-Baden, Germany : s.n., 2011. 2011 IEEE Intelligent Vehicles Symposium, Proceedings. pp. 709-714. ISSN 1931-0587. DOI: 10.1109/IVS.2011.5940501

[63] *Vehicle Lateral State Estimation Based on Measured Tyre Forces.* **Tuononen, Ari J.** 2009, Sensors, Vol. 9, pp. 8761-8775. DOI: 10.3390/s91108761

[64] *Effect of cornering forces measurement on real-time estimation of tyre-road friction coefficient , vehicle sideslip angle and road bank angle.* **Cheli, Federico, Ivone, Davide and Sabbioni, Edoardo.** Tokyo, Japan : JSAE, 2014. Proceedings of the 12th International Symposium on Advanced Vehicle Control, AVEC '14. pp. 285-293.

[65] *A New Nonlinear Observer of the Sideslip Angle and the Road Bank Angle using the Particle Filter.* **Cheng, Qi, Victorino, Alessandro Correa and Charara, Ali.** Seoul, Korea : JSAE, 2012. Proceedings of the 11th International Symposium on Advanced Vehicle Control, AVEC '12.

[66] **Kiencke, Uwe and Nielsen, Lars.** *Automotive Control Systems: For Engine, Driveline, and Vehicle.* 2nd edition. Berlin : Springer, 2005. ISBN 3-540-23139-0.

[67] *Bosch ESP Systems: 5 years of experience.* **Zanten, Anton van.** 2000. Proceedings of the 2000 SAE Automotive Dynamics & Stability Conference. pp. 211-220. DOI: 10.4271/2000-01-1633

[68] **Falanga, Giorgio.** *Influence of tyre pressure on vehicle steady-state lateral dynamics.* Department of Engineering, University of Pisa. Pisa, Italy : s.n., 2011. Master's Thesis.

[69] **Isomaa, Matti, Vauhkonen, Niclas and Sallinen, Reetu.** *Projekti E: Polttoaineenkulutuksen mittaaminen ja simuloiminen, Loppuraportti.* Department of Engineering Design and Production, Aalto University. Espoo, Finland : s.n., 2012.

[70] **Elonen, Tuomo.** *Jousien ja vaimentimien mittaus. Lyhyt suunnittelutyö -kurssin raportti.* Teknillinen korkeakoulu. Espoo, Finland : s.n., 2008.

[71] **Cars-data.** Volkswagen Golf Variant 1.9 TDI 105hp Comfortline 2007 - 2009. [Online] [Cited: March 31, 2016.] http://www.cars-data.com/en/volkswagen-golf-variant-1.9-tdi-105hp-comfortline-specs/50774.

[72] **Nokian Tyres.** Nokian Hakkapeliitta R. [Online] [Cited: March 31, 2016.] https://www.nokiantires.com/winter-tires/nokian-hakkapeliitta-r/.

[73] **Analog Devices.** ADIS16362 Six Degrees of Freedom Inertial Sensor Data Sheet. [Online] [Cited: April 1, 2016.] http://www.analog.com/media/en/technical-documentation/data-sheets/ADIS16362.pdf.

[74] **MTS.** SWIFT 20 (Ultra) Sensor Product Information. [Online] [Cited: April 1, 2016.] http://www.mts.com/ucm/groups/public/documents/library/mts_008356.pdf.

[75] **Corrsys Datron Sensorsysteme GmbH.** *Correvit S-350 non-contact 2-axis Optical Sesnsor for slip free measurement of longitudinal and transversal dynamics User Manual Volume I.* 2008.

[76] *Vehicle Longitudinal Velocity Estimation with Adaptive Kalman Filter.* **Lu, Xiong, Yunlong, Gao and Yuan, Feng.** Seoul, South Korea : s.n., 2012. Proceedings of the 11th International Symposium on Advanced Vehicle Control, AVEC '12.

[77] **IPG Automotive.** *CarMaker Reference Manual Version 3.0.* 2010.

[78] **IPG Automotive**. *CarMaker User's Guide Version 3.0.* 2010.

[79] **IPG Automotive**. *IPGKinematics Reference Manual Version 3.4.14.* 2010.

[80] **MathWorks.** MATLAB features. [Online] [Cited: April 6, 2016.] http://se.mathworks.com/products/matlab/features.html.

[81] **MathWorks**. Simulink overview. [Online] [Cited: April 6, 2016.] http://se.mathworks.com/products/simulink/index.html?s_tid=gn_loc_drop.

[82] **IPG Automotive.** *CarMaker Programmer's Guide Version 3.0.* 2010.

[83] **Mäkelä, Mikko, et al.** *Ajoneuvojen tuotekehitys – Ryhmä D: Pusla, Loppuraportti.* Department of Engineering Design and Production, Aalto University. Espoo, Finland : s.n., 2011. Project report.

[84] **MathWorks.** Band-Limited White Noise. [Online] [Cited: April 12, 2016.] http://www.mathworks.com/help/simulink/slref/bandlimitedwhitenoise.html.

[85] **Tuononen, Ari.** *Feasibility of Measured Tyre Forces in Global Chassis Control.* Department of Mechanical Engineering, Helsinki University of Technology. Espoo, Finland : s.n., 2005. Master's thesis.

[86] **Smith, Steven W.** *The Scientist and Engineer's Guide to Digital Signal Processing.* San Diego : California Technical Publishing, 1997. ISBN 0-9660176-3-3.

[87] **MathWorks.** Signal Smoothing. [Online] [Cited: 04 27, 2016.] http://se.mathworks.com/help/signal/examples/signal-smoothing.html?s_tid=gn_loc_drop#zmw57dd0e245.

[88] **MathWorks**. Kalman Filter. [Online] [Cited: May 01, 2016.] http://se.mathworks.com/help/dsp/ref/kalmanfilter.html.

[89] *Robust Estimation of Longitudinal Velocity and Road Slope in Hybrid Electric Vehicles using an Adaptive Kalman Filter.* **Klomp, Matthjis, Gao, Yunlong and**

Bruzelius, Fredrik. Qingdao, China : The International Association for Vehicle System Dynamics, 2013. Proceedings of the 23rd International Symposium on Dynamics of Vehicles on Roads and Tracks.

Appendix 1: Simulation Model Magic Formula Coefficients

Longitudinal force coefficients (pure longitudinal slip)

$p_{Cx1} = 1.48$	$p_{Dx1} = 1.0$	$p_{Dx2} = -0.075$	$p_{Dx3} = 0$
$p_{Ex1} = 0.7$	$p_{Ex2} = 0.08$	$p_{Ex3} = 0.01$	$p_{Ex4} = 0$
$p_{Kx1} = 13$	$p_{Kx2} = -0.163$	$p_{Kx3} = -0.2$	$p_{Hx1} = -0.002$
$p_{Hx2} = 0.002$	$p_{Vx1} = 0$	$p_{Vx2} = 0$	

Longitudinal force coefficients (combined slip)

$r_{Bx1} = 13$	$r_{Bx2} = -7$	$r_{Cx1} = 1.03$	$r_{Ex1} = 0$
$r_{Ex2} = 0$	$r_{Hx1} = 0.007$		

Lateral force coefficients (pure lateral slip)

$p_{Cy1} = 1.45$	$p_{Dy1} = -0.98$	$p_{Dy2} = 0.13$	$p_{Dy3} = -11.23$
$p_{Ey1} = -2$	$p_{Ey2} = 2.45$	$p_{Ey3} = 2.1128 \cdot 10^{-6}$	$p_{Ey4} = 0$
$p_{Ky1} = -25$	$p_{Ky2} = 10$	$p_{Ky3} = 0$	$p_{Hy1} = -1.2102 \cdot 10^{-8}$
$p_{Hy2} = 1.5811 \cdot 10^{-8}$	$p_{Hy3} = 0.25$	$p_{Vy1} = 2.5847 \cdot 10^{-7}$	$p_{Vy2} = -1.2802 \cdot 10^{-7}$
$p_{Vy3} = 0.15$	$p_{Vy4} = 0.039$		

Lateral force coefficients (combined slip)

$r_{By1} = 14$	$r_{By2} = 6$	$r_{By3} = -0.015$	$r_{Cy1} = 1.05$
$r_{Ey1} = 0$	$r_{Ey2} = 0$	$r_{Hy1} = 0$	$r_{Hy2} = 0$
$r_{Vy1} = 22.965$	$r_{Vy2} = 0.37981$	$r_{Vy3} = 1.8552$	$r_{Vy4} = 0.08767$
$r_{Vy5} = -8.823 \cdot 10^{-11}$	$r_{Vy6} = 0.90374$		

Transient behavior coefficients

$p_{Tx1} = 1.5$	$p_{Tx2} = 0.180096$	$p_{Tx3} = -0.15$	$p_{Ty1} = 1.75$
$p_{Ty2} = 1.35$			

Scale factors

$\lambda_{Cx} = 1$	$\lambda_{Cy} = 1$	$\lambda_{Ex} = 1$	$\lambda_{Ey} = 1$
$\lambda_{Hx} = 1$	$\lambda_{Hy} = 1$	$\lambda_{K\varkappa} = 1$	$\lambda_{K\gamma\alpha} = 1$
$\lambda_{Vx} = 1$	$\lambda_{Vy} = 1$	$\lambda_{V\gamma\varkappa} = 1$	$\lambda_{x\alpha} = 1$
$\lambda_{\gamma\varkappa} = 1$	$\lambda_{\gamma x} = 1$	$\lambda_{\gamma y} = 1$	$\lambda_{\gamma z} = 1$
$\lambda_{\mu x} = 0.35\ (0.15)$	$\lambda_{\mu y} = 0.35\ (0.15)$		